Direct Numerical Simulation of Flow Instabilities in Variable Velocity Flows

A thesis submitted

in partial fulfillment for the award of the degree of

Doctor of Philosophy

by

Sarath K. P.

Department of Aerospace Engineering
Indian Institute of Space Science and Technology
Thiruvananthapuram, India

September 2023

Certificate

This is to certify that the thesis titled ***Direct Numerical Simulation of Flow Instabilities in Variable Velocity Flows*** submitted by **Sarath K. P.**, to the Indian Institute of Space Science and Technology, Thiruvananthapuram, in partial fulfillment for the award of the degree of **Doctor of Philosophy** is a bonafide record of the original work carried out by him under my supervision. The contents of this thesis, in full or in parts, have not been submitted to any other Institute or University for the award of any degree or diploma.

Dr. Manu K. Vasudevan
Associate Professor,
Aerospace Engineering Department,
Indian Institute of Space Science and
Technology.

Dr. Deepu M.
Professor and Head of the Department,
Aerospace Engineering Department,
Indian Institute of Space Science and
Technology.

Place: Thiruvananthapuram
Date: September 2023

Declaration

I declare that this thesis titled ***Direct Numerical Simulation of Flow Instabilities in Variable Velocity Flows*** submitted in partial fulfillment for the award of the degree of **Doctor of Philosophy** is a record of the original work carried out by me under the supervision of **Dr. Manu K. Vasudevan**, and has not formed the basis for the award of any degree, diploma, associateship, fellowship, or other titles in this or any other Institution or University of higher learning. In keeping with the ethical practice in reporting scientific information, due acknowledgments have been made wherever the findings of others have been cited.

Place: Thiruvananthapuram
Date: September 2023

Sarath K. P.
(SC18D001)

To my parents, who instilled in me the values of hard work and education, I dedicate this thesis . . .

Acknowledgements

With joy and pleasure, I would like to express my sincere thanks and a deep sense of gratitude to my research adviser, Dr. Manu K. Vasudevan, for suggesting this problem. As a result of his guidance, encouragement, and advice, coupled with his excellent knowledge of various problems in fluid mechanics, I developed my critical thinking skills. He was patient and understanding, even when I made mistakes, and he helped me to build my scientific attitude and to become a better researcher.

I want to thank the present Head of the Department, Dr. Deepu M., for his valuable suggestions and encouragement in the course of my work. He believed that collaborating with other graduate students would help me expand my research areas and encouraged me to do so. I also thank the previous Head of the Departments, Dr. Manoj T. Nair and Dr. Aravind Vaidyanathan, for their patronage and support during their tenure in the HOD office. I am deeply grateful to my doctoral committee members, Dr. Salih A., Dr. Pradeep Kumar P., and Dr. Govindan Kutty M., for their critical comments and insightful feedback that helped me to strengthen my research.

I want to express my heartfelt gratitude to my fellow research scholars Anuja, Dr. Veena, Dayal, Dr. Sajith, Varsha, Dileep, Annmary, and all others for their support and for giving me friendly company during my longest life journey. I also wish to thank my senior colleagues, Dr. Jishnu, Dr. Risha, Dr. Arun Govindneelan, Dr. Aravind, Dr. Dhanesh, and all others, for keeping a lively atmosphere in the lab and guiding me during the early days in IIST. I appreciate the support of my lab mates, Vishnu Harikumar, Akhil S.L., Vishnu Raj, and all others, in maintaining a research environment that is both collaborative and stimulating. I would like to express my sincere thanks to my friends Dr. Sarathkrishnan, Shins, Nandakumar, Vishal, and Prabin for their unwavering support and motivation in pursuing our shared dreams.

I am deeply grateful to my parents, Prakasan and Radhalakshmy, for their unconditional love and support. They have always been there for me through thick and thin. I am also grateful to my grandparents, Vasudevan and Sathy, for their care and love. My sister, Greeshma, and brother-in-law, Shinoj, have always been there for me, and I am so lucky to have them in my life. I would also like to thank my extended family members, both on my maternal and paternal sides, for their love and support.

I know that I would not be the person I am today without the love and support of my family and friends. They have always been there for me, no matter what. I am highly grateful to them for patiently waiting to complete my work…

Sarath K. P.

Abstract

The origin of turbulence in fluid flow fields has been a significant concern for many years. Flow transition under steady inflow conditions over various geometries has been the subject of extensive experimental, theoretical, and numerical studies. Transitional flows with an unsteady inflow play a vital role in a broad range of applications, including biological fluid transport to space applications, which still went unexplored due to experimental and computational limitations. In such cases, the thickness of the boundary layer formed over the solid surface varies in both space and time, causing a high level of complexity in the path of vortical structures formed from the shear/boundary layer. Also, time and space-dependent shear stress exerted by the fluid, separation, and associated instability phenomena are to be better understood. Recent advances in numerical methods have enabled us to simulate fluid flow under transitional conditions.

This study uses direct numerical simulations (DNS) to investigate the stability of vortical flow structures that form in the transitional boundary layer under an adverse pressure gradient over two different geometries. In the first case, a strong spatial pressure gradient is created using a bell-shaped wall-attached bluff body, while in the second case, a weak spatial pressure gradient is induced using a slowly diverging channel. A transient inflow condition is enforced at the inlet through analytical velocity profiles of a trapezoidal pulse, consisting of the acceleration phase from rest followed by the constant velocity phase and deceleration phase to rest, similar to existing experimental studies [1, 2]. By selecting suitable inflow parameters, we isolate the individual effects of acceleration and deceleration on the vortex evolution. Analytical inflow profiles for such a trapezoidal pulse have been developed using the Laplace transform for a given flow rate [3].

An open-source DNS code (INCOMPACT3D [4]) is used for the flow simulation and is a highly parallelized code that emerged as an efficient way to tackle complex flow simulations. It combines higher-order spatial discretization with spectral methods to simulate incompressible flows over complex bodies enforced through immersed boundary methods (IBM). The use of IBM allows the inclusion of complex geometries in Cartesian mesh without any body-fitting considerations. Both spanwise and streamwise vorticity visualizations depict the vortex growth and disintegration over both top and bottom channel walls. In addition, the spatial and temporal growth of shear layers and three-dimensional instabilities

are investigated in detail for each case using both numerical and theoretical methods. The underlying coherent flow features of the transitional flows and associated time dynamics are extracted using the modal reduction method like dynamic mode decomposition (DMD) and further corroborated with theoretical/numerical growth rate analysis.

In a bluff body wake, the flow development starts with the formation of a primary vortex, followed by a two-dimensional circular array of spanwise vortex tubes by inflectional shear-layer instability. At sufficiently high Reynolds numbers, the shear layer vortices originated from two-dimensional fluctuations deformed by three-dimensional instabilities, giving fragmented streamwise vorticity. In addition, long-wavelength, 'tongue-like structures' and short-wavelength, 'rib-like structures' are evident near the top wall and separation bubble, respectively. The three-dimensional transition phase is further analyzed by the vorticity generation mechanism for streamwise vorticity. Using the DMD algorithm, distinct flow features, such as mode shape, frequency, and growth rate, are identified and compared with significant maxima in the frequency spectrum of vertical velocity and momentum thickness variations.

In a slowly diverging channel with a relatively low spatial pressure gradient combined with a time-varying trapezoidal-shaped inflow boundary condition, the flow transition begins with two-dimensional primary instability characterized by the formation of inflectional velocity profiles, followed by local separation and the emergence of an array of shear layer vortices. We systematically divide simulation cases into three categories based on the onset of secondary instability and the generation of streamwise vorticity. At low and medium Reynolds numbers (type I), the spanwise vortex rolls formed by inflectional instability remain two-dimensional and diffuse at the channel center without exhibiting further instabilities. At high Reynolds numbers and deceleration rates (type II), the rolled shear layer exhibits secondary instability during the zero mean inflow phase, followed by local incipient turbulent structure formation. The streamwise vorticity that develops over the shear layer structures causes oscillations with a spanwise wavelength similar to those associated with the elliptic instability in a counter-rotating vortex pair. Using the Lamb-Oseen approximation of vortices in conjunction with the dynamic mode decomposition algorithm of the three-dimensional flow field, we successfully identified the unstable nature of the elliptical instability evolving over the secondary vortices. The third category (type III) is characterized by periodic unsteady separation, secondary instability, and merging of shear layer vortices, which occurs when Reynolds numbers are high and deceleration rates are low.

In both geometries, flow separation, and vortex formation are caused by highly inflec-

tional streamwise velocity profiles, which are induced in the acceleration phase of a bluff body and during the constant velocity phase of a diverging channel. Shear layer instabilities and sequential roll-ups in a bluff body wake develop from an unstable velocity shear layer induced by early separation and high blockage ratios. Unsteady separation and vortex shedding arise in a diverging channel, offering a low spatial gradient combined with low deceleration rates. The three-dimensional transition is evident only at high inflow velocities for both geometries, whereas low inflow velocities inhibit spanwise oscillation growth, and flow features diffuse during zero-mean inflow. The nature of the vortical structures that develop in the wake of both geometries significantly impacts the onset and development of three-dimensional transition. In the bluff-body wake, the secondary instability initiates with the merging of the co-rotating body vortex structures ejected from the bottom boundary layer due to the shear layer vortex interaction. Such a merging mechanism induces small-wavelength rib-like braid instabilities similar to mode B instabilities in cylinder wake studies. Simultaneously, the counter-rotating vortex pair in the top wall indicates a three-dimensional transition with a relatively higher spatial wavelength. In a diverging channel, the primary vortex that develops from the initial inflectional profile further induces boundary layer vortices, forming a counter-rotating vortex pair susceptible to elliptic instability due to mutual induction and can later lead to three-dimensional disintegration.

Contents

List of Figures

List of Tables

Abbreviations

APG	Adverse Pressure Gradient
CFD	Computational Fluid Dynamics
CFL	Courant Friedrichs Lewy
DMD	Dynamic Mode Decomposition
DNS	Direct Numerical Simulation
IBM	Immersed Boundary Method
ROM	Reduced Order Models
RMS	Root Mean Square
SRM	Solid Rocket Motor

Nomenclature

a	Acceleration
a_1, a_2	Core radius of vortices
b	distance between vortex centers
C_f	Skin friction coefficient
d	Deceleration
f	frequency
f_{DMD}	DMD frequency
P, p	Pressure field
R	Radius of top circular geometry of bluff body
Re_a	Acceleration Reynolds number
Re_d	Deceleration Reynolds number
Re_b	Flow Reynolds number (Bluff body) case
Re_h	Flow Reynolds number (diverging channel) case
Re_δ, Re_{δ^*}	Reynolds number based on viscous length scales
t	Flow time
t_0	End of acceleration phase
t_1	End of constant velocity phase
t_2	End of deceleration phase
t^*	Non-dimensional flow time
t^*_D	Non-dimensional deceleration time
t^*_s	Non-dimensional flow separation time
t^*_v	Non-dimensional vortex formation time
t^*_{3D}	Non-dimensional secondary instability initiation time
U_p	Constant mean velocity
U_{tv}	Mean inflow velocity at t_v
U_{rms}	Root mean square deviation of streamwise velocity component
$\mathbf{V}$	Velocity vector

w^*_{rms}	Non-dimensional RMS of spanwise velocity component
(u, v, w)	Velocity components in streamwise, wall-normal, and spanwise direction
(x^*, y^*, z^*)	Non-dimensional length scales for bluff body cases
(x, y, z)	Non-dimensional length scales for diverging channel cases
(X_c, Y_c)	Vortex core position
ν	Kinematic Viscosity
ϵ	Immersed boundary coefficient
τ	Non-dimensional acceleration time
β	Separation angle
δ, δ^*	Boundary layer thickness and Displacement thickness
θ	Momentum thickness
σ	DMD growth rate
σ^*	Theoretical growth rate
λ	Spanwise oscillation wavelength
λ_2	Second largest eigenvalue used for vortex identification
$\lambda_{Re}, \lambda_{Im}$	Real and Imaginary parts of eigenvalues
Γ	Circulation
(α_D, β_D)	Constants for velocity approximation in diverging channel case
$(\omega_x, \omega_y, \omega_z)$	Vorticity components in streamwise, wall-normal, and spanwise direction

Chapter 1

Introduction

The onset of turbulence of the wake vortices associated with separation from the transitional boundary layer is a long-standing fluid dynamics problem that has intrigued researchers. Periodic coherent structures formed from an unsteady separation under transient inlet conditions can influence the performance of many engineering systems. A few practical situations showing flow separation and associated instabilities originating in the wake of the body are shown in figure 1.1. Other examples include internal flow in hydraulic devices and

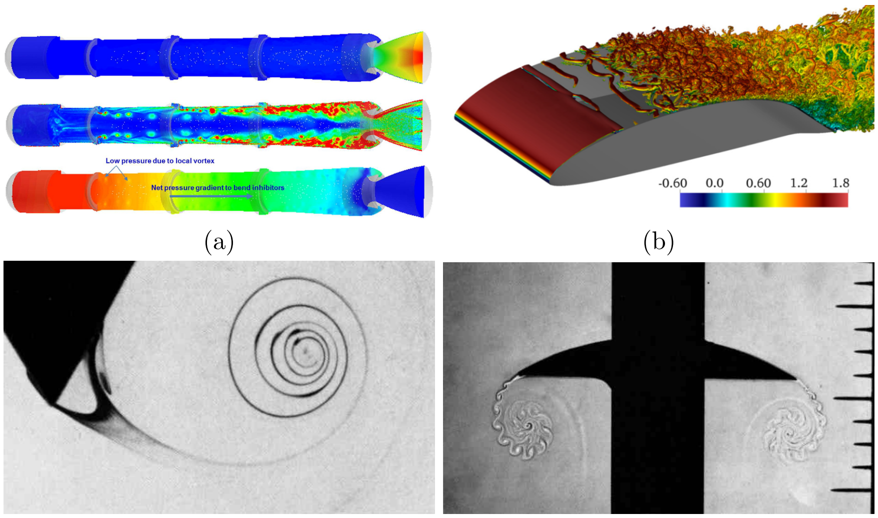

(a) (b)

(c) (d)

Figure 1.1: (a) Vortex shedding process inside a solid rocket motor (SRM) with rigid inhibitor contoured by instantaneous Mach number (top), vorticity field (middle), and pressure field (bottom) from the simulations of Yang et al. [5], (b) λ_2 structures identified through simulation of boundary layer transition over an airfoil [6], (c) starting flow vortex formation over a wedge experimentally visualized by Pullin and Perry [7], and (d) experimental images of shear layer shedding over an accelerated plate by Pierce [8].

physiological flows (blood flow in the aorta), the sudden closure of valves in pipe flows, turbo-machinery control, vortex shedding from ship funnels, and wind flow over hills. For example, the vortex-shedding process from the inhibitor in a solid rocket motor (SRM) is an essential concern for design engineers (figure 1.1 (a)). Such vortices generated from the inhibitors can lead to thrust oscillations in launch vehicles and damage the payload.

Unsteady flow separation and associated flow transitions also significantly affect airfoil and turbine performance, constituting a significant design concern (figure 1.1 (b)). For instance, the performance of turbo-machines, including pumps, turbines, and compressors, is adversely affected by the flow separation occurring from adverse pressure gradient (APG) conditions [9, 10]. A recent review by Sandberg and Michelassi [9] summarizes the consequences of flow separation and various modeling approaches in axial turbo-machines. During such complex real-world applications involving APG conditions, the boundary layer thickness can vary spatially and temporally, bringing about a set of inflectional velocity profiles at random times and points along the surface, making the investigation difficult.

Several computational, theoretical, and experimental studies have explored the flow dynamics of a bluff body maintained in a constant velocity field. Extensive reviews elucidating wake vortex dynamics of bluff bodies held in a uniform flow field utilizing diverse standpoints have been reported in Roshko [11], Williamson [12], and Thompson et al. [13]. Conversely, the flow dynamics of the bluff body in oscillatory (zero mean) and pulsating flows (non-zero mean) have received relatively lesser attention. Unlike a steady/oscillatory inflow velocity, a transient inflow condition can induce a multitude of flow formations like separation bubbles, transient vortex growth (figure 1.1 (c)), shear layer shedding (figure 1.1 (d)), and further transit into a highly complex three-dimensional flow.

A closer look into the three-dimensional oscillations evolving inside the vortex structures exhibits different interactions, like straining or stretching, between neighboring vortices which leads to instability development and then transition. Investigations on the instability development in counter-rotating vortex pairs in quiescent fluid have shown that different instability patterns can occur, with significant variations in the spanwise wavelength [14, 15, 16]. Similar studies of the merging of co-rotating vortical flow features that develop from a velocity shear layer reveal an unstable braid region between consequent vortex structures susceptible to spanwise oscillation growth[17, 18, 19]. Subsequently, the investigations comparing the nature and transitional mechanism in wake vortices displayed close similarities between three-dimensional instabilities in the cylinder wake with vortical instability mechanisms [20, 21].

Early investigations of flow transition were restricted to academic geometries because of the limited availability of experimental and computational resources. Still, a large number of researchers relied on direct numerical simulations to identify the physical mechanism involved in different wake transition problems [22, 23, 24]. The simulations, however, were limited by simple shapes due to the complexity of the domains with body-fitted grids, making numerical discretization time-consuming and computationally expensive. An approach to modeling fluid-structure interactions in biological flows through a set of discrete points that are considered "immersed" within the fluid, called the immersed boundary method (IBM), was outlined by Peskin [25]. A recent consolidated review by Verzicco [26] provides a detailed explanation of the background for the development of IBM, its advantages, and limitations over conventional methods.

A transient inflow can induce or alter the flow characteristics, even for flat plates or streamlined bodies [27]. It is often the case that the temporal pressure gradient distribution varies with the nature of the pulse, causing inflectional profiles in the boundary layer, with or without reverse flow. The effects of spatial and temporal pressure gradient conditions on vortex formation and associated instabilities have been extensively examined experimentally under trapezoidal mean flow conditions coupled with various geometrical configurations [1, 2, 3, 28]. Trapezoidal flows, in contrast to pulsating ones, are appropriate for investigating the effects of constant acceleration and deceleration on flow dynamics. Das et al. [1] analyzed flow structures originating from bluff bodies and critical time scales for similar mean flow conditions. Recently, Ramalingam and Das [28] performed a detailed visualization study on the flow structures in a water channel flow using direct visualization and particle image velocimetry.

Stability analysis of transitional flow fields involving spatiotemporal boundary layer variations is more complex than conventional problems consisting only of spatial or temporal variations. In order to gain further insight into the dynamics of coherent flow features, the data assimilation algorithm makes it practical to determine the stability of a flow field directly from the data. Dynamic mode decomposition (DMD) is a data-driven method to identify the spatial and temporal coherent flow features underlying a fluid flow field. DMD algorithm was initially proposed by Schmid [29] to identify coherent flow features in flow field data from both numerical and experimental methods. In recent years, DMD has become a popular dimensionality reduction technique due to its ability to factorize complex data sets efficiently [30, 31, 32]. Decomposing a flow field into its elemental flow features can help us to predict how the flow will develop in the future and how to control it. Dynamic mode decomposition is a simple and computationally flexible method that is ideal for this task, especially in transitional data sets that are difficult to analyze with conventional methods.

The current investigation of the transition of the wake vortices due to a spatiotemporal boundary layer variation is pivoted on two geometries. Geometries are carefully chosen to represent adverse pressure gradient conditions developed in real-life engineering designs. The first one represents the bodies offering a strong spatial gradient (bluff body) component with a large velocity shear region with a short separation bubble. The second one offers a low spatial pressure gradient (diverging channel), thus leading to a smaller velocity shear region and a long separation bubble.

1.1 Overview of literature

Early studies on the transition dynamics of the vortex flow features were carried out using isolated vortices [33] or using academic geometries like cylinder [20], or other axisymmetric bodies [34]. Visualizations of different three-dimensional flows identify the common traits in instability growth and further disintegration. Additionally, numerical simulations are frequently employed to investigate the effects of periodic external oscillations on separation flow dynamics [35]. In a stepped channel, Tutty and Pedley [36] analyzed the formation and propagation of ‘vortex waves’ generated during an oscillatory flow’s forward and backward phase using two-dimensional simulations. Alternatively, Rosenfeld [37] examined the influence of the Reynolds number and Strouhal number on vortex formation and propagation in a constricted channel. Wissink and Rodi [38] investigated the effect of oscillatory flow in transitional separated flow over a smooth converging and diverging section by employing three-dimensional numerical simulations. Wissink et al. [39] further investigated the heat transfer aspects of a laminar separation bubble affected by the oscillating external flow.

Similarly, the stability of flows with non-zero mean velocity has been investigated in several studies. Through a quasi-steady approach, Hall and Parker [40] investigated the growth of the disturbance velocity field associated with the inflectional velocity profiles in a decaying laminar flow. Based on a linear instability analysis of the inflectional velocity profiles generated in an oscillating pipe flow, a relationship between the flow stability and inflection point was posited by Das and Arakeri [3]. The wave number associated with the highest growth rate for such profiles is nearly constant. Additionally, a linear and weakly nonlinear analysis of a laminar flow subjected to rapid acceleration/deceleration by Ghidaoui and Kolyshkin [41] reinterprets the stability region predicted by Das and Arakeri [3]. Furthermore, it was discovered that the Ginzburg-Landau equation governs the amplitude of the most unstable mode. Using optimal growth analysis of normal modes, Nayak and Das [42] provides accurate growth rate predictions for unsteady channel flows. Recently, Kannaiyan et al. [43] investigated the stability characteristics of laminar pipe flow with a step-like flow rate increment by using a linear modal stability framework combined with a quasi-steady assumption.

1.1.1 Bluff body wake

Some of the early works on the cylinder wake by Stokes [44] and von Kármán initiated the quest of researchers to model the bluff body wakes. Despite the boundaries of experimental and numerical resources, extensive research in the cylinder wake uncovers the vortex shedding and shear layer instability mechanisms [45, 46, 47, 48, 49]. The effect of Reynolds and Strouhal number on the wave formation and propagation of the primary and secondary vortices on constricted channels with time-dependent inlet flow conditions (sinusoidal variation) was studied by Tutty and Pedley [50], and Rosenfeld[51]. A comparison of boundary layer transition and coherent structures between steady and unsteady flows was performed by Costamagna *et al.* [52]. They posited that the elementary process causing the turbulence in oscillatory flows is analogous to the steady flow cases.

Multiple researchers have analyzed the secondary instability and the transition of shear layer vortices resulting from separated flows [53, 54, 55, 56]. Shear layer vortices are susceptible to secondary instability in the elliptic and hyperbolic regions (core and braid regions, respectively), resulting in periodic streamwise vortex formation. For example, Mode A and Mode B instabilities in the transitional cylinder wake correspond to elliptic and hyperbolic instability in the wake vortices, respectively [20]. Caulfield and Kerswell [54] mathematically described the braid region instability arising over the hyperbolic stagnation points in mixing layer flows. Jones et al. [53] has confirmed the destabilization of the braid region between vortex structures emerging from a separated flow over the surface of an airfoil and relates it to the mode-B instability of hyperbolic streamlines in two dimensions; the same is often true for bluff-body wakes.

Many aspects of flow transition in oscillatory and pulsating flows are delineated through the analytical solution, exponent, and transient instability analyses. Through a laminar stability analysis of time-dependent flows combined with a momentary stability assumption, Shen [57] investigated the destabilizing nature of decelerating flows. Detailed instability analysis of inflectional velocity profiles formed during the decelerating phase of pulsating pipe flow was conducted by Das and Arakeri [3]. A good quantitative agreement with

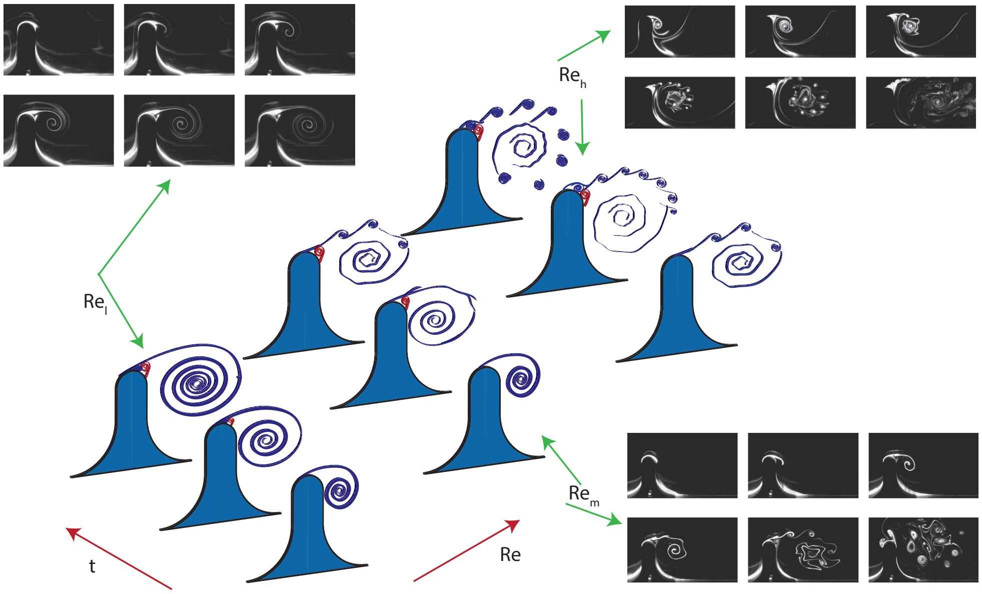

Figure 1.2: Schematic depiction of the main flow pattern at three different Reynolds numbers as in the study of Das *et al.* [1] Experimental figures are reproduced with permission from Das *et al.*, [1] Journal of Fluids and Structures 40 (2013). Copyright 2013 Elsevier.

experiment and linear instability analyses was obtained for decelerating flows containing inflection points [3]. They posited that flow breakdown could be due to inflectional inviscid instability. Similarly, Zhao et al. [58] analyzed the growth of the perturbation in different transient pipe flow conditions by considering it as a linearized initial value problem. Xu et al. [59] recently performed a non-modal analysis of unsteady internal flows to investigate their stability characteristics.

Das *et al.*[1] conducted experiments in a closed-loop unsteady water tunnel to study the initiation of separation from a bluff body for trapezoidal-type mean inflow variation with flow time in a channel flow. The flow configuration and salient flow features of Das *et al.*[1] experiments are depicted in figure 1.2. Flow characteristics around a bluff body vary with respect to the Reynolds number, which is calculated using the diameter of the top circular geometry $\left(Re_b = \frac{U_p b}{\nu}\right)$. In the experiments of Das *et al.*[1] at low Reynolds number case ($Re_l \approx 100$), the flow separated in the leeward side of the body, and the size of the separation bubble increased with flow time (figure 1.2). At a moderate Reynolds number ($Re_m \approx 700$), the shear layer becomes unstable, leading to the formation of shear layer vortices. At a high Reynolds number ($Re_h \approx 2300$), the shear layer breaks down quickly. A fascinating circular array of shear layer vortices was observed on the circumference of the primary large-scale vortex. Many features of the shear layer breakdown mechanism were reminiscent of the two-dimensional Bloor-Gerrard instability/secondary

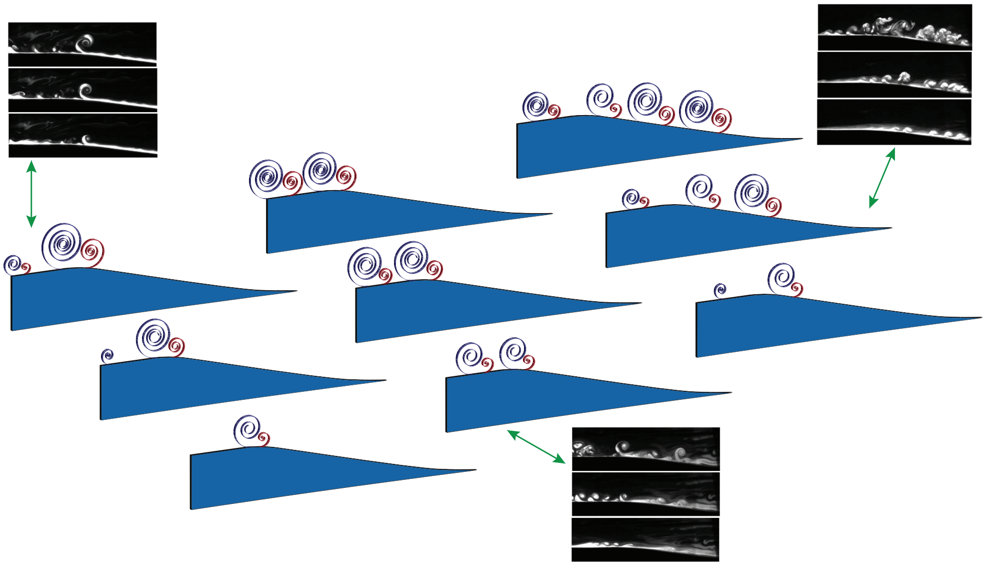

Figure 1.3: Schematic depiction of the main flow pattern at three different Reynolds numbers as in the study of Das *et al.* The experimental figure is reproduced with permission from Das *et al.*, [2] European Journal of Mechanics - B/Fluids 55 (2013). Copyright 2016 Elsevier Masson. [2]

vortices[45, 60] observed in steady inflow cases.

1.1.2 Diverging channel flow

Existing studies are focused on the effect of the APG variation induced by spatial components on the separation dynamics and flow stability under constant/oscillating inflow conditions. Likewise, the earlier works describe flow stability in such flow conditions where the adverse pressure gradient arises from the placement of a horizontal cylinder[45, 61] or by a combination of spatial contours [38] or integrating blowing/suction [62, 63] onto the wall. In such cases, the inflectional velocity profiles developed due to APG conditions can lead to separation, instability, or both. Flow development in real-life scenarios involves an unsteady boundary layer due to spatial as well as temporal variations.

The stability and transition mechanisms in the Adverse Pressure Gradient (APG) boundary layer have been studied extensively [64, 65, 66], given their frequent appearance in various engineering applications. Historically, separation bubble formation and growth were isolatedly investigated employing blowing/suction [62, 63], spatially varying wall contours [67], and attaching distinctive shapes to the wall [38, 68]. Further, the receptivity analysis is extensively used to delineate the mechanism that amplifies or decays the velocity field disturbances within the boundary layer of laminar and marginally separated flows ([69, 70, 71]). These studies demonstrated the Lambda vortex-induced breakdown of a separated shear layer occurs in short laminar bubbles and their absolute instability nature. Despite the absence of disturbances upstream, the disintegration produced by separation bubbles was characterized by the evolution of low-frequency oscillations with a high amplitude within itself [72]. A time-varying external flow or free-stream turbulence may enhance or reduce an adverse pressure gradient and alter the separation location over time, further complicating the problem. Hence the effect of unsteady inflow conditions on non-uniform channels has been the subject of many studies [1, 2, 36, 37, 38, 39].

Das et al. [2] conducted a fascinating experimental investigation in a diverging water channel to investigate the transition mechanism in APG conditions. A schematic illustration of the vortex flow structures observed in these experiments is shown in figure 1.3. In response to two-dimensional inflectional instabilities, an apparent roll-up of the shear layer is observed in both the lower and upper walls. Clear dye roll formation indicates two-dimensional vortex formation for low inflow velocities. One crucial experimental observation in their study was the highly localized transition to turbulence of shear layer vortices generated by primary instability. Further, in some cases, the formation of thick vortex clouds spans all over the diverging section pointing to an advective nature of vortices. Though a three-dimensional disintegration of vortices was identified, the spatial and temporal nature of instability still remains a mystery due to experimental constraints.

A study by Abdalla and Yang [73] demonstrated that the onset of turbulence could be attributed to a helical pairing of spanwise vortex rolls originating from Kelvin-Helmholtz instability. For the vortices shed from laminar separation bubbles, Marxen et al. [74] posited multiple instability mechanisms that lead to turbulent transitions. The first mechanism, identified as elliptical instability, distorts the vortex structure with a spanwise wavelength in the order of the vortex dimension. In contrast, the other instability develops in the braid region with a higher spanwise wave number.

1.2 Motivation and Objectives

An extensive literature review revealed that there is a dearth of literature examining the flow instabilities that arise following a transitional boundary layer. In the current investigation, the spatial component is taken into consideration by choosing two different bodies: a wall-attached bluff body with a strong spatial gradient and a slowly diverging channel with a weak spatial gradient component. The challenge of efficiently representing transitional flows in complex geometry is addressed by using the immersed boundary method in conjunction with higher-order compact schemes. The computationally economical immersed boundary method will allow the imposing of complex geometries using a Cartesian grid. The free-stream velocity varies temporally, similar to the unsteady water tunnel experimental studies [1, 2]. However, Das et al. [1] did not explore three-dimensional wake dynamics or the effect of acceleration and deceleration Reynolds numbers on flow instability.

Unlike sinusoidal variation of the mean flow, trapezoidal piston motion allows the analysis of flow transitions in constant acceleration/deceleration flow conditions. Here, the boundary layer is contingent on an adverse pressure gradient because of both the temporal and spatial components of the pressure gradient, which can obscure the flow dynamics and escalate the level of complexity. By studying velocity profiles, we examine the primary mechanism of instability, while streamwise vorticity analyses are used to study the secondary instability mechanism. The stability of coherent flow structures and their temporal characteristics are further investigated using DMD analysis, a well-established reduced-order modeling approach. In addition, the vortex's stability analysis is conducted using theoretical growth rate estimates using the vortex parameters identified from a comparable Lamb-Oseen approximation. Through the use of modal decomposition strategies and theoretical modeling, the current research aims to delineate three-dimensional instability mechanisms of wake vortices associated with a transitional boundary layer.

1.3 Thesis Outline

Chapters of the current thesis are arranged into seven chapters. This thesis focuses on identifying the vortex breakdown mechanisms in an unsteady boundary layer subjected to adverse pressure gradient conditions. The details of the computational solver, along with domain and boundary conditions, are described in Chapter 2. Additionally, this chapter describes the methodologies adopted in the current investigation to characterize different instability mechanisms. A discussion of the initial flow features is identified in the wake of a wall-attached bluff body, and the effects of the temporal parameters are presented in Chapter 3. Chapter 4 discusses in detail the three-dimensional flow features and coherent flow features identified through DMD analysis. Chapter 5 discusses flow evolution in the diverging channel, including the classification of flow cases based on secondary instability initiation time. The various modes of DMD and the theoretical stability analysis of the vortex flow features formed over a diverging channel are presented in chapter 6. As a final chapter, Chapter 7 concludes the current investigation with a detailed discussion and comparison of the instability mechanisms and their salient features evidenced for both geometries.

Chapter 2

Computational Methodology and Instability Analysis

2.1 Introduction

In the present work, direct numerical simulations are employed to simulate the transitional flow past a geometry under an unsteady inflow condition. Such transitional flows pose a challenge for researchers since they require higher-order methods combined with extensive computational resources to simulate a complex body embedded within the computational domain. With the advancement of higher-order numerical schemes for simulating flow development and the growth in computing power, simulations of transient flow problems have become feasible. The higher-order compact schemes and the IBM method equip INCOMPACT3D to efficiently associate complex geometries in Cartesian mesh for high-fidelity DNS simulations [4]. Numerical simulations in the current study are carried out in a high-performance cluster computing system using an open-source INCOMPACT3D, which incorporates domain decomposition techniques for parallel processing.

High-dimensional data obtained through direct numerical simulations are further analyzed to identify the flow evolution and the underlying instability mechanisms. Dynamic mode decomposition, similar to proper orthogonal decomposition (POD), is a data-driven method to identify the underlying spatial and temporal coherent flow feature characteristics in a fluid flow field. The algorithm initially proposed by Schmid [29] identifies the modes equivalent to global stability analysis. For non-linear flows, the technique identifies the linearly tangent flow features that will dominate during the flow sequence. DMD can yield spatial modes based on their frequency values, making it a convenient technique for investigating systems involving multiple frequency scales, as in the present study.

A comprehensive discussion on the spatial discretization scheme and modified pressure

Poisson solver, along with a detailed description of the solution procedure to obtain the temporal variation in the inflow velocity profile, is provided in section 2.2. Details on the governing equations and solution procedures, along with velocity profiles imposed at the inlet during different phases, can be found in section 2.3. In addition, this chapter also includes a detailed explanation of Rayleigh's instability criteria for identifying the primary instability mechanism and spectra analysis to isolate the underlying temporal characteristics of the fluctuations in the velocity field in section 2.4. Further, an in-depth explanation of the mathematical approach for obtaining the DMD modes and their associated time dynamics is provided in the section 2.5 of the current chapter.

2.2 Computational methodology

The time-dependent three-dimensional flow field is obtained by solving the following governing equations. The continuity and momentum equations for a three-dimensional, incompressible, and viscous flow are given by,

$$\begin{gathered} \nabla \cdot \mathbf{V} = 0, \\ \frac{\partial \mathbf{V}}{\partial t} = -\nabla p - \frac{1}{2}\left[\nabla(\mathbf{V} \otimes \mathbf{V}) + (\mathbf{V} \cdot \nabla)\mathbf{V}\right] + \nu \nabla^2 \mathbf{V} + f. \end{gathered} \tag{2.1}$$

In the above equation, $\mathbf{V}$ is the velocity vector with components u, v, and w in streamwise, wall-normal, and spanwise directions. Here, $t,\ p,\ \nu$ correspond to flow time, pressure, and kinematic viscosity. Using a higher-order finite difference scheme may induce aliasing errors to develop and perturb the solution field. Dealiasing can reduce such conditions when using the spectral methods for the divergence and convective terms, while the skew-symmetric and rotational forms are energy-conserving even without dealiasing [75]. A forcing field is incorporated in the governing equation (equations 2.1) to employ the immersed boundary method, and the details can be found in the following section.

2.2.1 Time advancement

Time advancement of the discretized governing equation is carried out using the following formulation:

$$\begin{aligned} \frac{\mathbf{V}^* - \mathbf{V}^k}{\Delta t} &= a_k \mathbf{F}^k + b_k \mathbf{F}^{k-1} + c_k \mathbf{F}^{k-2} - d_k \nabla \tilde{p}^k + d_k \tilde{\mathbf{f}}^{k+1}, \\ \frac{\mathbf{V}^{**} - \mathbf{V}^*}{\Delta t} &= d_k \nabla \tilde{p}^k, \end{aligned}$$

$$
\begin{aligned}
\nabla \cdot \nabla \tilde{p}^{k+1} &= \frac{\nabla[(1-\epsilon)\mathbf{V}^{**}]}{d_k \Delta t}, \\
\frac{\mathbf{V}^{k+1} - \mathbf{V}^{**}}{\Delta t} &= -d_k \nabla \tilde{p}^{k+1},
\end{aligned}
\tag{2.2}
$$

where $\mathbf{F}^k = -\frac{1}{2}[\nabla(\mathbf{V}^k \otimes \mathbf{V}^k) + (\mathbf{V}^k.\nabla)\mathbf{V}^k] + \nu\nabla^2\mathbf{V}^k$, and forcing term $d_k\tilde{f}^{k+1} = \epsilon\big(-a_kF^k - b_kF^{k-1} - c_kF^{k-2} + d_k\nabla\tilde{p}^k + \frac{\mathbf{V}_0^{k+1} - \mathbf{V}^k}{\Delta t}\big)$. For third order Adam-Bashforth scheme the coefficients a_k, b_k, c_k, and d_k are respectively $\frac{23}{12}$, $\frac{-16}{12}$, $\frac{5}{12}$, 1. The immersed boundary method is employed through the ϵ value; the ϵ takes the value 1 inside the body region, while it is 0 elsewhere.

The simulation begins with the user-defined initial condition or by reading the previously saved restart file. This allows the user to start the simulation at any desired point and see the results of the simulation progress over time. Further, any user-defined initial conditions can be used to set up the parameters of the simulation so that they accurately reflect the experimental conditions. The fractional step method advances in time as given by equations 2.2. As per the first equation, an intermediate velocity field ($\mathbf{V}^*$) is obtained from the current time step values. Simulation moves forward by updating the intermediate velocity by applying the boundary conditions ($\mathbf{V}^{**}$), and then the pressure field for the next time step is evaluated by solving the Poisson equation relating the divergence of the intermediate velocity field to the divergence of the pressure gradient using spectral methods. Finally, the velocity field for the next time step is calculated using the updated pressure gradient and intermediate velocity field.

2.2.1.1 Time integration schemes

The current solver configuration supports different time integration schemes, including Runge-Kutta (RK) and Adam-Bashforth (AB) schemes. In the Runge-Kutta method, each time step value is computed using sub-steps instead of previous time step values. The major drawback is the increased computational cost of calculating the sub-step values. In contrast, Adam-Bashforth schemes rely on the previous time step values to calculate the current time step values, an extension of Euler schemes. Comparing the simulation results with both methods indicates that for the current problem, the Adam-Bashforth method produces results with identical accuracy in a shorter computational period than the Runge-Kutta method. Our current investigation uses third-order Adam-Bashforth as the time integration scheme. In the third-order Adam-Bashforth scheme, the next time step value is calculated as:

$$U^{k+1} = U^k + \frac{\Delta t}{12} \times \left(23U^k - 16U^{k-1} + 5U^{k-2}\right). \tag{2.3}$$

2.2.2 Spatial discretization

The spatial discretization of the governing equation is carried out using compact scheme formulation proposed by Lele [76]. The approximation of the first derivative (U') of a function $U(x)$ can be expressed in the form

$$\alpha U'_{i-1} + U'_i + \alpha U'_{i+1} = a\frac{U_{i+1} - U_{i-1}}{2\Delta x} + b\frac{U_{i+2} - U_{i-2}}{4\Delta x}, \tag{2.4}$$

where $\alpha = 1/3$, $a = 14/9$, $b = 1/9$ achieving a “quasi-spectral behaviour". For second-order differentiation, the approximation is obtained as follows:

$$\alpha U''_{i-1} + U''_i + \alpha U''_{i+1} = a\frac{U_{i+1} - 2U_i + U_{i-1}}{\Delta x^2} + b\frac{U_{i+2} - 2U_i + U_{i-2}}{4\Delta x^2} + c\frac{U_{i+3} - 2U_i + U_{i-3}}{9\Delta x^2}. \tag{2.5}$$

The scheme attains sixth-order accuracy with controlled aliasing errors by choosing $\alpha = 0.47959871686180711$, $a = 0.42090288706093404$, $b = 1 : 7020738409366740$, $c = -0.16377929427399390$. Free slip conditions are enforced by the use of ghost cells (U_0, U_{-1}, U_{nx+1}, U_{nx+2}) by substitution of their counterparts (U_1, U_2, U_{nx-1}, U_{nx-2}). To enforce the no-slip or Dirichlet boundary condition, third-order accurate single-sided formulations are used for the boundary cells, while fourth-order accurate Padé schemes are used for their adjacent nodes. The three-point implicit formulation of discretized convective and viscous terms enables us to solve using the inverse tridiagonal matrix algorithm (TDMA).

2.2.3 Pressure computation

Unlike the classical fractional method in which the incompressibility condition is verified at the end of each sub-time step through solving the Poisson equation, the implementation of Immerse Boundary Method (IBM) requires a direct forcing method leading to a modified pressure Poisson equation as given in equation 2.2 which will result in a conventional Poisson equation when $\epsilon = 0$. While the internal velocity inside the body is defined through the placement of a mass source/sink inside the body region, and therefore the divergence condition modifies into:

$$\nabla \cdot \mathbf{V}^{k+1} = \nabla \cdot (\epsilon \mathbf{V}_0^{k+1}). \tag{2.6}$$

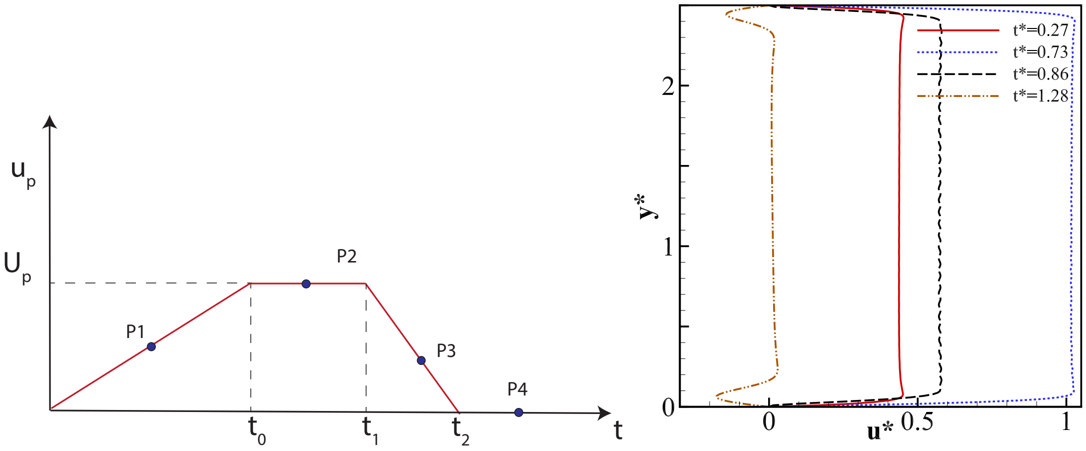

(a) (b)

Figure 2.1: Inflow boundary condition. (a) temporal variation of mean velocity; (b) inlet velocity profiles ($u^* = u/U_p$) at four different flow times.

Such an artificial flow maintains the solution regularity when spatial discretization involves high-order schemes.

The solution of the pressure Poisson equation involves high computation cost due to the inversion of the Poisson equation combined with high-order finite difference schemes. The current solution algorithm depends on the Fourier space for the equivalent operations. A staggered pressure grid is used for the pressure treatment to avoid spurious pressure oscillations [77]. 2Decomp&FFT [78], a domain decomposition library, performs Fast Fourier Transforms involved in spectral techniques. The library also contains a domain decomposition algorithm for efficient scaling and distribution of memory in high-performance computing systems.

2.3 Inflow generation

The current study involves temporally varying mean inflow, akin to the piston motion in the novel experiments of Das et al. [1]. Figure 2.1 shows the trapezoidal temporal inflow variation used in the present study. The single pulse configuration (figure 2.1 (a)) has four phases, as expressed in equation 2.7. In the initial phase of the trapezoidal pulse ($0 < t < t_0$), the mean flow undergoes a constant acceleration, followed by a constant-velocity phase ($t_0 < t < t_1$), and a constant-deceleration phase ($t_1 < t < t_2$). The mean velocity is zero for $t > t_2$. Hence the effect of acceleration and deceleration can be studied separately in phases one and three, respectively, through the variation in parameters t_0, t_1, and t_2.

$$\begin{aligned} u_p(t) &= U_p \frac{t}{t_0} \quad \text{for} \quad 0 \leq t \leq t_0, \\ &= U_p \quad \text{for} \quad t_0 \leq t \leq t_1, \\ &= U_p \frac{(t_2 - t)}{(t_2 - t_1)} \quad \text{for} \quad t_1 \leq t \leq t_2, \\ &= 0 \quad \text{for} \quad t > t_2. \end{aligned} \tag{2.7}$$

Since the velocity profiles will be fully developed at the body location, providing analytical solutions helps reduce computational costs. Also, the most straightforward way of giving the mean flow at the inlet of the computational domain and calculating the velocity profiles was computationally demanding. The general analytical solution of velocity profiles for trapezoidal mean flow variation in two-dimensional channel flow can be expressed as an infinite series [27]. To reduce the size of the computational domain and associated computational resources, the time-dependent boundary condition from the analytical solution given by Das and Arakeri [27] is imposed at the inlet of the computational domain (equation 2.8). Figure 2.1 (b) shows the velocity profile given at the inlet corresponding to each temporal point (P1-P4) highlighted in figure 2.1 (a). In addition, the non-dimensional time based on the pulse period (t_2) is also indicated in figure 2.1 (b). The usage of the analytical solution has been found computationally robust.

Analytical velocity solutions are obtained through the technique proposed by Das and Arakeri [3]. The governing partial differential equations with variable $u(x, t)$ are converted into ordinary differential equations with the Laplace transforms ($\tilde{u}(x, s)$). The ordinary differential equation is solved for $\tilde{u}(x, s)$, and the function is inverted to yield $u(x, t)$ using the Bromwich integral formula. Details of the derivations of analytical solutions and procedures are provided in the appendix (A). The velocity profiles obtained analytically during different phases are shown in figure 2.1 (b).

For single pulse cases, the analytical solutions are:

$$\begin{aligned} &\text{for} \quad 0 \leq t \leq t_0 \\ &\frac{u}{U_p} \;=\; \frac{1}{t_0}\left(A_1 t - \frac{K A_2}{40}\right) - \frac{2K}{t_0} \sum_{nh=1}^{\infty} \left(e^{\left(\frac{-\mathrm{v}_{nh}^2 t}{K}\right)}\right) \times \Psi, \end{aligned} \tag{2.8}$$

$$
\begin{aligned}
&\text{for}\quad t_0 \leq t \leq t_1\\
\frac{u}{U_p} &= A_1 - \frac{2K}{t_0}\sum_{nh=1}^{\infty}\left(e^{\left(\frac{-\mathrm{v}_{nh}^2 t}{K}\right)} - e^{\left(\frac{-\mathrm{v}_{nh}^2 (t-t_0)}{K}\right)}\right) \times \Psi,\\
&\text{for}\quad t_1 \leq t \leq t_2\\
\frac{u}{U_p} &= A_1\left(\frac{t_2 - t}{t_2 - t_1}\right) + \frac{KA_2}{40\left(t_2 - t_1\right)}\\
&\quad -2K\sum_{nh=1}^{\infty}\left(\frac{e^{\left(\frac{-\mathrm{v}_{nh}^2 t}{K}\right)} - e^{\left(\frac{-\mathrm{v}_{nh}^2 (t-t_0)}{K}\right)}}{t_0} - \frac{e^{\left(\frac{-\mathrm{v}_{nh}^2 (t-t_1)}{K}\right)}}{t_2 - t_1}\right) \times \Psi,\\
&\text{for}\quad t_2 \leq t < \infty\\
\frac{u}{U_p} &= -2K\sum_{nh=1}^{\infty}\left(\frac{e^{\left(\frac{-\mathrm{v}_{nh}^2 t}{K}\right)} - e^{\left(\frac{-\mathrm{v}_{nh}^2 (t-t_0)}{K}\right)}}{t_0} - \frac{e^{\left(\frac{-\mathrm{v}_{nh}^2 (t-t_2)}{K}\right)} - e^{\left(\frac{-\mathrm{v}_{nh}^2 (t-t_1)}{K}\right)}}{t_2 - t_1}\right) \times \Psi,\\
where\quad A_1 &= \frac{3}{2}\left(1 - c_h^2\right), \quad A_2 = 5c_h^4 - 6c_h^2 + 1, \quad K = \frac{h^2}{\nu},\\
\Psi &= \left[\frac{cos(c_h\mathrm{v}_{nh}) - cos(\mathrm{v}_{nh})}{\mathrm{v}_{nh}^3 sin(\mathrm{v}_{nh})}\right].
\end{aligned}
$$

Here, h is the channel half height, y is the distance from the center line towards the wall of the channel, $c_h = \frac{y}{h}$, and v_{nh}, nh = 1,2,3,... ∞ are roots of $tan(\mathrm{v}) = \mathrm{v}$. Here, the first fifty roots of $tan(\mathrm{v}) = \mathrm{v}$ are used to obtain the sum of the above converging infinite series.

2.4 Instability characterization methodologies

The transition mechanism in an unsteady flow evolution involves various instability mechanisms. Different methods are employed in the analysis of instability mechanisms focusing on the nature and temporal characteristics. Flow separation due to the primary inflectional instability is identified through the velocity profile over the separation point. As the flow progresses, the separated shear layer induces oscillation creating further shedding of vortices. Shedding frequency is identified through probe analysis and corresponding spectra analysis. In addition, data-driven methods like Dynamic Mode Decomposition (DMD) developed in recent years extract both the temporal and spatial characteristics of the coherent flow features and are utilized to investigate the underlying flow features. Compared to the more established POD method, the DMD algorithm extracts temporal information and can reconstruct the system dynamics, making it more suitable for complex transient flows.

2.4.1 Primary Instability or Flow separation

The classical linear stability theory by Rayleigh[79] identified a point of inflection as a necessary condition in inviscid plane-parallel shear flows and was later established as a sufficient condition for disturbance amplification by Tollmien [80]. Rayleigh's equation, also known as the friction-less stability equation, is obtained by considering a small amplitude perturbation stream function substituted into the two-dimensional Euler equation for shear flow and is given by:

$$(\overline{U} - c)(D^2 - k^2)\Psi_s - \overline{U}_{yy}\Psi_s = 0. \tag{2.9}$$

Integrating equation 2.9 to determine the stability leads to identifying the necessary condition for stability as the change in sign of the term $\overline{U}_{yy}$. An adverse pressure gradient arising from geometry-induced or temporally-induced flow deceleration or both can further lead to flow separation. The instability nature of such separated flows is examined through the streamwise velocity profiles. In the current investigation, inflectional velocity profiles are formed in both cases, which may lead to boundary layer separation, instability, or both. The flow separation and inflectional instability are quantified through the velocity profile through the zero wall shear stress point. In addition, the point of inflection is identified through the analysis of the point of sign reversal in the second derivative of the velocity profile.

2.4.2 Temporal characteristics

In the current investigation, the vortex shedding frequency is identified from the temporal variation of the vertical velocity component and momentum thickness oscillations. Since the vertical velocity component is imposed to be zero, the development of oscillations in the vertical velocity component can be considered as a reflection of boundary layer oscillations, tailoring it to analyze the temporal characteristics. Also, the temporal window selected for the frequency analysis is chosen between the constant velocity period to remove any temporal anomaly due to the change of the mean inflow phase. Boundary layer integral parameters such as displacement and momentum thicknesses are calculated using the left Riemann sum rule with dy as the interval length and grid point as the quadrature point. Data from a probe taken over the shear layer is transformed using Fourier transforms to determine the underlying frequency spectrum. Fast Fourier Transformation arises as a computationally fast and efficient way to compute Discrete Fourier Transform (DFT) for a signal from its original domain to the frequency domain. DFT mathematically decomposes a sequence of values into their individual frequency components. Though the initial development of the FFT algorithm is in the field of digital signal processing, the wide applicability of the method for extracting frequency information from sequential data makes it ideal for secondary instability frequency calculation. The present study made use of the inbuilt FFT algorithm in Tecplot software combined with a rectangular window function. Temporal data for the frequency calculation is extracted through data probing and by calculating the momentum thickness across the shear layer avoiding the top and bottom boundary layers.

2.5 Dynamic Mode Decomposition

The inherent limitations in the computational power also restricted the global stability analysis of the complex flow fields, especially when the flow field involves complex geometries. Alternatively, for large data sets of complex flow fields, Proper Orthogonal Decomposition (POD) is established to identify spatial orthogonal modes ranked by their energy but lacks crucial temporal information and therefore loses the instability growth characteristics. In a recent review paper by Rowley and Dawson [81], different model reduction techniques were reviewed for analyzing various fluid flow problems. As observed in previous studies, it is hard to select the dominant modes in unsteady inflow conditions using the DMD algorithm since we are unsure whether to prioritize modes' energy, frequency, or growth rate. Dynamic mode decomposition can yield spatial modes based on their frequency values, making it a convenient technique for investigating systems involving multiple frequency scales, as in the present study.

Recently, DMD algorithms have been implemented successfully to identify coherent structures and stability parameters in many pulsating flow conditions. In the work of Jang et al. [82], coherent flow features evidenced in the oscillatory flow around a cylinder are identified using the DMD algorithm. The algorithm determines the forcing frequency of oscillatory flow as the primary wave frequency, taking the amplitude criterion. Liu et al. [83] identified the coherent flow structures in cloud cavitating flow around the hydrofoil using the DMD algorithm. The energy of each mode is calculated using the Frobenius norm and sorted. Compared with other Reduced Order Models (POD), the DMD algorithm identifies the flow features and the underlying frequency of flow formations. A recent review by Taira et al. [84] depicts a detailed picture of different modal analysis techniques applied to different fluid flow scenarios.

The DMD algorithm starts by arranging state vectors from simulation data snapshots column-wise into two snapshot matrices, $\mathbf{U}_1$ and $\mathbf{U}_2$, with two consecutive time intervals ($\Delta\tau$). DMD analysis identifies a best-fit linear operator $\mathbf{A}$ that relates matrix $\mathbf{U}_1$ with matrix $\mathbf{U}_2$: DMD uses regression of data onto locally linear dynamics $\mathbf{x}_{k+1} = \mathbf{A}\mathbf{x}_k$, where A is chosen to minimize $||\mathbf{x}_{k+1} - \mathbf{A}\mathbf{x}_k||_2$ over k=1,2,3,..., N-1. Snapshot data is arranged in matrix format as:

$$\mathbf{U}_1 = [U^1, U^2, U^3, U^4 ... U^{N-1}] = \begin{bmatrix} u_1^1 & u_1^2 & ... & u_1^{N-1} \\ u_2^1 & u_2^2 & ... & u_2^{N-1} \\ \vdots & \vdots & \vdots & \vdots \\ u_M^1 & u_M^2 & ... & u_M^{N-1} \end{bmatrix},$$

$$\mathbf{U}_2 = \mathbf{A}\mathbf{U}_1. \tag{2.10}$$

By taking the Singular Value Decomposition (SVD) of the snapshot matrix ($\mathbf{U}_1$), we obtain left and right eigenvectors ($\mathbf{S}$ and $\mathbf{D}$, respectively), along with the eigenvalue (Λ).

$$\mathbf{U} \approx \mathbf{S}\Lambda\mathbf{D}. \tag{2.11}$$

In order to build a best-fit linear operator correlating both matrices, we take the pseudo-inverse of $\mathbf{U}_1$ (by taking the conjugate transpose of SVD vectors ($\mathbf{S}^*, \mathbf{D}^*$) together with $\mathbf{U}_2$ as follows:

$$A = \mathbf{U}_2\mathbf{D}^*\Lambda^{-1}\mathbf{S}^*. \tag{2.12}$$

By eigendecomposition, the low-dimensional model is decomposed into eigenvector ($\mathbf{W}$) and eigenvalues(λ_D) by eigendecomposition. The temporal dynamics of the system can be identified from the eigenvalues using the following relations for growth rate and frequency:

$$\sigma_{DMD} = \frac{log\left(Re\left(\lambda_D\right)\right)}{2\pi\Delta\tau}, \tag{2.13}$$

$$f_{DMD} = \frac{log\left(Im\left(\lambda_D\right)\right)}{2\pi\Delta\tau}. \tag{2.14}$$

In order to obtain the DMD modes (Φ), the low dimensional model is reconstructed from its eigenvectors as follows:

$$\Phi = \mathbf{U}_2\mathbf{D}\Lambda^{-1}\mathbf{W}. \tag{2.15}$$

DNS simulation offers a series of data sets for identifying the stability of the vortical structures in the wake. Since the frequency characteristics through the spectra analysis are from the vertical velocity component oscillation, the DMD using the vertical velocity also determines the coherent flow structures associated with frequency peaks of spectra analysis. Three-dimensional disintegration of the vortex flow features developed in the current investigation is closely related to the evolution of the streamwise and spanwise vorticity development in the wake region. Therefore, the DMD analysis of the vorticity components is also carried out to identify the secondary instability characteristics.

2.6 Summary

The current chapter discusses the different computational methodologies adopted in the present thesis work for simulating a transient inflow over different body geometries. Numerical simulations are carried out using a highly parallelized open-source DNS code INCOMPACT3D, which utilizes a higher-order compact scheme for spatial discretization coupled with spectral methods for pressure field computation. Imposing a complex geometry in a Cartesian grid is addressed using an immersed boundary method without any body orientation concerns. The transient inflow boundary condition is imposed through analytical solutions for a trapezoidal pulse obtained by the mathematical approach proposed by Das and Arakeri [27].

Different methodologies were adopted to investigate and characterize the development of three-dimensional instabilities in the flow field. Through the analysis of velocity profiles, the inflectional nature of the streamwise velocity profiles is investigated through Rayleigh's instability criterion. Further, the computational approach of the DMD method employed to identify the underlying coherent flow structures and temporal characteristics is explained in detail.

Chapter 3

Bluff-body wake under a variable velocity inflow

3.1 Introduction

The wall-mounted bluff bodies kept in time-dependent boundary conditions can produce a fascinating gamut of flow structures. In such cases, the thickness of the boundary layer formed over the solid surface varies in both space and time, causing a high level of complexity in the path of vortical structures formed from the shear/boundary layer. Numerical simulation studies are extensively used to understand the development of the vortical flow field and the subsequent generation of secondary structures. However, most numerical studies on flow transition in transient inflow conditions are performed on academic geometries. Numerically predicting the transitional flows in complex geometries poses a significant challenge.

This chapter focuses on vortex development within the wake of a wall-attached bluff body under variable velocity inflow conditions. A computational domain and temporal parameters are selected in accordance with the experiments of Das et al. [1]. By varying the mean inflow velocity, the effect of Reynolds number $\left(Re_b = \frac{U_p b}{\nu}\right)$ is studied for a Reynolds number range $100 \leq Re_b \leq 2500$. The influence of temporal variation in the inflow pulse is further examined by altering the acceleration and deceleration parameters. The inflectional nature of the boundary layer is investigated through streamwise velocity profiles. Further, shear layer instability features are identified through the vertical velocity fluctuations and their frequency spectra. This chapter provides an overview of vortex flow features, their temporal characteristics, and the fundamental instability nature of vorticity development.

The chapter is organized into five different sections. The section 3.2 introduces the

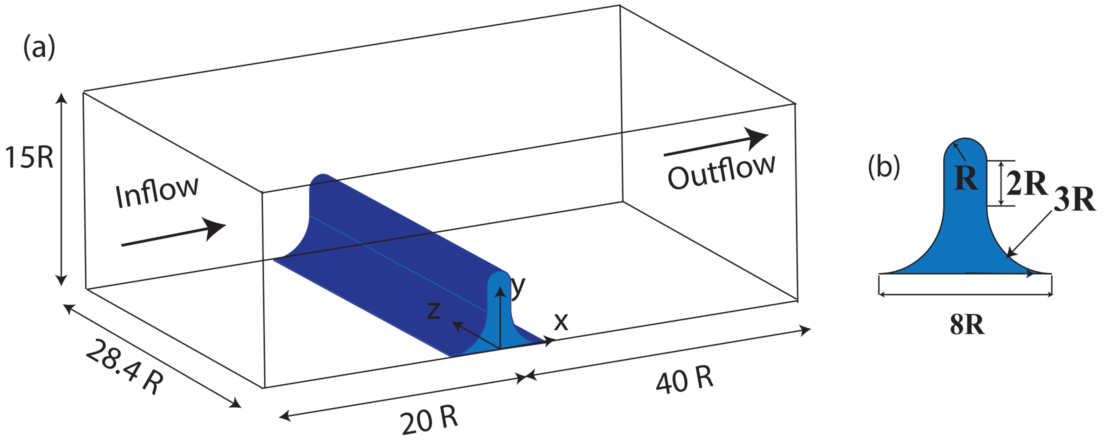

Figure 3.1: Computational domain and boundary conditions. (a) three-dimensional view; (b) details of the bluff body.

computational domain and non-dimensional parameters used for defining and explaining the flow evolution. In the third section (section 3.3), we briefly describe the initial observations and flow patterns that develop behind the bluff-body wake under different inflow velocities. The comparison of the flow evolution and three-dimensional disintegration under different non-dimensional numbers is provided in section 3.4. Finally, section 3.5 summarizes the discussions on flow evolution and the effect of the non-dimensional parameters.

3.2 Computational domain and simulation parameters

3.2.1 Computational Domain

Figure 3.1 shows the schematic diagram of the three-dimensional computational domain and boundary conditions used for the bluff body wake simulations. The complex-shaped bluff body used in the study of Das *et al.*[1] (figure 3.1) is modeled using the virtual or immersed boundary technique. The desired bluff body is formed by combining three circular arcs with a rectangular geometry. The maximum dimension of the bluff body is $8R \times 6R$, where R is the radius of the top circular geometry. No-slip condition on the top and bottom wall is assigned through the Dirichlet velocity condition. Free-slip condition is applied to the right and left boundaries. Analytical solutions obtained by considering a time-varying mean inflow in a 2D channel are enforced as the inlet condition at each time step (equations 2.8). Such practice is found to be an efficient way to reduce computational domain and time. At the outlet ($x = l_x$), the imposed exit velocity is deduced from the following equation:

$$\frac{\partial u}{\partial t}|_{\mathrm{X}=l_x} + U_c \frac{\partial u}{\partial \mathrm{X}}|_{\mathrm{X}=l_x} = 0. \tag{3.1}$$

Here, the mean velocity of the inflow profile during the pulse phase is taken as the advection velocity U_c.

3.2.2 Physical and numerical parameters

In order to quantify the effects due to variations in parameters, different non-dimensional quantities are defined. The instantaneous flow time t is non-dimensionalized by pulse period ($t^* = \frac{t}{t_2}$). Non-dimensionalized streamwise distance is defined by $x^* = \frac{X-0.2}{2R}$. Wall normal distance is non-dimensionalized by the body height ($y^* = \frac{Y}{6R}$). The following definitions are used to define the Reynolds number (Re_b), acceleration Reynolds number (Re_a), and deceleration Reynolds number (Re_d). A flow Reynolds number is defined based on the top circular geometry diameter (b), the mean inflow velocity during the constant velocity phase (U_p) and kinematic viscosity (ν).

$$Re_b = \frac{U_p b}{\nu}$$

Similarly, a standard non-dimensional number for studying flow dynamics in accelerating flows is the acceleration Reynolds number [85, 86]. Finaish *et al.* [86] successfully

Case	$U_p(m/s)$	Re_b	$t_0(s)$	$t_1(s)$	$t_2(s)$	Re_a	Re_d
BC1	0.0048	96	0.2	29.9	30.3	438	310
BC2	0.0359	718	7.5	8.92	11.92	196	450
BC3	0.0717	1434	1	4.33	5.33	756	756
BC4A	0.0956	1912	2.66	3.91	5.25	536	756
BC4B	0.0956	1912	1.33	3.25	4.58	756	756
BC4C	0.0956	1912	1.33	3.25	3.84	756	1138
BC4D	0.0956	1912	1.33	3.25	3.58	756	1522
BC4E	0.0956	1912	0.8	2.98	4.32	978	756
BC5	0.1195	2390	1.67	2.6	4.27	756	756

Table 3.1: Simulation parameters: U_p mean inflow velocity in constant inflow phase, t_0 end of the acceleration phase, t_1 end of constant velocity phase, and t_2 end of the deceleration phase. Reynolds numbers based on the mean inflow velocity, acceleration, and deceleration parameters are respectively represented by Re_b, Re_a, and Re_d.

analyzed the dependency between the vortex patterns development and the acceleration Reynolds number over an accelerating airfoil started from rest.

In an accelerating flow, an acceleration Reynolds number can be defined by considering piston velocity ($U_p(t)$).

$$Re_a = \frac{U_p(t)b}{\nu} = \frac{atb}{\nu};$$

where, the acceleration can be defined as: $a = \frac{U_p}{t_0}$ and $b = 2R$.

By taking a convective time scale t $= \sqrt{\frac{b}{a}}$;

$$Re_a = \sqrt{\frac{ab^3}{\nu^2}}.$$

The same procedure is followed in a decelerating flow to obtain

$$Re_d = \sqrt{\frac{db^3}{\nu^2}},$$

where, deceleration rate is obtained by: $d = \frac{U_p}{t_2 - t_1}$.

The non-dimensional vortex formation time [1] is represented by

$$t_v^* = \frac{1}{2}\frac{U_{t_v} t_v}{b}.$$

Here, t_v is the time when the vortex begins to form, and U_{t_v} is the mean inlet velocity at the t_v. The following non-dimensional time in terms of acceleration and deceleration parameters are defined using the relation:

$$\tau = t\sqrt{\frac{a}{b}},$$

$$t_d^* = \frac{t - t_1}{t_2 - t_1} = \frac{(t - t_1)d}{U_p}.$$

Numerical experiments were carried out for different flow parameters, as shown in table 3.1. The computational domain with dimensions $L_x \times L_y \times L_z = 60R \times 15R \times 28.4R$ is discretized using uniform grid points; dimensions are taken based on the experiments of Das *et al.*[1]. The grid independence was assessed by comparing the skin friction coefficient values at the midplane in a spanwise direction during the constant velocity phase for grids with $513 \times 129 \times 241$ (grid A), $1025 \times 257 \times 481$ (grid B), and $1501 \times 385 \times 721$

(grid C) elements. The percentage of deviation in skin friction coefficient between grids A and B was 10%, while it was below 1% for grids B and C. Figure 3.2 shows the streamwise variation of skin friction coefficient for grids A, B, and C. Results were reproduced

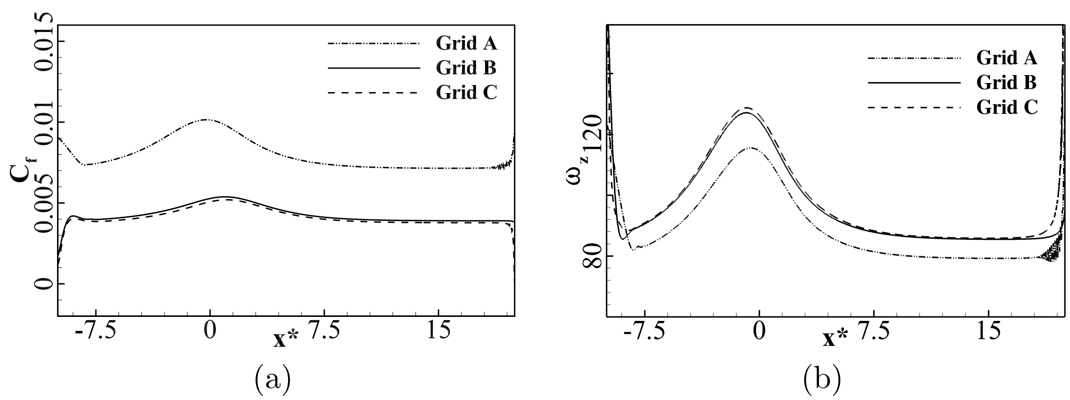

Figure 3.2: Grid independence analysis: (a) Variation of skin-friction coefficient (C_f), and (b) variation of spanwise vorticity (ω_z); with respect to non-dimensional streamwise direction $\left(x^* = \frac{X-0.2}{2R}\right)$ for different grid sizes.

with negligible difference between grid B and C, as evidenced in Figure 3.2. The Reynolds number employed in the grid independence study was the highest. Consequently, grid B is used for further simulations.

Time step dependency analysis was performed by using three different time steps of 10^{-3} s, 10^{-4} s, and 10^{-5} s. In terms of accuracy and computational economy, a time step of 10^{-4} s (CFL = 0.02) was found to be satisfactory. Therefore a time step of 10^{-4} s is used for all the cases. The numerical procedure is validated by comparing the vortex formation time (t_v) and separation angle (β) with the experimental results of Das *et al.*[1]. Here, the separation angle is defined as the angle between the separation point and the axis of symmetry of the bluff body (taken to the left of the axis of symmetry). The present simulations calculate the vortex formation time by plotting the streamlines at different flow instances. In contrast, Das *et al.*[1] used high-speed dye visualization techniques to measure the vortex formation time.

Figures 3.3(a, b) show the comparison of simulation results with experimental results of Das *et al.*[1]. The simulation result lies within a six percent deviation from experimental results, as shown in figures 3.3(a, b). The slight difference between numerical simulation and experiment could be because of the different methods used to evaluate the vortex formation time. Also, there could be minor differences in the inlet conditions between an

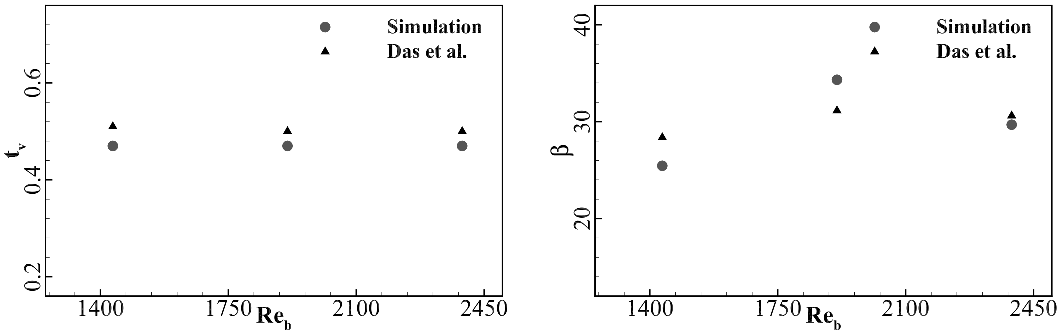

(a) (b)

Figure 3.3: Validation of numerical scheme. (a) Comparison of vortex formation time; (b) comparison of separation angle.

experiment and a simulation. It is not easy to maintain a perfect trapezoidal motion in an experiment, which causes inlet fluctuations in the water tunnel. In many studies, computational noise related to numerical methods has been discussed, especially in transitional and turbulent flows. These factors might account for the difference.

3.3 Two-dimensional flow structures

First, we present the numerical visualizations at different flow instances in $x - y$ planes for three Reynolds numbers (cases BC1, BC2, and BC5). The flow parameters are precisely the same as in the water tunnel experiments of Das *et al.*[1] (cases X, I, and XI in Das *et al.*[1]). Here, the evolution of flow structures from the bluff body at three different Reynolds numbers (Re_b = 96, 718, and 2390) are evidenced by instantaneous contour plot of spanwise vorticity (ω_z) in the center plane of spanwise direction ($z = 14.2R$) as shown in figures 3.4, 3.5 and 3.6. In our numerical visualization, at the low-Reynolds number (Re_b = 96), the recirculation region grows with the flow-time precisely like the experimental study, as shown in figure 3.4. Here, the formed structure is laminar and two-dimensional, with no sign of shear-layer instability. For similar flow conditions, the present simulations show good agreement (less than six percent deviation) with experimental observation.

At moderate Reynolds number ($Re_b = 718$), the initial formation of the primary vortex (marked as SL0 in figure 3.5) is similar to the low Reynolds number case (figure 3.5, $t^* = 0.28$ and 0.39). A pair of steady laminar separation bubbles formed over the leeward upper side of the bluff body vortices (marked as B1 and B2) is identifiable at $t^* \approx 0.55$. At

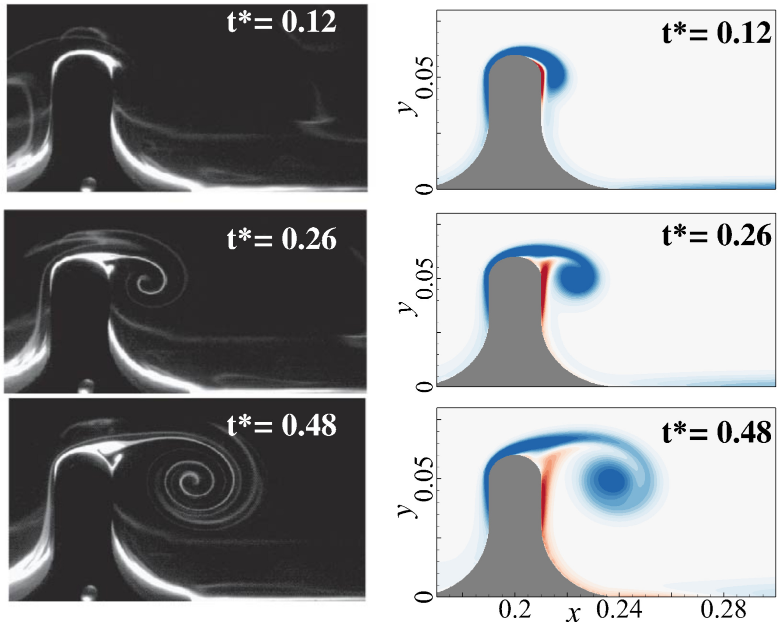

Figure 3.4: Flow evolution at low Reynolds number (case BC1). The experimental figure is reproduced with permission from Das *et al.*, [1] Journal of Fluids and Structures 40 (2013). Copyright 2013 Elsevier.

this Reynolds number, the flow shows shear-layer instability. The primary vortex oscillates at flow time $t^* \approx 0.68$. The origin of oscillations is near the steady separation bubbles. shear layer roll-up causes the formation of numerous small-scale vortices (marked as SL1 to SL4), which move around the primary vortex ($t^* = 0.92$). The newly formed shear-layer vortices eventually dominate the flow field. The sequence of vortices formed from the shear layer is analogous to that of a plane mixing layer ($t^* = 0.92$). Flow features near the top and bottom walls change significantly during the deceleration phase ($t^* = 0.92$ and 1). In addition, deceleration retards the motion of the vortex core ($SL0$). Deceleration creates an adverse pressure gradient and destabilizes the boundary layer. Local boundary layer separations are observed on the top and bottom walls (WT1 and WB1, respectively). The flow deceleration enhances the detachment of vortices from the near-wall vorticity layer (B2 and WB1). In later flow-time, these counter-vorticity regions shed into the core flow from the top and bottom wall (WB1 and WT1).

A similar sequence of events is evidenced at a relatively high Reynolds number ($Re_b = 2390$), with a higher shear layer shedding frequency, as depicted in figure 3.6. The shear layer roll-up and shedding of vortices (initiated from the steady separation bubbles B1 and B2) are observed at $t^* \approx 0.44$. At this Reynolds number, the shear layer breaks down quickly. A fascinating circular array of shear-layer vortices (SL1 to SL5) is observed along

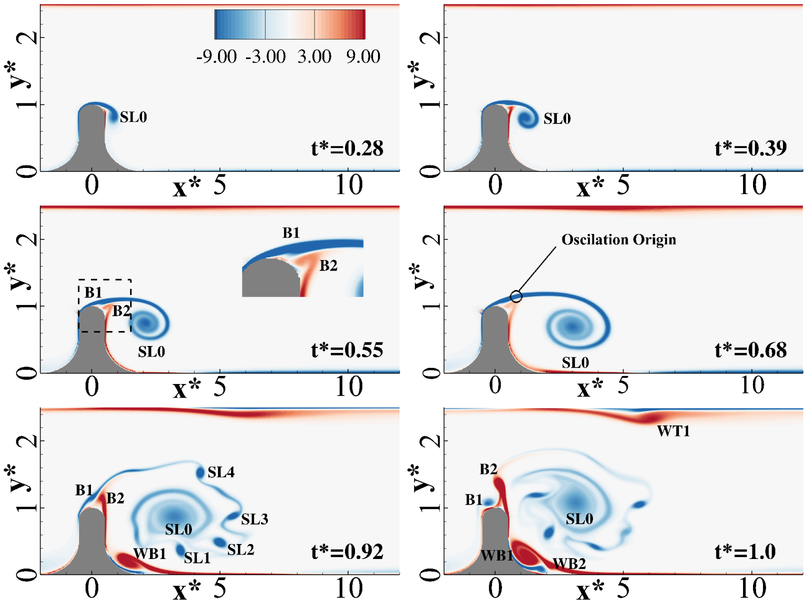

Figure 3.5: Instantaneous spanwise vorticity depicting the flow evolution in medium Reynolds number (case BC2).

the circumference of the primary large-scale vortex ($t^* = 0.60$). The transition to the decelerating phase is marked by a shift in the shedding pattern and the development of wall vortices ($t^* = 0.75$). With decaying streamwise velocity, momentum transfers into the boundary layer ($t^* = 0.90$), resulting in the amplification of positive vortices (WB1, WB2, WT1, WT2). In addition, towards the end of the pulse, these wall vortices move toward one another, causing pairing and the formation of three-dimensional structures ($t^* = 0.96, 1.01$). These structures expand and coalesce, forming the final stages of the vortex pulse. Multiple folding (mentioned as ‘fingers’) and the interconnections between vortices in the cylinder wake experiments of Gerrard [87] are also evident.

Figure 3.7 illustrates the velocity vector field plotted over the spanwise vorticity at different phases for case BC5. Numerous velocity vectors are skipped in the x and y directions from the obtained simulations for the clarity of the image. Rolled-up laminar separation bubbles (B1 and B2) formed over the bluff body and primary vortex are shown in figures 3.7(a) and 3.7(b). The vortices created by the shear-layer instability (SL1-SL6) do not show closed or spiraling streamline patterns, as shown in figures 3.7(b) and 3.7(c). Coherent structures formed during the decelerating phase near the top and bottom wall proximity are shown in figures 3.7(d) and 3.7(e), respectively. During this deceleration period, the magnitude of other components of velocity escalates abruptly (figures 3.7(d) and 3.7(e)). Continued shedding of the boundary layer vortices (WB1-WB3) from the bottom boundary

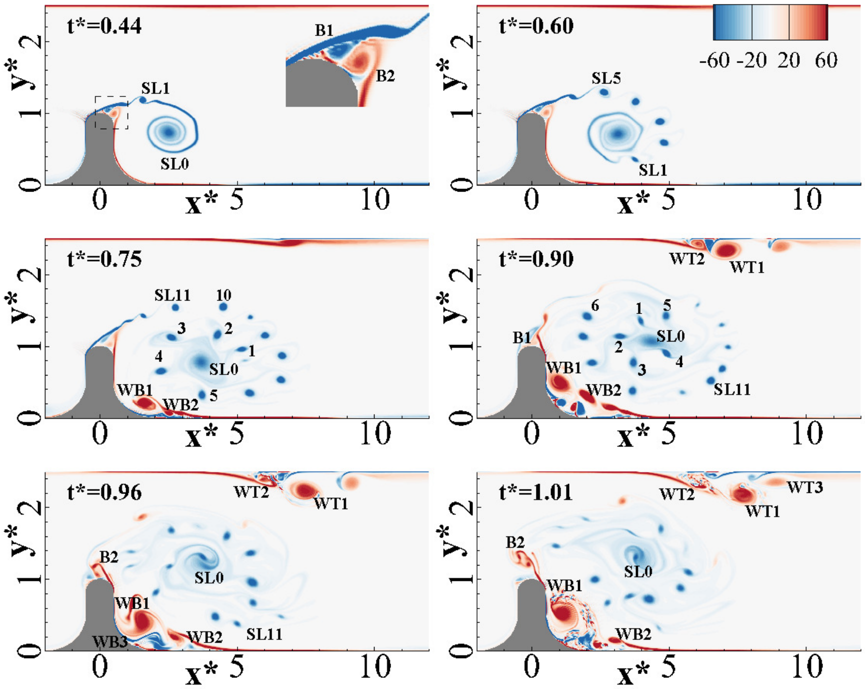

Figure 3.6: Instantaneous spanwise vorticity depicting the flow evolution in high Reynolds number (case BC5).

layer due to the shear layer vortex structures is evident.

3.4 Influence of non-dimensional numbers on flow evolution

Through the variation of the associated non-dimensional numbers, transient parameters' influence on flow evolution is systematically analyzed. This analysis provides insight into the effects of transient parameters on flow behavior and can aid in predicting the dynamics of the flow. We can determine the influence of the mean inflow velocity by varying the Reynolds number; a higher mean inflow velocity leads additional shear layer vortices to develop, resulting in a higher shear layer frequency. Consequently, this ultimately leads to an increase in vortex structures and, subsequently, the production of more turbulence. In the same way, acceleration and deceleration parameters have similar effects on the shear layer and three-dimensional integration. By examining the vertical velocity and momentum thickness variations, we can better understand the behavior of the flow field and the underlying physical processes involved. In the subsections that follow, we examine in detail the

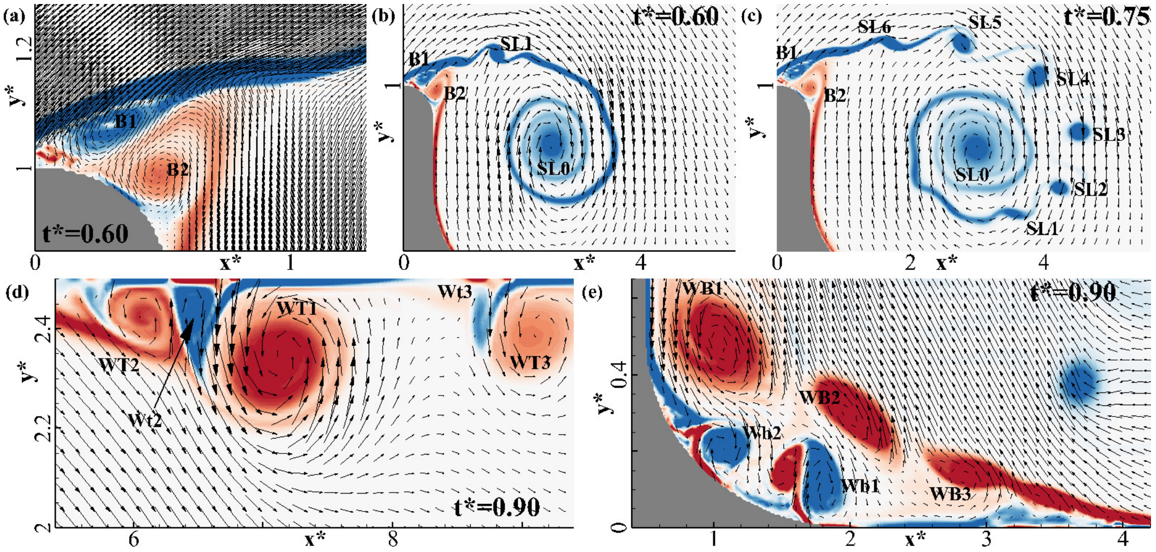

Figure 3.7: Detailed view of the coherent structures observed during different phases of the flow evolution. (a) separation bubble over the bluff body; (b) early stage of vortex shedding; (c) an instance of periodic vortex shedding; (d) top-wall boundary layer separation; (e) bottom-wall boundary layer separation.

effect of these non-dimensional numbers on the formation of flow patterns.

3.4.1 Effects of Reynolds number on flow evolution (cases BC3, BC4B and BC5)

The effects of Reynolds numbers on flow dynamics are systematically analyzed by keeping the acceleration and deceleration Reynolds numbers constant (BC3, BC4B, and BC5). Important flow parameters obtained from the simulation are tabulated in table 3.2. An evaluation of the non-dimensional vortex formation time and separation angle is conducted, and the results are found to agree well (within 10 percent) with those from experiments as shown in table 3.2.

Case	Re_b	t_v^*	$t_{v,exp}^*$	β	β_{exp}	t_{sl}	f_V	f_θ	$\frac{f_\theta \theta_{avg}}{U_p}$
BC3	1434	0.39596	0.46623	25.45	28.37	1.18	5.46	4.94	0.718
BC4B	1912	0.39696	0.44925	34.33	31.14	1.50	7.5	7.32	0.659
BC5	2390	0.39517	0.44723	29.69	30.61	1.82	10.00	10.20	0.469

Table 3.2: Quantitative comparison of parameters non-dimensional vortex formation time (t_v^*), and separation angle (β) with experimental results of Das *et al.* [1]. f_V and f_θ respectively represent vertical velocity and momentum thickness oscillation frequency.

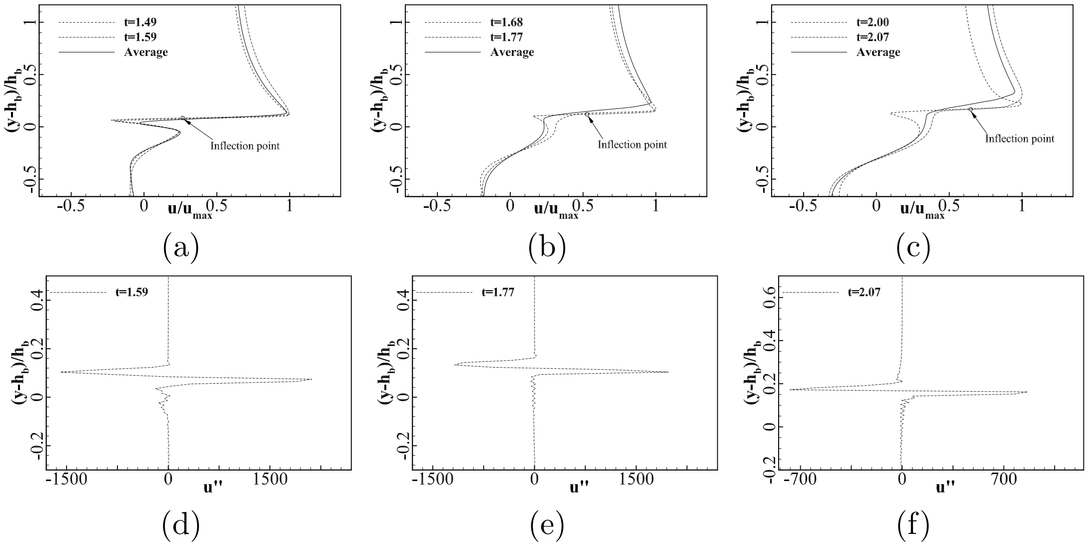

(a) (b) (c)

(d) (e) (f)

Figure 3.8: Streamwise velocity profiles for different cases ($x^* = 2.3047$). (a) case BC3; (b) case BC4B; (c) case BC5. Second derivative profiles of velocity profile (d) case BC3; (e) case BC4B; (f) case BC5.

The inflectional nature of velocity profiles causing the instability are compared at locations near the bluff body and are plotted in figure 3.8. The velocity profiles observed downstream of the bluff body are the superposition of the confluent mixing layer (wake and shear layer) and boundary layer. Inflectional streamwise velocity profiles are observed in all the cases (figure 3.8(a), 3.8(b), and 3.8(c)). Shear-layer instability is originated in the vicinity of the inflection point on the velocity profile. This two-dimensional instability results in an intermittent formation of a two-dimensional circular array of small vortices (SL1, SL2, ...etc.). The inflectional nature of flow instability can be further explained using the second derivative of the velocity profile (equation 2.9). Figures 3.8 (d), (e), and (f) show the second derivative of the non-dimensional velocity profiles for cases BC3, BC4B, and BC5, respectively. Here, figures 3.8 (d), (e), and (f) show inflection points for all the cases, which are marked with circles in figures 3.8 (a), (b), and (c). These inflected points are inviscidly unstable and prone to flow instability. As seen from the two-dimensional contour graphs of the instantaneous spanwise vorticity (figures 3.5 and 3.6), the flow oscillations originate at these inflection points. Hence, flow instability appears to develop at these inflection points in velocity profiles.

Some typical time series of vertical velocity are plotted for three Reynolds number cases to probe the nature of the flow unsteadiness, as shown in figure 3.9(a). Here, the

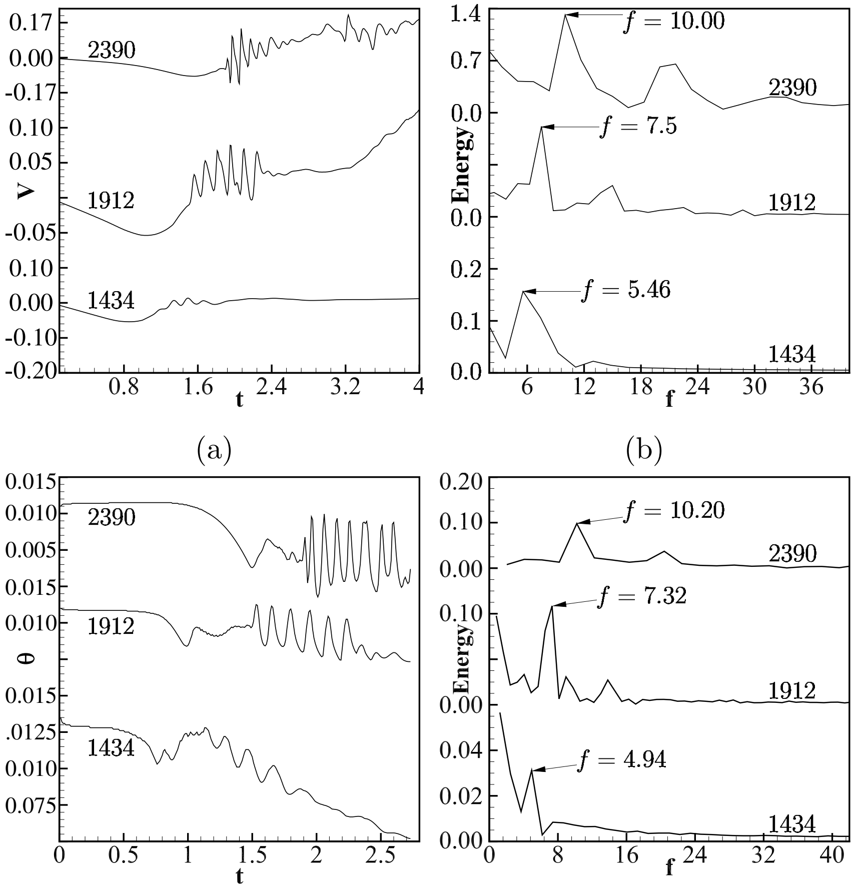

(a) (b)

(c) (d)

Figure 3.9: Temporal variation of velocity, momentum thickness, and corresponding frequency spectra. (*a*) wall-normal velocity; (*b*) frequency spectra of wall-normal velocity; (*c*) temporal variation of momentum thickness; (*d*) frequency spectra of momentum thickness.

measurement point is near the origin of shear layer oscillations. The shear-layer shedding process can be seen from the time series data of vertical velocity. The shear-layer instability vortices/waves have a definite frequency, especially at a high Reynolds number. The peak frequency of velocity fluctuation is determined using spectral analysis (figure 3.9(b)). Further time series analysis is made by changing the location of the measurement points. The newly selected measurement positions are at downstream locations but inside the shear layer shedding regions. Similar time series sequences are obtained in the new measurement locations. The local momentum thickness of the shear layer is calculated by removing the data near the top and bottom wall using the below expression.

$$\theta = \int_{h_1}^{h_2} \frac{u}{U_{max}} \left(1 - \frac{u}{U_{max}}\right) dy.$$

Instantaneous momentum thickness oscillates at a frequency (f_θ) that is nearly equal to the frequency obtained from the time-series data of the vertical velocity (f_v), as shown in figure 3.9(d). The non-dimensionalized frequency $\left(\frac{f_\theta \theta_{avg}}{U_p}\right)$ based on average momentum thickness is tabulated in table 3.2. However, here the values do not remain constant.

3.4.2 Effects of acceleration Reynolds number on flow evolution (cases BC4A, BC4B and BC4E)

The effects of acceleration Reynolds number on flow feature are analyzed for three cases with varying Re_a by keeping Re_b and Re_d constant (cases BC4A, BC4B, and BC4E). The development of the vortex core point (x_c) trajectory for the primary vortex is traced for all the Re_a cases. The core is identified by probing the location with instantaneous minimum local pressure in a two-dimensional $x - y$ plane. Here the low-pressure criterion effectively captures the core of the primary vortex structure. The location of the low-pressure point for three acceleration Reynolds numbers at various flow times is calculated (as marked in figure 3.11). The following non-dimensional parameters are defined to track the core trajectory:

$$X_c = \frac{x_c - 0.2}{8R}$$

Figure 3.10 shows the variation of non dimensionalized vortex core position (X_c) against the non-dimensionalized time scale ($\tau = t\sqrt{\frac{a}{b}}$). At early flow times ($\tau < 3$), a reasonable collapse of the location of the core of the primary eddy is obtained with the new scaling, as shown in figure 3.10. This regime corresponds to the time of collapse ($\tau < 3$), is two-dimensional, and is unaffected by shear layer oscillations. With the increase in flow time ($\tau > 3$), the core trajectory significantly departs from each other. Furthermore, it appears that the shear-layer instabilities and three-dimensional structures cause this departure, and they are analyzed in detail below.

Flow evolution for three different acceleration Reynolds cases at the same non-dimensional flow time (τ) is shown in figure 3.11. At the early time (τ = 2.75), the primary vortex core lies precisely at the same point for all three cases. For the case of the lowest acceleration Reynolds number $Re_a = 536$, as shown in figure 3.11(a1), the flow does not generate shear-layer vortices. At this flow time, for medium and high acceleration Reynolds number cases

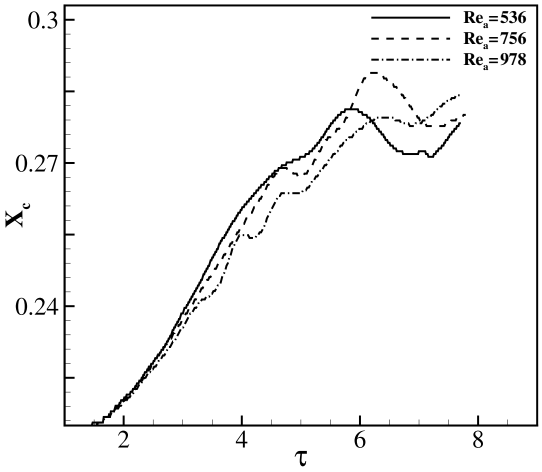

Figure 3.10: Variation of vortex center position for cases BC4A, BC4B, and BC4E.

Case	Re_a	$t_v(s)$	t_v^*	β	$t_{sl}(s)$	f_θ	f_V	σ_{max}	$f_{\sigma_{max}}$
BC4A	536	0.66	0.39138	22.03	2.86	8.07	8.57	0.0380	8.26
BC4B	756	0.47	0.39696	34.33	1.50	7.32	7.5	0.0714	7.33
BC4E	978	0.37	0.40899	29.69	0.93	6.25	7.04	0.1047	6.93

Table 3.3: Effects of acceleration Reynolds number on flow features

($Re_a = 756$ and $Re_a = 978$), the shear-layer instability triggers a series of small-scale vortices, as shown in figures 3.11(b1) and 3.11(c1). The local separation bubble on the top wall is formed further upstream for higher Re_a cases (figures 3.11 (a2), (b2), and (c2)). Another important feature worth mentioning is that the shear-layer instability features are observed earliest in the high acceleration case, while three-dimensional instability features are observed in the low acceleration case. The flow structures near the walls are relatively complex at low acceleration Reynolds number cases (figures 3.11 (a3), (b3), and (c3)). However, small-scale eddy formation near the bottom and top walls under the influence of the local adverse pressure gradient is observed for all cases.

A quantitative comparison of vortex formation time, non-dimensionalized vortex formation time, and separation angle is made in table 3.3. Here, the non-dimensional vortex formation time (t_v^*) is nearly constant. By using the boundary layer parameters, a universal time scale of separation independent of Reynolds number and acceleration Reynolds number is obtained. The two-dimensional shedding frequencies are obtained from spectral analysis of vertical velocity. As discussed in the preceding section, the instantaneous momentum thickness oscillates at a frequency that is nearly equal to the frequency obtained

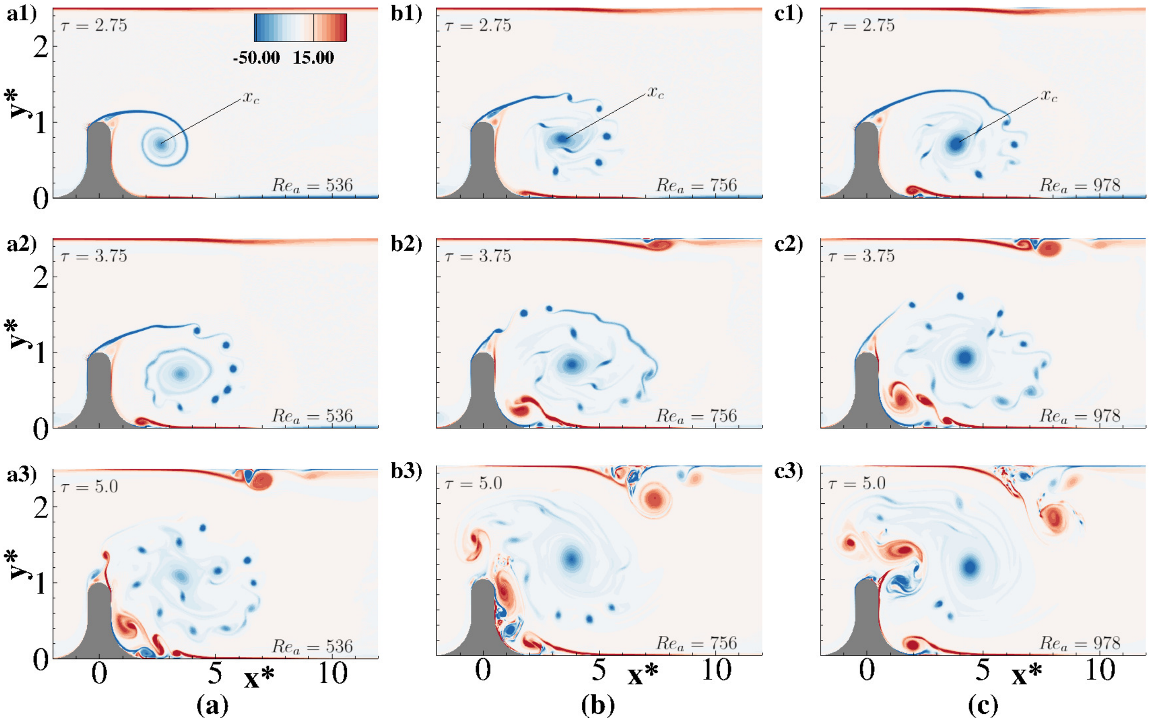

Figure 3.11: Flow evolution for different Re_a cases (a) BC4A, (b) BC4B and (c) BC4E.

from the time-series data of the vertical velocity. The values of peak frequency so estimated are listed in table 3.3. Here, the peak shear layer frequency decreases with an increase in acceleration Reynolds number.

3.4.3 Effects of deceleration Reynolds number on flow evolution (cases BC4B, BC4C and BC4D)

An analysis of the effects of the deceleration Reynolds number on flow evolution is performed using two different approaches. In both approaches, significant differences in flow characteristics were observed, indicating that the deceleration Reynolds number can greatly influence flow dynamics. First, we examine the effects of deceleration on flow characteristics. In the second, we study the mechanism of streamwise vorticity formation, which leads to three-dimensional oscillations and transitions. This two-pronged approach allows a comprehensive analysis of the intertwined process of vortex structure disintegration. Although the flow features formed during the deceleration period vary depending on the deceleration parameters, the generation of the three-dimensional oscillation remains constant in all cases.

3.4.3.1 Evolution of flow structures during the deceleration phase

To illustrate the effects of deceleration on flow features, three cases are analyzed with varying Re_d by keeping Re_b and Re_a as constants. The effects of deceleration are analyzed by plotting instantaneous vorticity at different non-dimensionalized flow times $\left(t_d^* = \frac{t-t_1}{t_2-t_1}\right)$, as shown in figure 3.12. Figure 3.12 shows vorticity data at the starting point ($t_d^* = 0$), quarter one ($t_d^* = 0.25$), quarter two ($t_d^* = 0.5$), and at the end of the deceleration phase ($t_d^* = 1$).

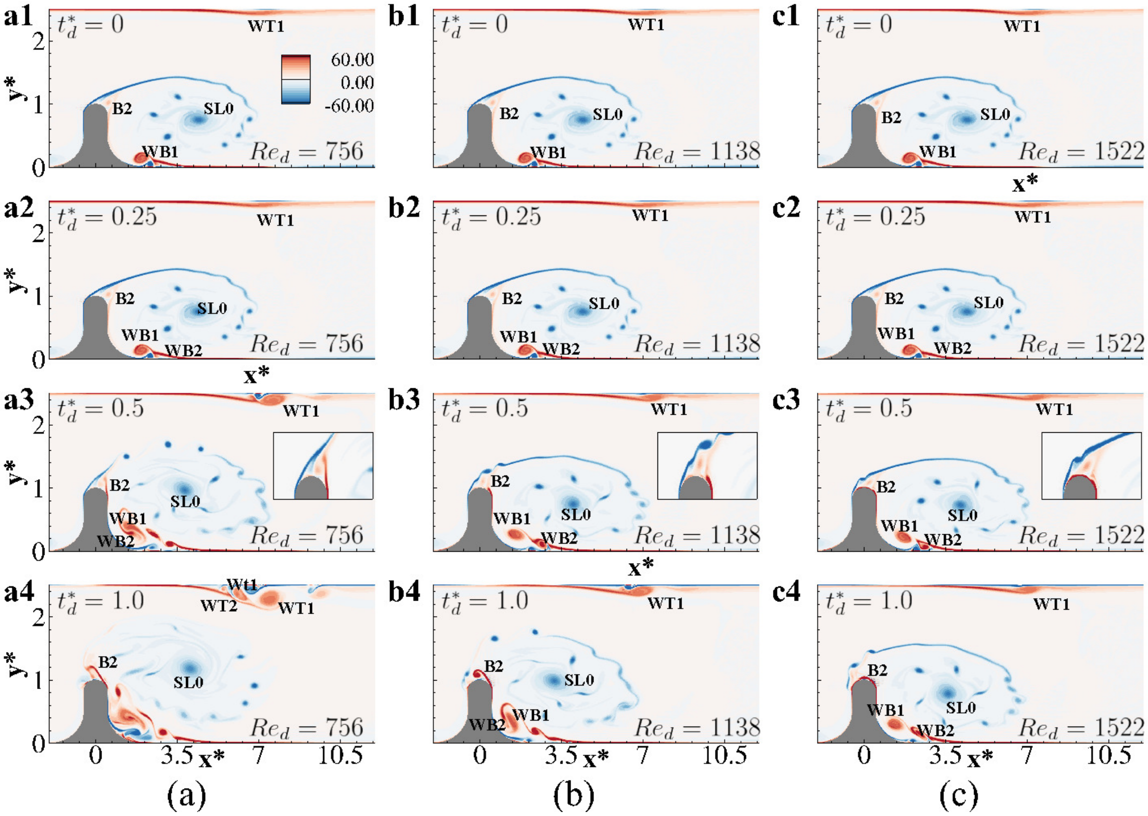

(a) (b) (c)

Figure 3.12: Evolution of spanwise vorticity during different deceleration phases. (a) BC4B, (b) BC4C, and (c) BC4D.

The flow dynamics of the primary vortex ($SL0$) and shear-layer vortices are nearly similar at $t_d^* = 0.25$ for all the cases. However, the deceleration Reynolds number effects are seen in the dynamics of wall vortices. In the case of smooth deceleration (at low Re_d), the detachment of vortices from the wall ($B2$ and $WT1$) is observed at an early non-dimensionalized deceleration period (t_d^* = 0.5) as shown in figure 3.12(a3). Higher shedding characteristics of the low deceleration case owe to the momentum transfer to the boundary layer due to shear layer vortex interactions. Further, the ejected boundary layer vortices move closer to each other, leading to merging phenomena as depicted in figure 3.12(a3). Concomitantly, the evolution of separation bubble vortices also alters with the change in deceleration parameters. A close-up view of the detachment of the separation bubble is shown in the subplot in (figure 3.12(a3), 3.12(b3), and 3.12(c3)). As evidenced in these figures, the decrease in the deceleration moves the separation point downstream by reducing the separation angle.

As the primary vortex decelerates, the separated secondary structures (WT1) in the top surface boundary layer develop rapidly, and rapid boundary layer growth occurs near the secondary eddy (Wt1). Under the influence of the primary vortex structure, further small-scale eddy structures soon develop near the top and bottom walls due to the adverse pressure gradient induced by the vortex. At the end of the deceleration period ($t_d^* = 1$, figures 3.12(a4), 3.12(b4) and 3.12(c4)), an eruption of the viscous flow near the top wall (near WT1) are observed for low Re_d case (figure 3.12(a4)). For medium and high Re_d cases, the deceleration causes an increase in bubble volume ($WT1$ and $WB1$), but at the end of the deceleration period, the vortical region would not wholly separate from the surface (figure 3.12(b4) and 3.12(c4)) as in the low Re_d case.

3.5 Summary

The current chapter focuses on vortex dynamics in a bluff body wake under a variable velocity inflow. The flow employed to study the dynamics was a channel with a wall-attached bluff body kept in a trapezoidal pulse of mean velocity inflow. This configuration is ideal for studying wake dynamics in the wake of a relatively complex bluff body under a trapezoidal pulse, enabling a comprehensive analysis of the effects of acceleration and deceleration separately.

A systematic study on effects due to change in Reynolds number, acceleration Reynolds number, and deceleration Reynolds numbers on flow dynamics were carried out. Though flow evolution has a strong dependence on the flow Reynolds number, the unsteadiness has its effects on the flow-feature formation. The primary inflectional instability nature is examined through Rayleigh inflection point criteria for the streamwise velocity profiles. In addition, the secondary instability features are analyzed through the spanwise vorticity contoured two-dimensional snapshots, and the associated temporal characteristics are extracted from spectral analysis of probe data.

The results obtained from the DNS simulation suggest the following picture for the development of wakes. Flow features such as laminar separation bubbles, shear layer oscillations, and associated rollups are observed during the constant acceleration or constant velocity phase. Subsequently, due to shear-layer instabilities, a two-dimensional circular array of spanwise vortex tubes is developed from the primary vortex. During the deceleration phase, the evolving spanwise vortex rolls and induced near-wall circulating eddies to encounter axial stretching, and flow transitioned from a two-dimensional to a three-dimensional state. Vortex merging and strongly localized eruptions near the top and bottom walls are observed.

The effect of the Reynolds number on shear layer frequency was analyzed using momentum thickness of inflectional velocity profiles, velocity, and momentum thickness spectra. A non-dimensionalized timescale (τ) tracks the primary vortex core in varying acceleration cases. The low acceleration Reynolds number case showed early signs of 2D-3D transition in the non-dimensional time frame. Variations in deceleration parameters affect the formation of wall vortices, resulting in the development of three-dimensional structures. Qualitative and quantitative comparison of the flow evolution in different deceleration cases strongly supports this observation.

Chapter 4

Three-dimensional aspects of coherent flow structures in bluff body wake

4.1 Introduction

A detailed discussion of the vortex flow dynamics and the shedding characteristics were provided in the previous chapter. Spanwise oscillations and further disintegration processes are strongly influenced by the nature of the vortices developed and their mutual induction/interaction. Bluff body wake constitutes a higher number of the co-rotating vortex structures, which interact with each other, resulting in the merging and further transition. Similar to other wake vortex studies, the instabilities arising in a bluff body wake can be classified into instability development in core and braid regions.

The current chapter aims to present a comprehensive analysis of underlying three-dimensional coherent flow features in flow evolution and their stability characteristics using a reduced-order modeling approach. Dynamic mode decomposition is employed for decomposing the coherent structures and flow patterns, whose dynamics provide a more compact method for describing the flow process. In addition, the temporal characteristics of the DMD modes identified are compared with the frequency spectra obtained from probe analysis. Furthermore, the effect of the acceleration and deceleration parameters on flow development is delineated through coherent features and their associated frequency characteristics. Also, in this investigation, the streamwise vorticity generation equation is employed to model the formation of streamwise vorticity during the dead inflow phase.

The three-dimensional aspects of flow features in the wake of bluff body are detailed in this chapter. In section 4.2, a comparison of three-dimensional simulations with two-dimensional simulation results shows the vortex disintegration during the zero mean inflow phase captured in three-dimensional simulations. Section 4.3 discusses the spatial features of the three-dimensional flow structures that are identified using the λ_2 method. The temporal nature of coherent flow features is investigated using DMD analysis, as outlined in section 4.4. By analyzing the evolution of the components in the streamwise vorticity generation equation, the three-dimensional transition mechanism is further explained in section 4.5. In section 4.6, we summarize the observations on the three-dimensional flow features and the associated vorticity generation mechanism in the bluff-body wake.

4.2 Deviation in three-dimensional simulations

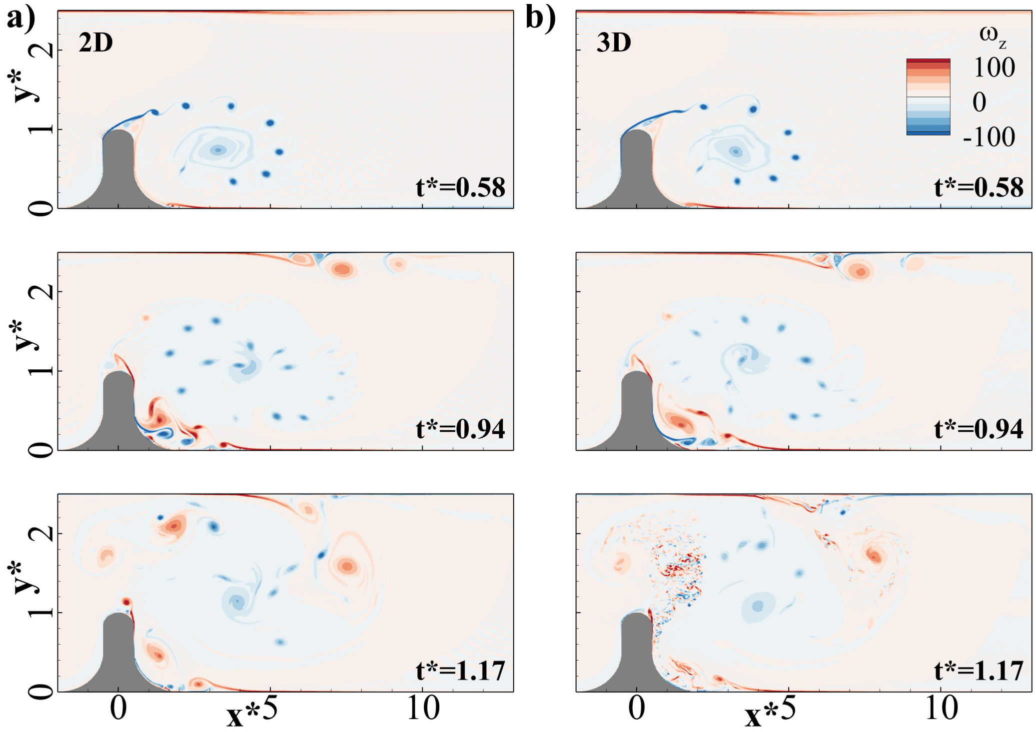

Figure 4.1: Comparison of three-dimensional and two-dimensional simulations for high Reynolds number (case BC5). (a) two-dimensional simulation; (b) three-dimensional simulation.

Initially, a comparison of simulations in two and three dimensions is provided to better understand the nature of the shear-layer instability mechanism. Figure 4.1 shows the flow evolution of two-dimensional and three-dimensional simulations for high Reynolds number (Re_b = 2390). The flow features are analogous in two-dimensional and three-dimensional simulations during acceleration and constant-velocity phases ($t^* = 0.58$ and 0.94). Here, two-dimensional perturbations are inherently unstable compared to three-dimensional perturbations during the initial phase. Due to the two-dimensional nature of shear-layer instability, the amplification and shedding of the shear-layer vortices are evidenced in the two-dimensional simulation, similar to three-dimensional simulations. With increasing flow time, three-dimensional effects appear, which could be due to the secondary instability of the separated shear layer, as seen in many steady flow transition conditions [56, 88]. For case BC5, the two-dimensional simulation results reasonably agree with the experiment results up to the deceleration phase.

A flow transition from a two-dimensional to a three-dimensional state can initially be observed near the wall proximity. During the decelerating and zero mean-velocity phases, three-dimensional flow characteristics such as axial stretching, tilting of vortices, and subsequent instabilities in spanwise directions are dominant. Positive vortices are formed from the body, which interacts with the core flow and eventually breaks down. Due to this inherent limitation, two-dimensional simulations do not capture the final disintegration of the vortices. Drastic differences in flow dynamics occur during the zero mean-velocity phases ($t^* = 1.17$).

4.3 Three-dimensional flow structures

We further examine the instability's three-dimensional nature using the λ_2 method [89] in the three-dimensional flow field. This method is rigorously applied to accurately depict the topology of vortex cores in diverse classes of flows, including the wake patterns behind bluff bodies, transitional, and turbulent flows.[13] For DNS data, λ_2 has been found to assess the size of the vortex core and the number of small scales. In this method, coherent vortex structures in the flow field using the second-largest eigenvalue of the symmetric tensor are created from the symmetric and anti-symmetric components of the velocity gradient tensor. Detailed analysis of this method is available in the work of Jeong and Hussain. [89]

Isometric views of the vortices identified using the λ_2 method at different flow instances for medium Reynolds number (case BC2) are shown in figure 4.2. The isosurfaces are colored according to spanwise (figures 4.2(a) and 4.2(b)) and streamwise vorticity (ω_x) magnitude (figures 4.2(c) and 4.2(d)) to show the orientation of the three-dimensional structures. At $t^* = 0.88$, the flow field mainly consists of two-dimensional shear-layer structures (figures 4.2(a) and 4.2(c)). The value of streamwise vorticity is minimal at this flow instant. The values are slightly higher near the side boundaries. The amplification of the streamwise vorticity (ω_x) components (figures 4.2(b) and 4.2(d)) indicate the flow transition from a two-dimensional to a three-dimensional state. Spanwise modulations of streamwise vor-

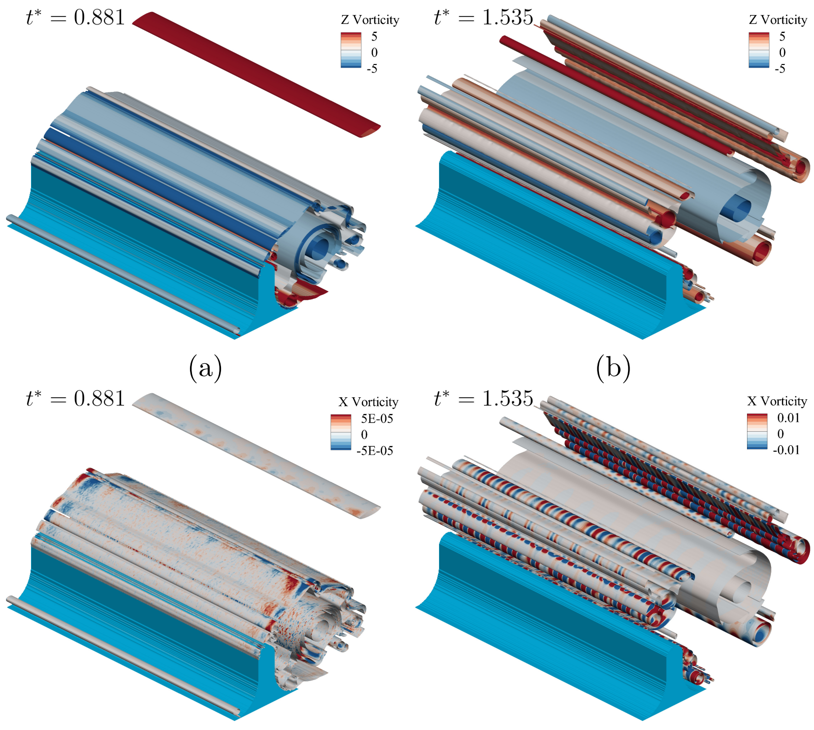

(c) (d)

Figure 4.2: Three-dimensional structures were identified using λ_2 criteria, colored by vorticity, for medium Reynolds number (case BC2). (a) ω_z contour at $t^* = 0.881$; (b) ω_z contour at $t^* = 1.535$; (c) ω_x contour at $t^* = 0.881$; (d) ω_x contour at $t^* = 1.535$.

ticity and the tendency to generate three-dimensional structures are evident at later flow instances. The shear-layer eddies from two-dimensional instabilities are deformed by three-dimensional instabilities, as shown in figures 4.2(b) and 4.2(d). Alternate negative and positive streamwise vorticity regions are observed in the spanwise direction (figure 4.2(d)). Since the dynamics alter in time, conditions conducive to three-dimensional instability are generally formed at the end of the decelerating phase. Here, the birth of streamwise vorticity is due to the progressive development of the spanwise velocity component as the flow time increases. Three-dimensional modulations are not evident in the immense core primary vortex (SL0).

Iso surfaces of λ_2 structures colored by spanwise vorticity at different flow instances for high Reynolds number (case BC5) are shown in figure 4.3. During the deceleration phase, the flow changes from a two-dimensional state to a three-dimensional one (figures 4.3 (a),(b),(c) and (d)). Coherent three-dimensional modes are observed in the simulations, and

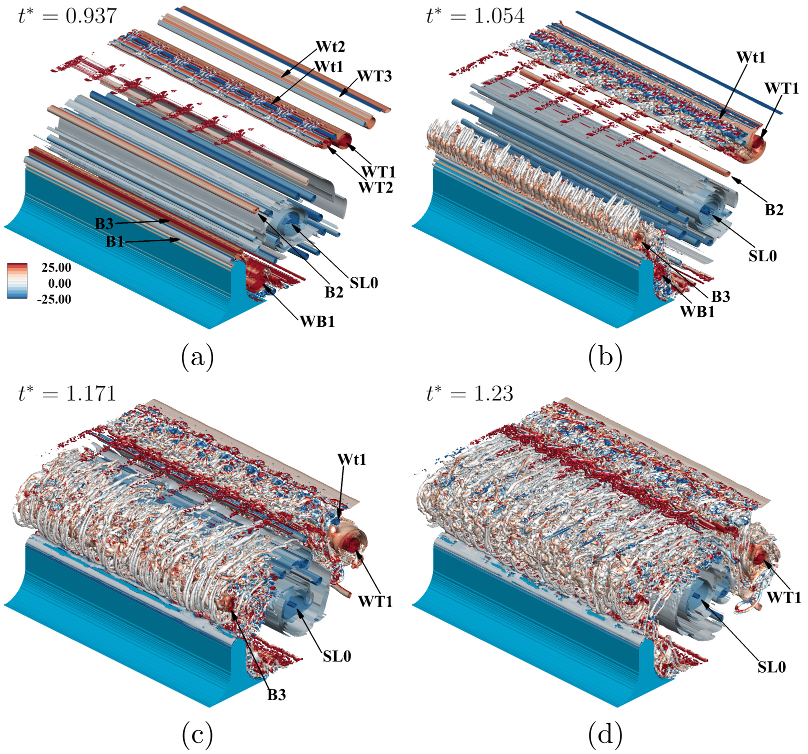

Figure 4.3: Three-dimensional structures were identified using λ_2 criteria, colored by spanwise vorticity at different flow instances, for high Reynolds number (case BC5). (a)$t^* = 0.937$, (b) $t^* = 1.054$; (c) $t^* = 1.171$; (d) $t^* = 1.23$.

the structures are similar to the other wake-transition studies[13, 46]. The spanwise vortex rolls evolved by shear-layer instability, and near-wall vortices encounter axial stretching. Dominating three-dimensional flow instabilities of the vortex sheets are realized for near-wall structures. Clear distinctions in shape and spanwise wavelength are observed between the bottom-wall and top-wall formed flow structures. Fragmented streamwise structures and small-scale eddies generated from the spanwise vortex rolls are evident at later flow time ($t^* = 1.23$). The origin of small-scale structures from the shear rolls is observed in the zero mean-velocity phases. The topology of streamwise vorticity is depicted in Figures 4.4 (a)-(d). Fundamentally unstable characteristics of strained vortex sheets cause the formation of streamwise vorticity. The wavelength of the streamwise vortices (the spanwise distance between adjacent streamwise vortex pairs) is measured for all the spanwise rolls. Long-wavelength, tongue-like structures are observed near the top wall. Short-wavelength, rib-like structures, characteristic of the mode B instability in the cylinder wake study, are observed near the bluff body, as shown in figures 4.5(a). For mode B structures in the cylin-

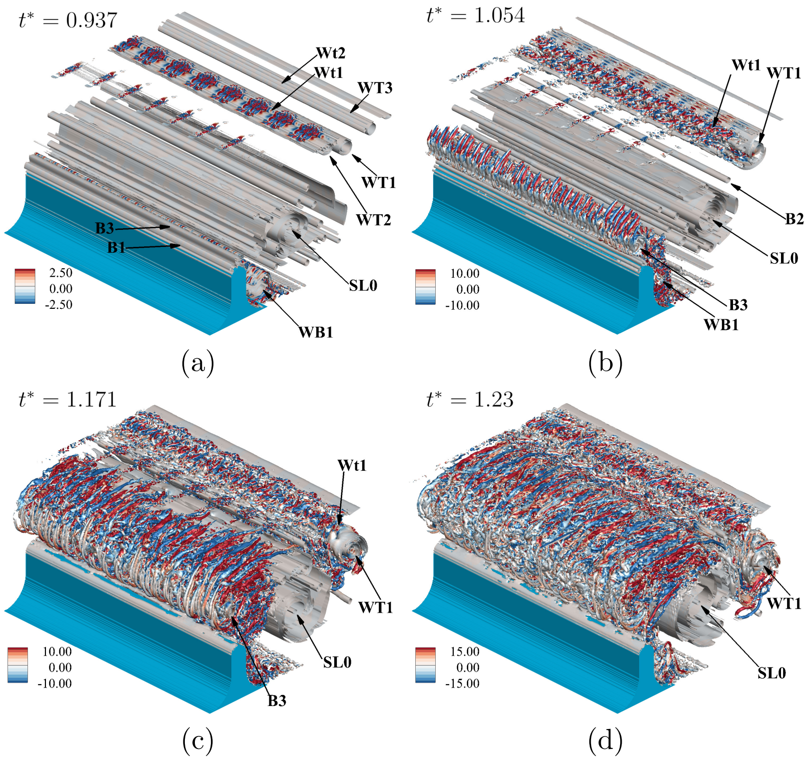

Figure 4.4: Three-dimensional structures were identified using λ_2 criteria, colored by spanwise vorticity at different flow instances, for high Reynolds number (case BC5). (a) $t^* = 0.937$; (b) $t^* = 1.054$; (c) $t^* = 1.171$; (d) $t^* = 1.23$.

der wake, a spanwise wavelength of $\lambda_z \approx \frac{40}{\sqrt{Re}}R$ was proposed by Mansy *et al.*[90]. The spanwise wavelength for mode B matches the value obtained from cylinder wake studies. Signatures of modes A and B are evident in the top view contours of spanwise vorticity figures 4.5 (a) and (b). The process of a three-dimensional breakdown associated with streamwise vorticity is depicted in figure 4.5 (b). The difference in spanwise wavelength is evident in the top views. Streamwise vortices are advected from the bottom wall and generated from the top wall due to the boundary layer separations dominating the flow field.

In steady flow cases, similar modes are observed, indicative of secondary instability. Hence in the present case, two and three-dimensional secondary perturbations may lead to a three-dimensional flow transition. A combination of more than one secondary instability mechanism is present during the later flow time, as indicated by Mode A and Mode B structures. The spanwise deformation of the separation bubble observed near the top wall is caused by the elliptic instability of vortex cores, which results in a wavelength of the

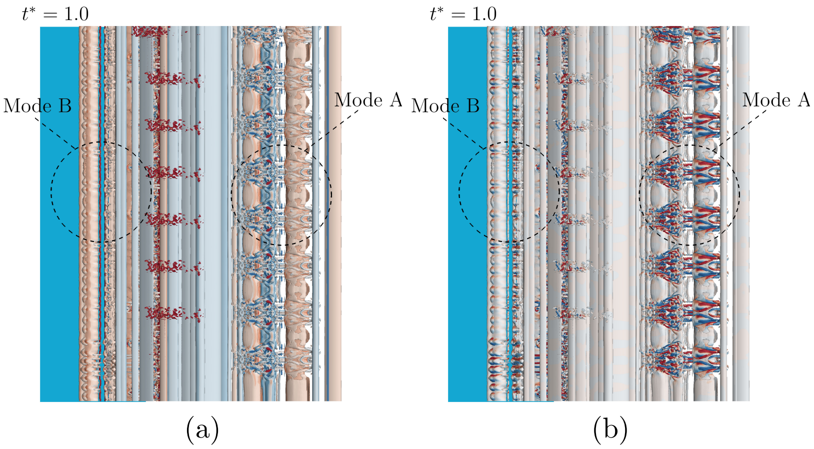

(a)

(b)

Figure 4.5: Three-dimensional structures were identified using λ_2 criteria, colored by spanwise vorticity at different flow instances, for high Reynolds number (case BC5). Top-view colored by ω_z at $t^* = 1$; (d) top-view colored by ω_x at $t^* = 1$.

order of the vortex size (mode A). This mode (mode A) occurs when three-dimensional disturbances are amplified in regions of two-dimensional elliptical streamlines of counter-rotating vortex pairs.[12] The flow structures that occur near the bottom wall are also characterized by three-dimensionality that potentially arises due to the instability of flow arising between two consecutive vortices. Short-wavelength hyperbolic instability (mode B) generally arises due to an unstable braid shear layer between two consecutive vortex structures. Here, two-dimensional vortices become distorted in the spanwise direction soon after the vortex pairing and eventually break up into small-scale vortices, and the related structure (mode B) maintains a shorter spanwise wavelength than those amplified through mode A.

4.4 Coherent flow features

4.4.0.1 Shear layer shedding characteristics in bluff body wakes

DMD analyses are conducted to understand the shear-layer instability mechanism further and identify the coherent structures more clearly. The method proposed by Schmid [31] is used for analysis, which is based on the snapshots for decomposing the fluid structures.

Initially, the DMD algorithm is applied to three-dimensional vertical velocity data on a sub-domain closer to the bluff body. The details of the time step, duration, and the number of snapshots for all the cases are tabulated in table 4.1. The total number of snapshots selected is large enough to ensure the DMD results converge. The obtained results for case

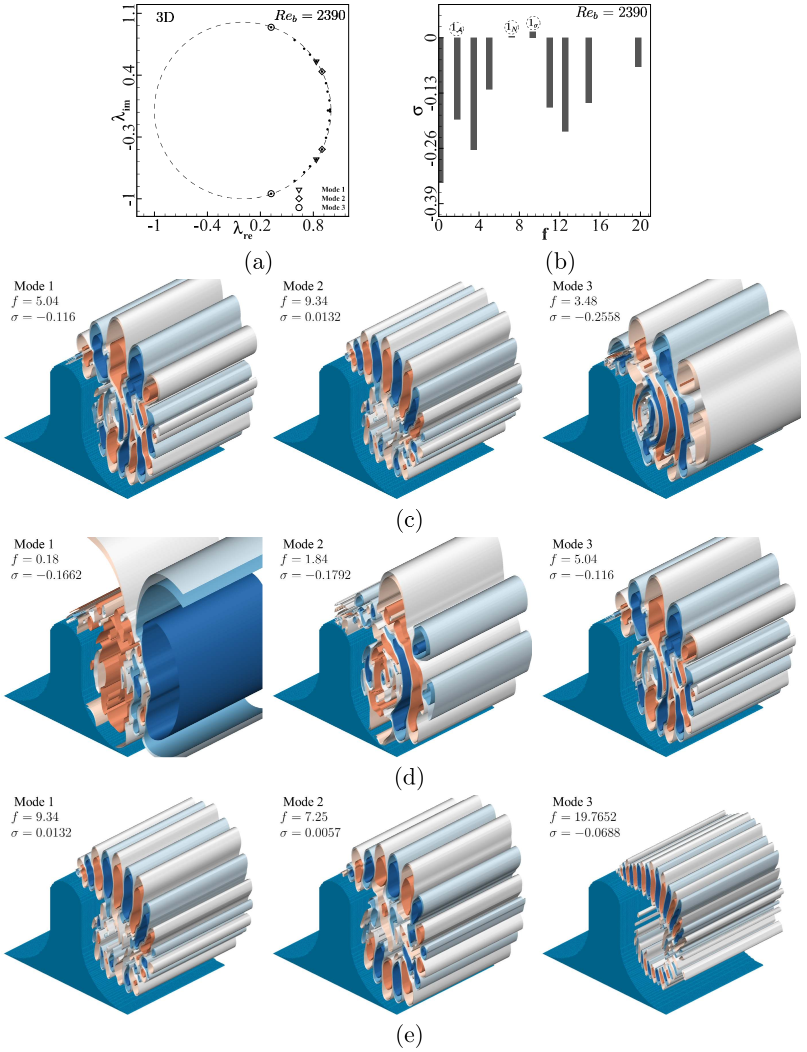

(a) (b)

(c)

(d)

(e)

Figure 4.6: Three-dimensional DMD analysis for case BC5. (*a*) Ritz circle; (*b*) growth rate vs. frequency; (*c*) leading modes based on amplitude values; (*d*) leading modes based on norm values; (*e*) leading modes based on growth rate values.

Case	t_{start}	t_{final}	Δt	No. of snapshots	σ_{max}	frequency ($f_{\sigma_{max}}$)
BC3	1.6	2.6	0.01	100	0.0163	4.43
BC4B	1.0	2.5	0.01	150	0.0714	7.33
BC5	1.87	2.60	0.01	73	0.0142	9.34
BC5(3D)	1.87	2.60	0.01	73	0.0132	9.34

Table 4.1: Dynamic mode decomposition analysis

BC5 are shown in figure 4.6. The Ritz values presented in figure 4.6 (a) show the stability of the modes. Here, the real and imaginary parts of the eigenvalues are taken as horizontal and vertical axes, respectively. Nearly all the values are clustered near the unit circle, hinting that the dynamics settle on an attractor. The growth/decay rate and frequencies of different modes are shown in figure 4.6 (b). Now, the mode having a frequency nearly equal to the peak frequency (f_v) is searched from the DMD analyses. Interestingly, the extracted peak frequency of vertical velocity (f_v) from the spectra analysis matches with DMD mode with the highest growth rate, as shown in figure 4.6 (b).

The contours of DMD modes obtained from the analysis are now arranged according to various criteria. The contours of the first three modes sorted based on amplitude, norm, and growth/decay rate are shown In figure 4.6 (c), (d), and (e), respectively. The highest mode obtained using amplitude, norm, and growth/decay rate are indicated by the subscript A, N, and σ, respectively, as shown in figure 4.6 (b). Coherent structures with alternate positive and negative regions can be seen in the contours. For simplicity, in many studies, the modes are sorted based on the value of amplitude. However, a mode with initially high amplitude can generally decay fast (first mode in figure 4.6 (c)). Also, such a method can ignore a mode with a relatively low amplitude but fast growth. In the second DMD mode, the frequency is equal to the shedding frequency. The third mode displays a similar distribution to the first two but with a lower frequency.

In figure 4.6 (d)), the modes are sorted Frobenius norms values. Here, the mode with the shedding frequency is not among the first three modes derived by norm calculation (figure 4.6 (d)). It is interesting to note, using norm criteria, the first two modes are large-scale structures with relatively low frequency. The third mode is the same as the first mode obtained using amplitude criteria. The first three modes with the highest growth rate are shown in (figure 4.6 (e)). The first two modes' frequency is nearly equal to the shedding frequency obtained from the spectra analysis. Here, the third mode is near the second harmonic of the fundamental shedding frequency. In comparison with the first two modes,

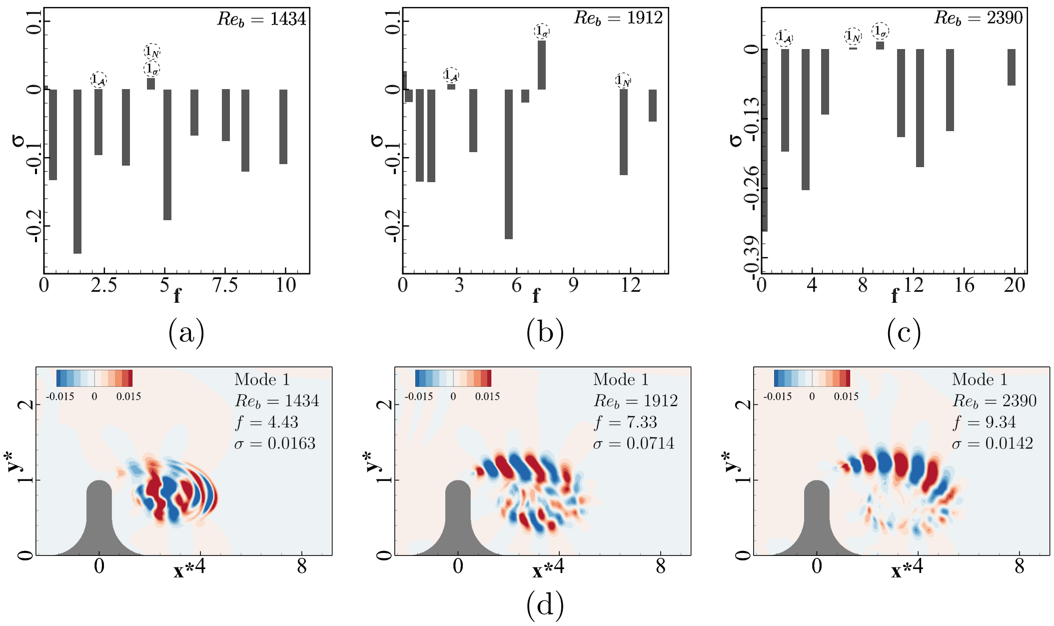

Figure 4.7: Two-dimensional DMD analysis for three Reynolds numbers (cases BC3, BC4B, and BC5). $(a - c)$ growth rate against frequency; (d) modes with the highest growth rate.

the spatial scale of the third mode is relatively small. Hence, DMD analysis separated the shear layer oscillations from the flow field using the growth rate criteria. Similar results are obtained by repeating the DMD analysis with spanwise vorticity data.

DMD analyses are repeated for two-dimensional data in the x-y plane (at the center of spanwise locations and full domain) obtained from the three-dimensional simulations for cases BC3, BC4B, BC5. The two-dimensional DMD analysis is nearly identical to the three-dimensional DMD analysis, as shown in table 4.1. The growth rate of different modes is obtained from the DMD analysis and plotted in figure 4.7(d). For all the cases, f_v value matches with DMD mode with the highest growth rate, as shown in figure 4.7. Here, all the leading modes exhibit a positive growth rate. For all the cases, alternate vertical velocity fluctuations are observed in the leading mode (figure 4.7 (d)). The shear layer oscillations in low Reynolds numbers (case BC3) are smaller and less developed than those in higher Reynolds numbers. For cases BC4B and BC5, the leading mode tracks the secondary shear layer vortex movement around the primary vortex. Due to the complex flow field from multiple vortices induced in bluff body wake, further investigations on the streamwise vorticity induction using the DMD method failed.

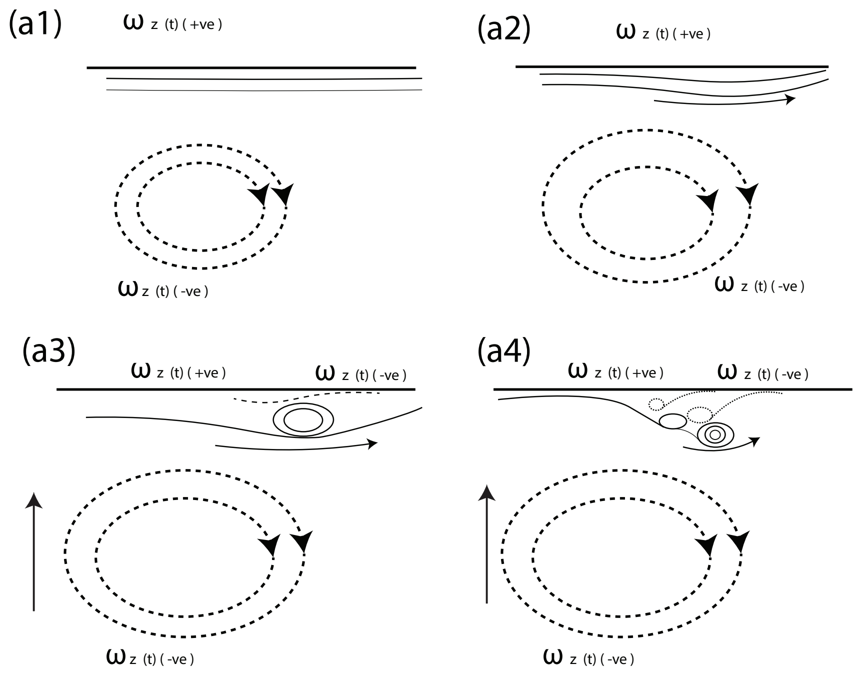

Figure 4.8: An illustration of the flow feature near the wall over the top wall.

4.5 Vorticity generation mechanism

Finally, we focus on the formation of wall vortices and the disintegration mechanism of the three-dimensional structures observed during the deceleration phase. It is likely that the generation and roll-up of near-wall vorticity is via a two-dimensional parent-offspring mechanism. Figures 4.8 and 4.9 illustrates the top and bottom wall vortex formation sequence. As evident from the simulation snapshots (4.1), initially, during the acceleration phase, the thickness of the vorticity sheet near the top wall (positive $\omega_z(t)$) increases with flow time (figure 4.8(a1) and (a2)). The advection and upward propagation of the primary vortex and shear layer structures cause the lifting of the near-wall vorticity sheets similar to the 'rebound' mechanism suggested by Harris and Williamson [91], as depicted in figure 4.8(a3). Convective vortices induce a region of adverse pressure gradient in the boundary layer in front of the moving vortex. Here, if the primary vortex is close enough to the wall and stays for a sufficient period, the lifting of vortex sheets and vortex-induced boundary layer separation is observed. During the deceleration phase (figure 4.8(a3)), patches of negative vorticity are formed near the wall. The separation occurs in the form of a small-sized eddy, which is of the opposite rotation to the primary convective vortex. Further deceleration leads to the roll-up of vorticity sheets and detachment of vortices from

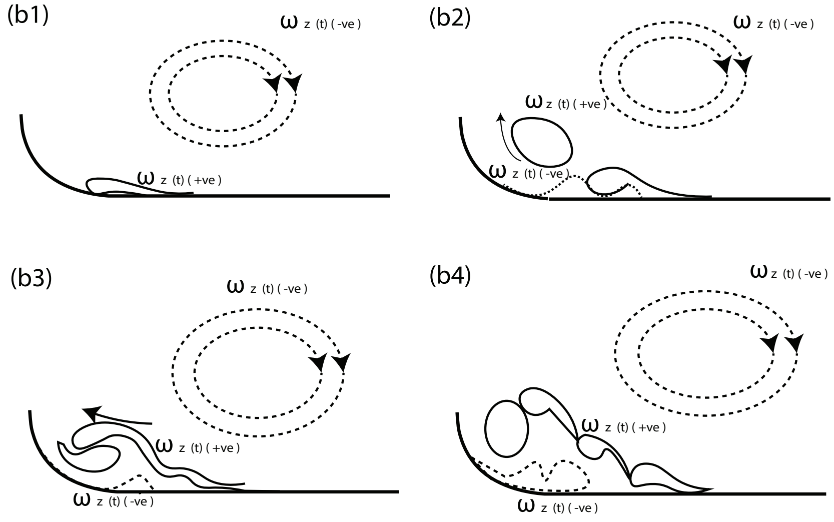

Figure 4.9: An illustration of the flow feature near the bottom wall.

the top-wall surface and ultimately provokes an eruption (figure 4.8(a4)). However, in two-dimensional simulations, the outbreak of small-scale vortices does not occur. Due to the mutual action of moving vortices and temporarily varying boundary layers, a gamut of complex and separation effects are observed in the wall proximity. The vortices detach from the wall, culminating in fluid ejection from the wall region.

A schematic of the sequence of events near the bottom-wall proximity is depicted in figure 4.9. The bottom-wall vortex generation mechanism is similar to the abovementioned top-wall separation mechanism. However, the flow structures are complicated by the curvature of the wall-attached bluff body. Here, the motion of the primary vortex causes the lifting of the near-wall vortices, as sketched in figure 4.9(b1). Opposite-signed vorticity rolls up near the curvature side of the bluff body immediately underneath the negative-signed primary vortex($SL0$). An increase in the vertical flow component causes the convection of wall-generated positive vorticity ($WB1$) into the core flow. This is evidenced by the propagation of newly formed positive vorticity. When the convected vortices are too close, merging/pairing of positive vortices is observed (figure 4.9(b2)). With further deceleration, intense, complex local interactions between merged positive wall-generated vorticity with near-wall negative vorticity are observed. The passage of near-wall vortices and interactions with opposite sign vortices cause the formation of new small-scale structures (figure 4.9(b4)). For all cases considered, three-dimensional effects are observed during the late stages of the decelerating phase. Further new simulations with extended steady or accelerating phases might manifest three-dimensional evolution in the early pulse phase.

As observed in many experiments and numerical studies, the flow transition from two-dimensional to three-dimensional can be related to the generation of streamwise vorticity. In order to understand the formation of three-dimensional structures, the incompressible form of the vorticity equation is considered analyzed.

$$\frac{D\omega_x}{Dt} = \overbrace{\omega_x \frac{\partial u}{\partial x}}^{\text{stretching}} + \overbrace{\omega_y \frac{\partial u}{\partial y} + \omega_z \frac{\partial u}{\partial z}}^{\text{tilting}} + \overbrace{\nu \nabla^2 \omega_x}^{\text{diffusion}} . \tag{4.1}$$

In equation 4.1, the first term on the right side represents the production of ω_x due to the stretching of vorticity-line elements. The following two terms describe the vortex line 'tilting'. The last term in equation 4.1 is the diffusion of vorticity due to viscous effects. For three-dimensional flows, equation 4.1 can be rewritten as:

$$\frac{\partial \omega_x}{\partial t} = \overbrace{-u\frac{\partial \omega_x}{\partial x} - v\frac{\partial \omega_x}{\partial y} - w\frac{\partial \omega_x}{\partial z}}^{\text{advection}} + \overbrace{\omega_x \frac{\partial u}{\partial x}}^{\text{stretching}} + \overbrace{\frac{\partial v}{\partial x}\frac{\partial u}{\partial z} - \frac{\partial w}{\partial x}\frac{\partial u}{\partial y}}^{\text{tilting}} + \overbrace{\nu \nabla^2 \omega_x}^{\text{diffusion}} . \tag{4.2}$$

The production of ω_x by tilting can occur through two mechanisms. The first mechanism (Ti_1) is due to the tilting of $\frac{\partial v}{\partial x}$ by the spanwise shear ($\frac{\partial u}{\partial z}$). The second mechanism (Ti_2) is the tilting of $\frac{\partial w}{\partial x}$ by the wall-normal shear ($\frac{\partial u}{\partial y}$). Hence, as evident from equation 4.2, the spanwise end-conditions (tilting terms) significantly affect the three-dimensional vorticity mechanism. It is important to note that the 3D simulations are performed using periodic boundary conditions to eliminate the boundary layer effects from the side walls. Such boundary conditions are intentionally imposed to match the inflow analytical boundary conditions obtained by neglecting the spanwise velocity variation. As revealed in several experimental studies [46, 92] in the past, the end conditions in the wind/water tunnel affect the coherent structures. Hence, the absence of a side-wall boundary layer changes the three-dimensional dynamics, which could be different from that obtained with a no-slip side-wall boundary condition. Due to the strain field created by the evolving spanwise vortex array and the wall effect, the vortices initially undergo tilting resulting in the formation of streamwise vorticity. The net streamwise vorticity production further amplifies by the vortex stretching process.

In order to analyze the contribution of each term in equation 4.2, the temporal variations of stretching and tilting terms at points near the top wall ($x^* = 6.7, y^* = 2.34$) and bottom wall ($x^* = 2.26, y^* = 0.167$) are plotted in figure 4.10(a) and 4.10(b) respectively. These points are inside the three-dimensional structures formed at the end of the deceleration pe-

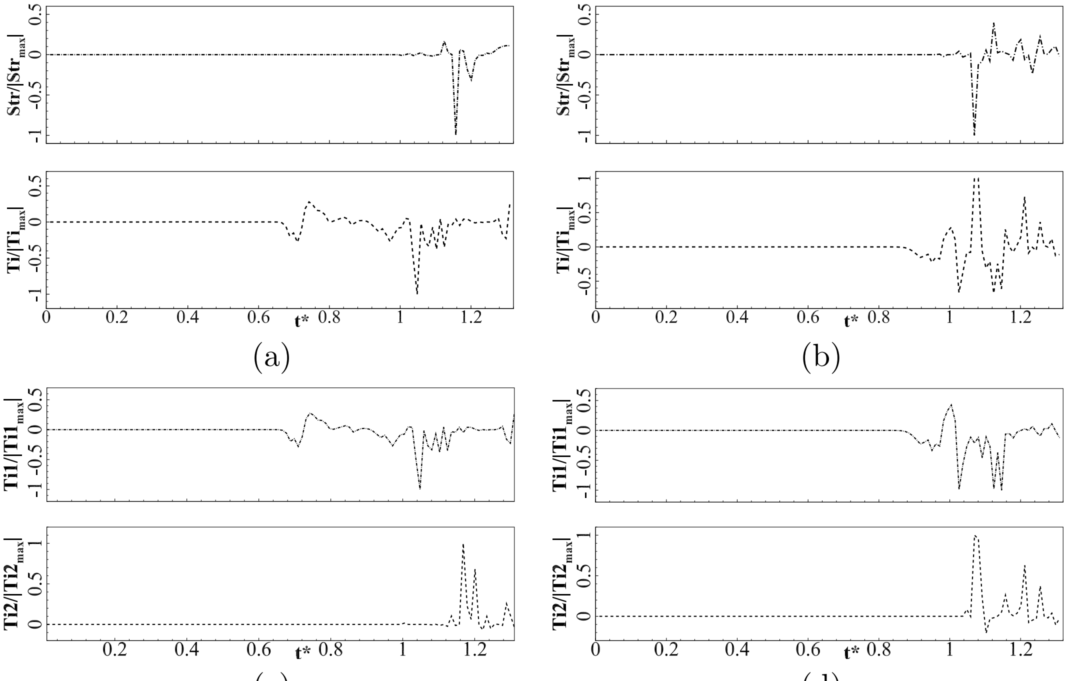

(a) (b)

(c) (d)

Figure 4.10: Temporal variation of streamwise vorticity generation in case BC5. (a) stretching and tilting terms at a point near the bottom wall; (b) stretching and tilting terms at a point near the top wall; (c) tilting components at a point near the bottom wall; (d) tilting components at a point near the top wall.

riod. A substantial increase in tilting and stretching terms is observed during the end of the deceleration phase, as evident in figure 4.10(a) and 4.10(b). Deceleration induces velocity variation along the streamwise direction, affecting the stretching term. The strong presence of stretching terms is observed over the crippling parts of vortices. The tilting mechanism can be seen as a result of two components (equation 4.1). Figures 4.10(c) and (d) show the temporal evolution of the tilting term components at points near the top and bottom walls, respectively. In each flow phase, s difference in temporal evolution is observed for each tilting component. During the initial stages, the major contributors are the spanwise vorticity and the spanwise shear. Due to deceleration, the spanwise vorticity magnitude reduces in the later flow phase while the wall-normal vorticity and wall-normal shear components increase. Simultaneous to three-dimensional breakdown, a spike in stretching and second tilting term components can be identified.

4.6 Summary

Three-dimensional transition in an unsteady wake of the body offering a strong spatial gradient closely relies on the mean inflow velocity and temporal parameters. Unlike a two-dimensional simulation producing advection of the vortex flow features, three-dimensional simulations indicate a multitude of transition mechanisms inducing spanwise oscillations. The major deviation is through the decay of the streamwise velocity during the deceleration phase creating flow features susceptible to the spanwise oscillation growth.

An in-depth analysis of the spatial features of the underlying flow features is carried out through the λ_2 method. Though the two-dimensional vortex flow features provide a preliminary picture of the transition mechanism developed in the bluff body wake, the core structure of the flow field is identified through the λ_2 method. Vortex flow structures identified distinguish two different instability mechanisms induced inside the flow field and are closely related to the vortex-pair nature. Due to the strong spatial gradient, the leeward side instigates higher boundary layer vortices, which are shed due to the shear layer vortex movement. Further, these vortex structures pair, creating an unstable braid region producing a series of small three-dimensional loops with lower wavelengths (mode B). Simultaneously, decelerating high-velocity region induces top boundary layer vortices to eject into the flow, forming a counter-rotating vortex pair which later transit into high wavelength instability (mode A).

The three-dimensional coherent flow features are investigated through a reduced-order modeling approach. Important mode shapes, frequencies, and growth/decay rates were identified using dynamic mode decomposition. Modes are arranged based on amplitude, norm, and growth rate values. The dominant mode, as determined by amplitude criteria, shows a high decay rate, whereas the dominant mode, as determined by norm value, is a large-scale structure with relatively low frequency. With the DMD analysis, the primary and secondary harmonics associated with the shear-layer instability are obtained, and flow characteristics are separated from the flow field using the growth rate criterion.

Finally, the growth of the three-dimensional oscillation is analyzed based on streamwise vorticity formation providing insight into the three-dimensional disintegration mechanism and aiding in a better understanding of vorticity dynamics. Through a detailed analysis of the temporal growth of each term in the streamwise vorticity generation equation, it identifies the development of the tilting mechanism during the deceleration phase, which is further amplified by the stretching term during the zero-mean inflow phase.

Chapter 5

Wake transition in a diverging channel

5.1 Introduction

This chapter discusses flow features evolving in a diverging channel under a trapezoidal variation of the mean inflow condition. The flow parameters are selected based on the experiments of Das et al. [2] and extended to isolate the effects of varying mean inflow velocity and deceleration parameters. Further, the analysis of the three-dimensional vortex disintegration evidenced three types of flow evolution. The simulation cases are categorically placed into three different sets based on the non-dimensionalized three-dimensional disintegration time. The first type of flow shows a two-dimensional nature with the vortex flow features disintegrating through a diffusion process. In the second category, the coherent structures indicate a stationary nature, and during the zero inflow phase, the counter-rotating vortex pair leads to the development of an elliptically unstable nature. Later, a locally chaotic structure is formed in the initial diverging section. The flow features in the third group show a convective nature, and the three-dimensional instability is formed in the decelerating phase. The chaotic structure formed during the deceleration phase also evidences characteristics of the merging phenomenon.

Along with a detailed description of the three-dimensional flow evolution and classification, the current chapter also focuses on the development of the spanwise circulation, the growth of boundary layers, and their inflectional nature. Discussions on the secondary instability nature and coherent structures are introduced and are detailed in the subsequent chapter. Specific information on the computational domain and numerical parameters are given in section 5.2. Common traits of the flow features developed in the diverging channel flow and the classification methodology adopted are discussed in section 5.3. Section 5.4 outlines the flow features developed in an advecting and decaying two-dimensional case (Type I). The evolution of a locally turbulent three-dimensional structure in the second cat-

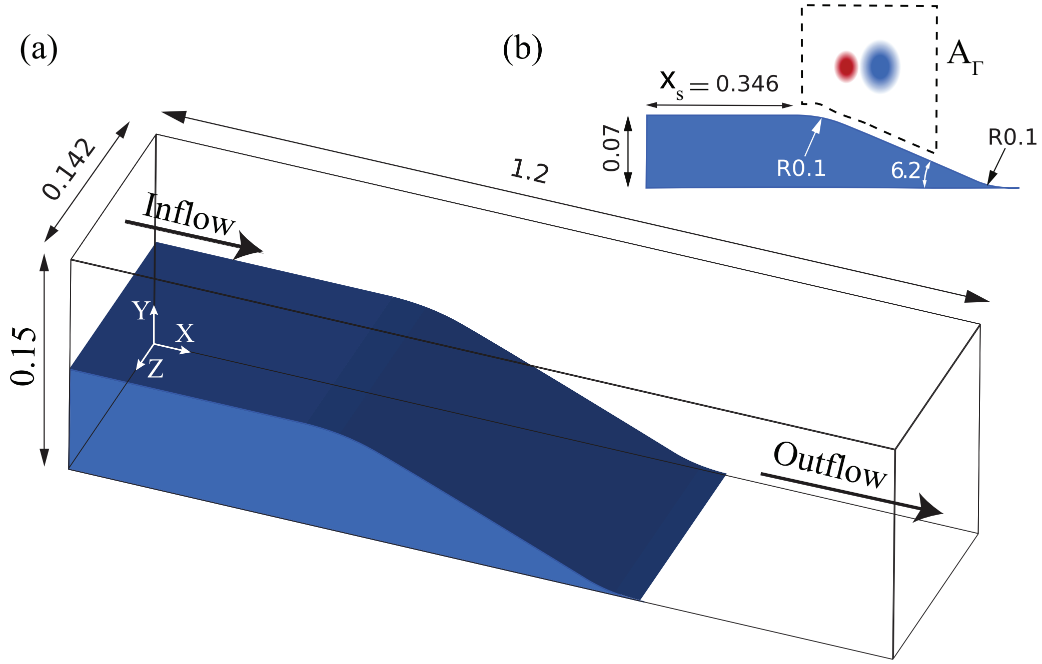

Figure 5.1: Computational domain along with boundary conditions: (a) three-dimensional view of the computational domain, (b) dimensions of the diverging section.

egory of cases is detailed in section 5.5. Section 5.6 provides a detailed picture of flow features developing in spatially turbulent cases (Type III). Finally, a consolidation of the flow evolution and the three-dimensional nature of flow features is presented in section 5.7.

5.2 Computational domain and simulation parameters

5.2.1 Computational Domain

A sketch of the computational setup of flow in a diverging channel is shown in figure 5.1. The computational domain chosen for this study is a small segment of the experimental setup employed by Das et al. [2]. Here, X, Y, and Z are streamwise, wall-normal, and spanwise distances, respectively. In the simulation, the computational domain has a length of 1.2 m, a width of 0.142 m, which is equal to half the width of the experimental section, and a height of 0.15 m, as illustrated in figure 5.1(a). The embedded body section has a height of 0.07 m at the constant channel section. After a length of 0.3464 m, the edge starts to curve along an arc with a radius of 0.1 m. Later, the curve joins smoothly to the diverging section with an angle of depression $6.2°$ (figure 5.1(b)). Similarly, the end of the

Case	U_p (m/s)	t_0 (s)	t_1 (s)	t_2 (s)	t_s (s)	Re_d	Re_h	Re_{δ_s}	t^*_{3D}
A1	0.1372	0.6	2	3.00	2.15	8381	10976	750	–
A2	0.1372	0.6	2	5.00	2.55	4840	10976	810	–
A3	0.1372	0.6	2	8.00	3.15	3422	10976	861	–
B1	0.1830	0.8	1	1.55	1.18	13052	14640	544	–
B2	0.1830	0.8	1	2.33	1.50	8393	14640	613	–
B3	0.1830	0.8	1	5.00	2.25	4840	14640	865	–
C1	0.2745	1.2	2	2.83	2.09	13013	21960	1449	3.67
C2	0.2745	1.2	2	4.00	2.21	8383	21960	1530	1.58
C3	0.2745	1.2	2	8.00	2.48	4840	21960	1707	0.53
D1	0.3203	1.4	2	3.17	2.11	11839	25624	1666	2.26
D2	0.3203	1.4	2	4.08	2.21	8879	25624	1694	1.29
D3	0.3203	1.4	2	9.00	2.46	4840	25624	2020	0.38

Table 5.1: Simulation parameters ($Re_a = 10822$). The boundary layer thickness (δ_s) is calculated over the separation point of the diverging channel.

diverging part joins fluidly with the bottom wall of the channel.

The no-slip boundary condition is enforced on both top and bottom walls for devising identical experimental setup conditions in the computational domain. A time-varying inlet condition based on the analytical solution (equation 2.8) of trapezoidal mean flow variation is imposed at the inlet of the computational domain. The free-slip condition is applied to both the right and left boundaries. Similar to the bluff body case, the one-dimensional advective outflow equation is implemented as the exit boundary condition given as:

$$\frac{\partial u}{\partial t}|_{\mathrm{X}=l_x} + U_c \frac{\partial u}{\partial \mathrm{X}}|_{\mathrm{X}=l_x} = 0. \tag{5.1}$$

Where the mean velocity of the inlet velocity profile is taken as the advection velocity (U_c) and l_x is the domain length in the streamwise direction.

5.2.2 Physical and numerical parameters

In this chapter, flow features are illustrated using non-dimensional spatial scales. Streamwise distance is non-dimensionalized as $x = \frac{X-X_s}{h_b}$, where h_b is the embedded body height at the inlet and X_s denote the start of the diverging section ($X_s = 0.3464$). Wall-normal and spanwise distances are non-dimensionalized by using the body height defined by $y = \frac{Y}{h_b}$ and $z = \frac{Z}{h_b}$ respectively. As in the experiments of Das et al. [2], the working fluid is selected to be water with a kinematic viscosity (ν) of $10^{-6}\ m^2/s$. The parameters provided below are used to analyze the flow dynamics:

Reynolds number:

$$Re_h = \frac{U_p h}{\nu}. \tag{5.2}$$

Acceleration Reynolds number is defined as:

$$Re_a = \sqrt{\frac{a h^3}{\nu^2}}. \tag{5.3}$$

where h is the inlet channel height, and a is the acceleration $\left(\frac{U_p}{t_0}\right)$. Similarly, for varying deceleration cases, a deceleration Reynolds number is defined by:

$$Re_d = \sqrt{\frac{d h^3}{\nu^2}}, \tag{5.4}$$

here, d is the deceleration $\left(\frac{U_p}{t_2 - t_1}\right)$. In the present work, the Reynolds numbers based on the viscous length scales are defined as follows:

$$Re_\delta = \frac{U_p \delta}{\nu} \quad \text{and} \quad Re_{\delta^*} = \frac{U_p \delta^*}{\nu}, \tag{5.5}$$

where, δ and δ^* represents boundary layer and displacement thicknesses respectively. Circulation of vortices for a particular time instance is calculated by: $\Gamma_{\omega_z} = \iint_{A_\Gamma} \omega_z \, dA$. Here, the area A_Γ is set appropriately to determine the circulation for top and bottom vortex flow features while omitting the wall boundary region (as depicted in figure 5.1(b)), and ω_z indicates the spanwise vorticity $\left(\omega_z = \frac{\partial v}{\partial X} - \frac{\partial u}{\partial Y}\right)$. Similar to other vortex flow evolution studies [93, 94], the vortex Reynolds number based on spanwise circulation is estimated by:

$$Re_{\Gamma_{\omega,z}} = \frac{\Gamma_{\omega_z}}{\nu}. \tag{5.6}$$

Table 5.1 shows the simulation parameters for 12 different flow cases. Each case is assigned an alpha-numeric code to identify its simulation parameters. Of 12 simulations, cases with identical mean inflow velocity (U_p) are marked by alphabets A, B, C, and D, respectively, for low, moderate, high, and very high inflow velocities. In addition, numerical letters indicate cases with different deceleration parameters and the same Reynolds number; numbers 1, 2, and 3 refer to high, moderate, and low deceleration. For all the cases, the acceleration Reynolds number (Re_a) is kept constant at 10822. The Reynolds number

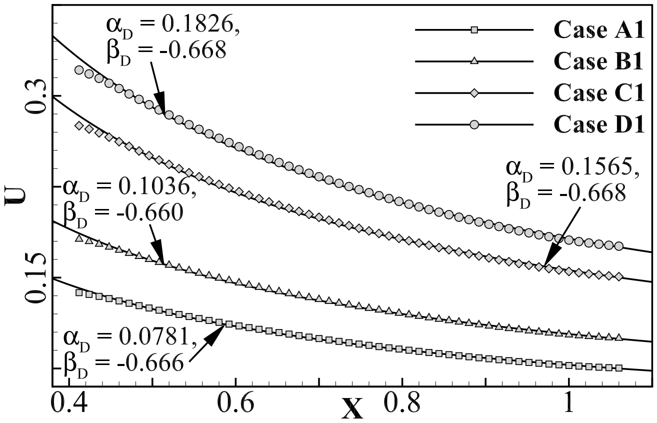

Figure 5.2: Streamwise velocity variation in the inviscid region along the streamwise direction ($y = 1.4286,\ z = 1.0$)

based on the boundary layer thickness (Re_{δ_s}) for all cases at separation time is given in Table 1.

As a measure of the spatial pressure distribution, the variation of the streamwise velocity component in the inviscid region (U_x) along the streamwise direction is shown in figure 5.2. The velocity profile is shown at half the constant velocity period. The velocity variation in the diverging section (from $X = 0.4$ to $X = 1.06$) can be approximated by using the relation:

$$U_x = \alpha_D x^{\beta_D}, \tag{5.7}$$

where the α_D and β_D are constants and vary with Reynolds number (Re_h). Since the acceleration and constant inflow velocity period remain the same, α_D and β_D remain the same for varying deceleration cases. In figure 5.2, the continuous line represents the fitted curve, while the symbols represent the velocity obtained from the simulation. The symbols are placed at a distance of 15 grid point spaces between each. The obtained values for α_D and β_D for all cases are marked in figure 5.2.

The following non-dimensionalized time scales are used to distinguish flow events. At first, flow time is non-dimensionalized by t_2 to differentiate between both the pulse phase and the zero mean inflow period ($t^* = \frac{t}{t_2}$). In order to compare different deceleration cases, a non-dimensionalized time scale is identified as $t^*_d = \frac{t-t_1}{t_2-t_1}$. Also, a critical flow time associated with three-dimensionally unstable cases t^*_{3D} $\left(t^*_{3D} = \frac{t_{3D}-t_1}{t_2-t_1}\right)$ is identified from the t_{3D}, physical time at which a visible secondary instability initiates in three-dimensionally unstable cases. The t^*_{3D} observed for cases showing three-dimensional disintegration is provided in table 5.1. In low and moderate Reynolds number cases, the flow stays in the two-dimensional regime; hence, the t^*_{3D} is absent for these cases.

5.2.3 Grid independence and numerical validation

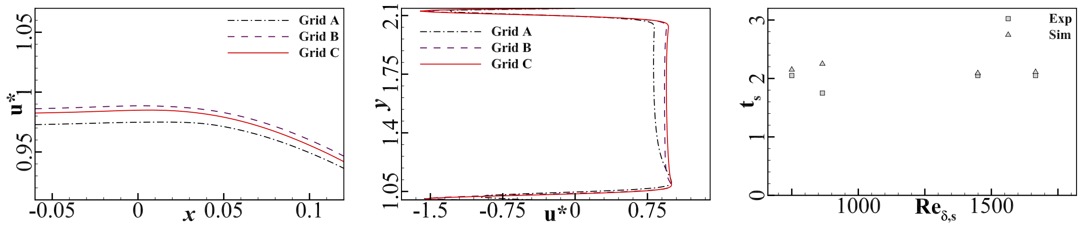

(a) (b) (c)

Figure 5.3: Computational model validation: (a) Streamwise velocity variation in streamwise direction (before separation ($t^* = 0.631$)), (b) streamwise velocity variation in wall-normal direction (after separation ($t^* = 0.946$)) and (c) experimental comparison of t_s.

The grid-independent analysis is performed by comparing the evolution of streamwise velocity (Case D1) for different grids with elements of $961 \times 193 \times 181$ (grid A), $1501 \times 301 \times 289$ (grid B), and $1921 \times 385 \times 361$ (grid C). Figure 5.3(a) shows the streamwise velocity through the central axis ($y = 1.3143,\ z = 1.0$) of the diverging channel at the end of the constant velocity phase for different grid sizes. The velocity component is non-dimensionalized by the maximum velocity magnitude for the flow instance $\left(u^* = \frac{u}{u_{max}}\right)$. The velocity profiles for three different grid sizes are shown in figure 5.3(b) following the onset of initial instability at $x = 0.5,\ z = 1.0$. Grids A and B differ by approximately 1.5%, three times greater than grids B and C. The root mean square deviation (RMS) of the streamwise velocity component (u_{rms}) of the velocity field during the constant mean inflow phase is calculated as:

$$u_{rms} = \left(\frac{1}{N} \sum_{l=1}^{l=N} (u'(l))^2 \right)^{1/2}, \tag{5.8}$$

where the velocity perturbation (u') is calculated by:

$$u'(l) = u(l) - u_{mean}, \text{ and } \quad u_{mean} = \frac{1}{N} \sum_{l=1}^{l=N} u(l), \tag{5.9}$$

For N snapshots belonging to the constant velocity phase. A comparison of the root mean square deviation of the streamwise velocity component developed over the constant mean inflow period reveals a difference of 8.4% between grids A and B, while the difference between grids B and C is below 4%. Consequently, grid B is selected for the numerical simulations due to the accuracy and computational economy. Based on time step dependency analysis with time steps ranging from 1×10^{-3}s to 1×10^{-5} s, a time step of 1×10^{-4} s (CFL = 0.02) was found to be computationally and accurately affordable.

Comparison of time of flow separation (t_s) with the results of Das et al. [2] (figure 5.3(b)) validates the computational method. The previous experimental works incorporated a two-dimensional simulation of vortex evolution to calculate flow separation time. Here, by taking the flow time and position of zero wall shear stress, we determine the flow separation time and separation point. All the cases show an excellent match with the reported experimental values (less than 8%). An experimental and simulation comparison of the flow field for a high-velocity case is provided in section 5.3.

5.3 Initial Observations and Flow Classification

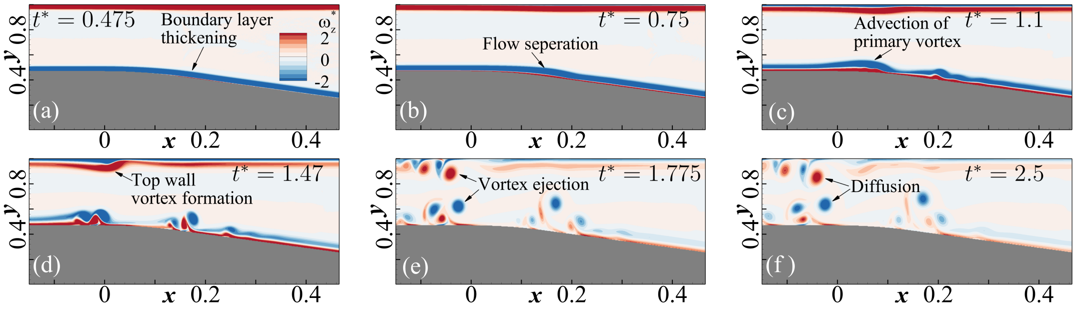

Figure 5.4: Flow evolution at low Reynolds number case (Case A3): (a) boundary layer thickening, (b) initial oscillation, (c) vortex formation, (d) vortex formation top wall, (e) vortex detachment, and (f) interaction of top and bottom wall vortices.

Initially, the contour of non-dimensional spanwise vorticity $\left(\omega_z^* = \frac{\omega_z h}{U_p}\right)$ at various flow instances is used to analyze the evolution at low and high Reynolds number cases. Figure 5.4 illustrates the contours of spanwise vorticity at six flow instances for low-Reynolds number (case A3). The boundary layer thickness increases temporally due to the transient inflow boundary condition (figures 5.4(a) and 5.4(b)). The flow generally remains attached to the channel surface during the acceleration and constant velocity phases. Further, the flow undergoes two-dimensional inflectional flow instability during the deceleration

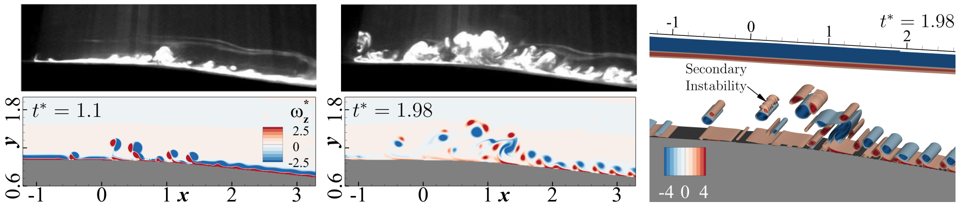

(a) (b)

Figure 5.5: Flow evolution at the high Reynolds number (Case C1) compared with the experimental snapshots of Das et al. [2] (a) two-dimensional snapshots, and (b) three-dimensional snapshots.

phase. Associated vortex formation occurs either during deceleration or zero mean velocity phases, as reported in previous experiments. The formation of the separation bubble is evident in figure 5.4(b) at the initial part of the diverging section ($x = 0$ to 2). Initial instability amplifies with the flow time, resulting in shear layer roll-up (figure 5.4(c)). Due to the reverse velocity profiles formed near the channel surface during the deceleration phase, the shear layer vortices advect into the upstream region as the flow progresses.

Analogous to the bottom wall-flow features, the oscillation developed over the top wall moves upstream during the deceleration phase (figure 5.4(d)). As a result of the primary negative vortex developed during deceleration, a secondary positive vortex is induced from the bottom wall. During the zero mean inflow phase, vortices eject from the top and bottom channels as a result of the mutual induction of vortex pairs (figure 5.4(e)). Further, both top and bottom wall vortices diffuse during the zero inflow phase (figure 5.4(f)). The initial development of flow instability in the case of a high Reynolds number is qualitatively similar to the low Reynolds number case. At high Reynolds numbers, characteristic features such as boundary layer thickening, inflectional instability, and shear layer roll-up are observed. However, the subsequent evolution of vortices varies depending on the Reynolds number and deceleration rate. The structures exhibit secondary instability at high Reynolds numbers, and subsequently, the flow becomes turbulent. The spreading and development of three-dimensional structures differ with the deceleration rate.

Figure 5.5 shows the comparison of flow evolution in numerical simulation with experimental results of Das et al. [2]. At $t = 3.13$ s, dye visualization manifests the formation of vortices in the diverging part, and similar flow formations are observable in the spanwise vorticity contours of simulation results. Vortex structures spread locally over the initial diverging section ($x = 0.5$ to 2). The maximum pressure gradient point also lies in the initial diverging section ($x \approx 0.46$). The upward movement of vortices is apparent dur-

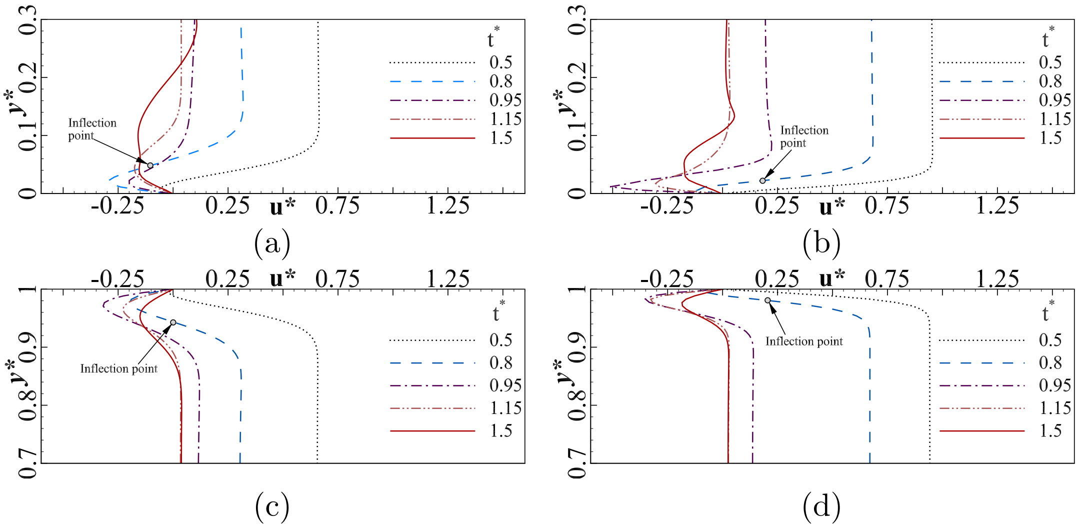

(a) (b)

(c) (d)

Figure 5.6: Velocity profiles across the separation point: (a) bottom wall (case A3, $x = 0.0615$), (b) bottom wall (case C1, $x = 0.0635$), (c) top wall (case A3), and (d) top wall (case C1).

ing the deceleration period. Simultaneously coalescence of multiple vortex structures is also noticeable. At $t = 5.6$ s, the spanwise vorticity contour of numerical simulation also demonstrates the secondary instability formations. However, a dense cloud of dye can only be seen in the experimental visualization. A three-dimensional development of the vortex interaction makes dye visualization challenging due to the difficulty in identifying individual vortex structures. Localized turbulent vortex formations are observed near the maximum pressure gradient region of the diverging section. Similar to the dye visualization images, the onset of secondary instability over spanwise vortex structures at the end of the constant area section of the channel is visible in the three-dimensional snapshot (figure 5.5(b)). The spanwise oscillation evolution is evident, indicating an onset of secondary instability in flow evolution.

As a result of the APG conditions, inflectional profiles develop, which can eventually lead to boundary layer separation, instability, or both. Figure 5.6 compares the inflectional nature of flow instability associated with the two-dimensional primary instability for low and high Reynolds number cases. Figures 5.6(a) and (b) indicate the temporal evolution of instantaneous streamwise velocity profiles developed over the bottom wall in low Reynolds number (case A3) and high Reynolds number (case C1) cases, respectively. During the acceleration phase, the velocity profile is close to the wall surface without any reverse flow region. Here, the velocity profiles are similar to the wall-jet profiles during the deceleration phase. Depending on the Reynolds number and the deceleration rate parameters, reverse flow velocity profiles are observed at specific locations and instances. Since both cases differ in deceleration characteristics, the profiles show slight variations in the initial phase ($t^* = 0.5$).

The flow enters into the deceleration phase resulting in a flow separation in case A3, while case C1 lies in the constant velocity phase. A strong adverse pressure gradient develops when the inflow decelerates, resulting in a reverse flow region. At $t^* = 0.8$, both cases indicate a reverse flow region, while for case A3, the profile is highly inflectional. In the high deceleration case (case C1), the profile is highly inflectional, close to the end of deceleration ($t^* = 0.95$). The extent of the reverse flow zone declines in the zero mean inflow region ($t^* = 1.15$), and the velocity profiles also alter due to the spanwise vortices passing through the selected point ($t^* = 1.5$). The velocity profile developed over the top wall is illustrated in figures 5.6(c) and (d) for cases A3 and C1, respectively. Similar to the bottom wall velocity profiles, the top wall velocity profiles follow the same evolution pattern. Top wall velocity profiles tend to show a higher boundary layer region than bottom wall velocity profiles.

Based on secondary instability features and secondary instability initiation time (discussed in detail in the subsequent sections of the chapter), the simulation cases are classified into three categories. A schematic representation of the development of vortices at two critical flow instances in each category is shown in figure 5.7. The type I category represents low and moderate inflow velocity cases, which do not exhibit spanwise oscillations and remain two-dimensional. Mutual induction of primary and secondary vortices evolved during the flow progression is indicated in the right inset of figure 5.7(a). Vortex pairs stretch, diffuse, and do not exhibit three-dimensional oscillations when in motion.

The second category, type II, a secondary vortex that emerges from the bottom boundary in the zero mean inflow phase (after the deceleration phase, mean velocity of the inflow velocity profile is zero), exhibits secondary instability and three-dimensional oscillations. Vortex evolution in a locally unstable three-dimensional case (type II) is illustrated in figure 5.7(b). Here, the value of secondary instability initiation time (t^*_{3D}) is significantly higher than one. In a rapidly decelerating case, as depicted in the left inset of figure 5.7(b), the flow generally takes a route similar to the two-dimensional instances during the initial stages. Flow structures evolve near the separation bubble and move upstream during the zero mean inflow stage. However, shear layer vortices undergo secondary instability, characterized by a spanwise oscillation with a wavelength λ, as indicated by the right inset figure in figure 5.7(b). The spanwise oscillation intensifies with flow time, culminating in

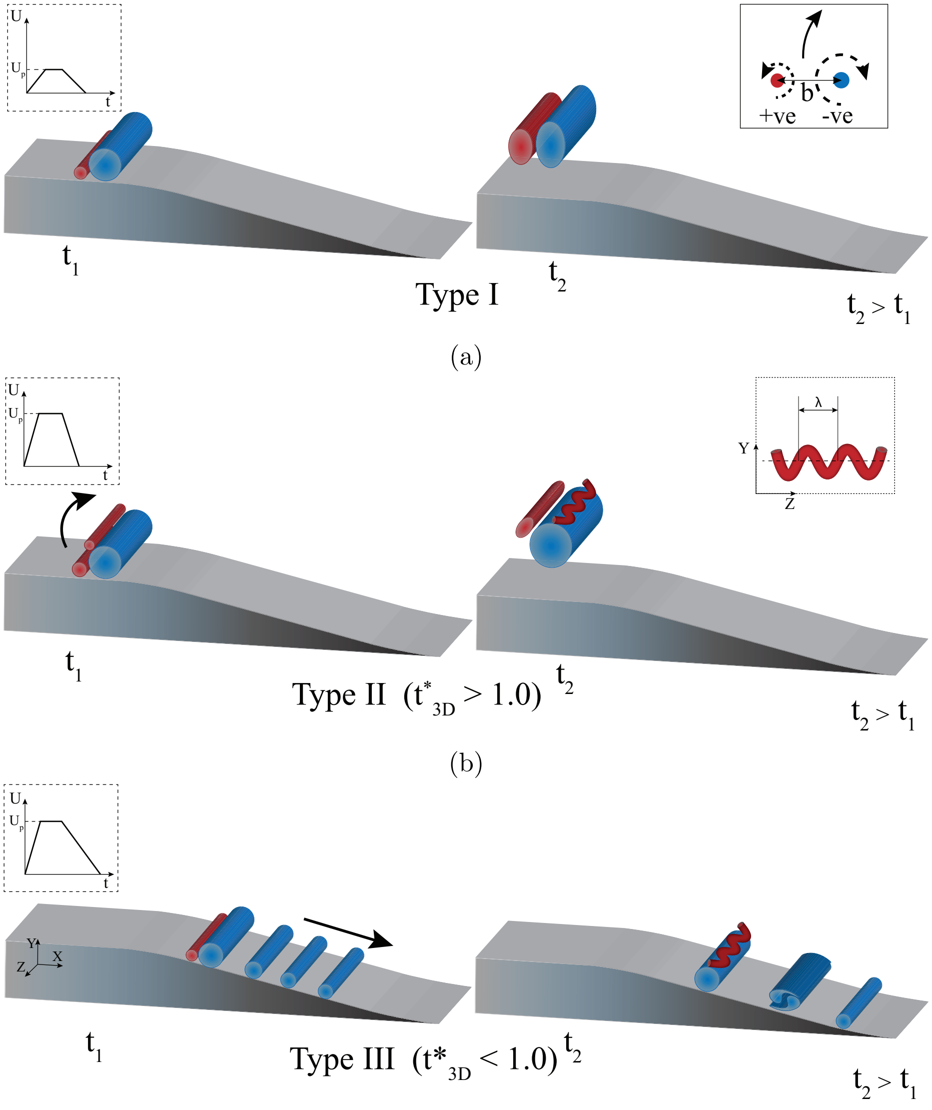

Figure 5.7: Illustration of flow evolution for: (a) type I: advecting and decaying two-dimensional vortices, (b) type II: local instability formation, and (c) type III: spatially unstable flow scenarios.

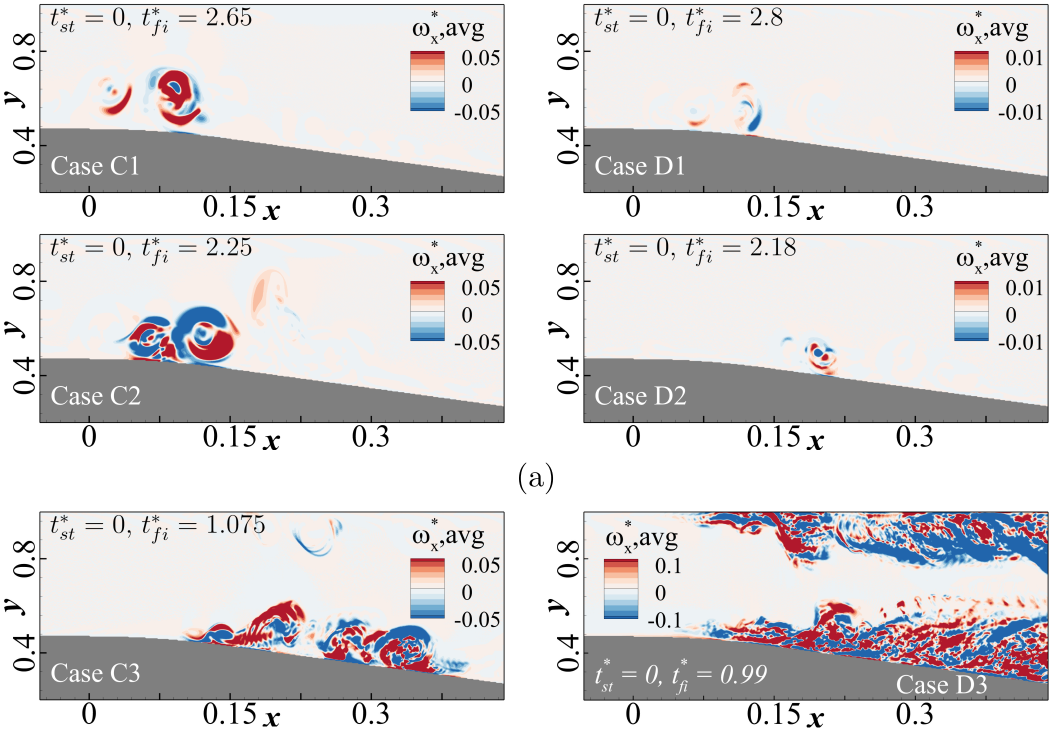

(a)

(b)

Figure 5.8: Temporally averaged streamwise vorticity in three-dimensional cases belonging to (a) locally unstable flow evolution cases (type II), and (b) spatially unstable flow evolution cases (type III).

a locally turbulent structure.

In the third category, the flow shifts from two-dimensional to three-dimensional during the deceleration phase ($t^*_{3D} < 1$). The extended deceleration period induces continuous shedding of vortex structures from the separation bubble and advection of the vortex structures. Figure 5.7(c) illustrates the development of spatially unstable flow with multiple vortices formed over the bottom wall. Due to the streamwise movement of primary vortices over diverging sections, vortex structures downstream merge to form a large structure, further instigating three-dimensional flow characteristics. Advecting three-dimensional structures from the separation bubble and the associated three-dimensional vortices creates turbulent flow in the downstream diverging region.

Analogous to the bluff body wake, the contour of streamwise vorticity $\left(\omega_x = \frac{\partial w}{\partial Y} - \frac{\partial v}{\partial Z}\right)$ can reveal the onset and spread of turbulence. A temporally averaged two-dimensional snapshot of non-dimensional streamwise vorticity $\left(\omega^*_x = \frac{\omega_x h}{U_p}\right)$ for three-dimensional cases is presented in figure 5.8. For N number of snapshots, a temporally averaged streamwise vorticity is obtained by:

$$\omega_x^*, avg = \frac{1}{N}\sum_{l=1}^{l=N} \omega_x^*(l).$$

Flow field data between flow instances t_{st}^* taken as the first snapshot and t_{fi}^* taken as the final snapshot are used to perform temporal averaging, and respective values for each case are given in figure 5.8. For locally unstable cases (cases C1, C2, D1, and D2), a time-step of 0.05 s is used, while for spatially unstable cases, a time-step of 0.1 s is used (cases C3 and D3). The first category of cases (Type I) represents two-dimensional spanwise vortices that advect and decay in the channel region. Therefore, a temporal average of streamwise vorticity does not yield valid results for this category (cases A1 - A3 and cases B1 - B3) and is hence excluded in figure 5.8. The second category of cases illustrates the flow features evolving near the separation region. In these cases, the spanwise flow formations remain confined to the entrance of the diverging area and generate three-dimensional oscillations on the secondary vortex structures during the zero mean flow stage. The formation of streamwise vorticity also remains confined to a narrow region near the separation bubble. The third flow category (type III) involves periodic vortex shedding, secondary instability, and vortex merging. Flow features develop near the separation region and advect downstream during the deceleration phase. Such cases manifest three-dimensional oscillation in the deceleration phase and disintegrate at a later flow instance. The streamwise vorticity formed over the diverging section is indicative of turbulent advective flow for the third category, as shown in figure 5.8(b). Near the top wall, streamwise vorticity production indicates similar three-dimensional disintegration of top wall vortex structures.

5.4 Type I: advecting and decaying two-dimensional vortices

We now investigate the effect of Reynolds number, and deceleration rate, on vortex flow evolution characteristics in the first flow category. Figure 5.9 depicts the temporal variation of the Reynolds number based on the displacement thickness calculated using the velocity profile over the separation point for cases belonging to the first category. As the flow accelerates, a thin boundary layer appears over the bottom wall. Broadening of the boundary layer during the change in the mean inflow velocity phase causes an increase in displacement thickness. The displacement thickness remains nearly constant during the constant

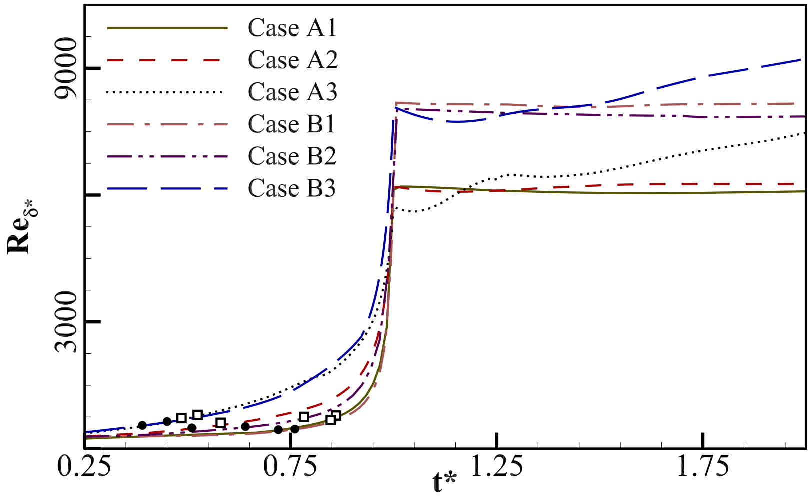

Figure 5.9: Temporal evolution of Reynolds number based on displacement thickness for advecting and decaying cases (filled circle: t_s, open square: t_v) over the separation point.

velocity phase (figure 5.9). For high deceleration Reynolds number cases (cases A1 and B1), deceleration happens in a short period, resulting in a significant increase in displacement thickness. During the zero mean inflow phase, the reverse flow region remains constant, manifesting a constant Re_{δ^*}.

Both low and moderate Reynolds number cases show identical flow evolution and are evidenced by the displacement thickness variation. A gradual increase in displacement thickness for low deceleration cases (cases A3 and B3) is attributed to the more extended deceleration period. The time at which wall shear stress is zero (t_s) and vortex formation time (t_v) are marked with filled circles and hollow square symbols, respectively. Figure 5.9 shows that two-dimensional flow separations occur in the Re_{δ^*} band of 420 to 640, and vortex formation occurs between 560 and 780. During the zero mean inflow phase, the vortices pass across the separation point, causing the abnormality in the temporal variation of displacement Reynolds number.

The three-dimensional vortex structures developed in zero mean inflow phase ($t^* = 2.0$) for advecting and decaying cases exhibit distinct two-dimensional evolution characteristics (figure 5.10). The initial flow develops along the general route of broadening boundary layer thickness, inflectional streamwise velocity profile, followed by flow separation. In figure 5.10, the most amplified vortex pair formed due to the inflectional instability is labeled by BV and bv for primary and secondary vortices, respectively. Vortex structures

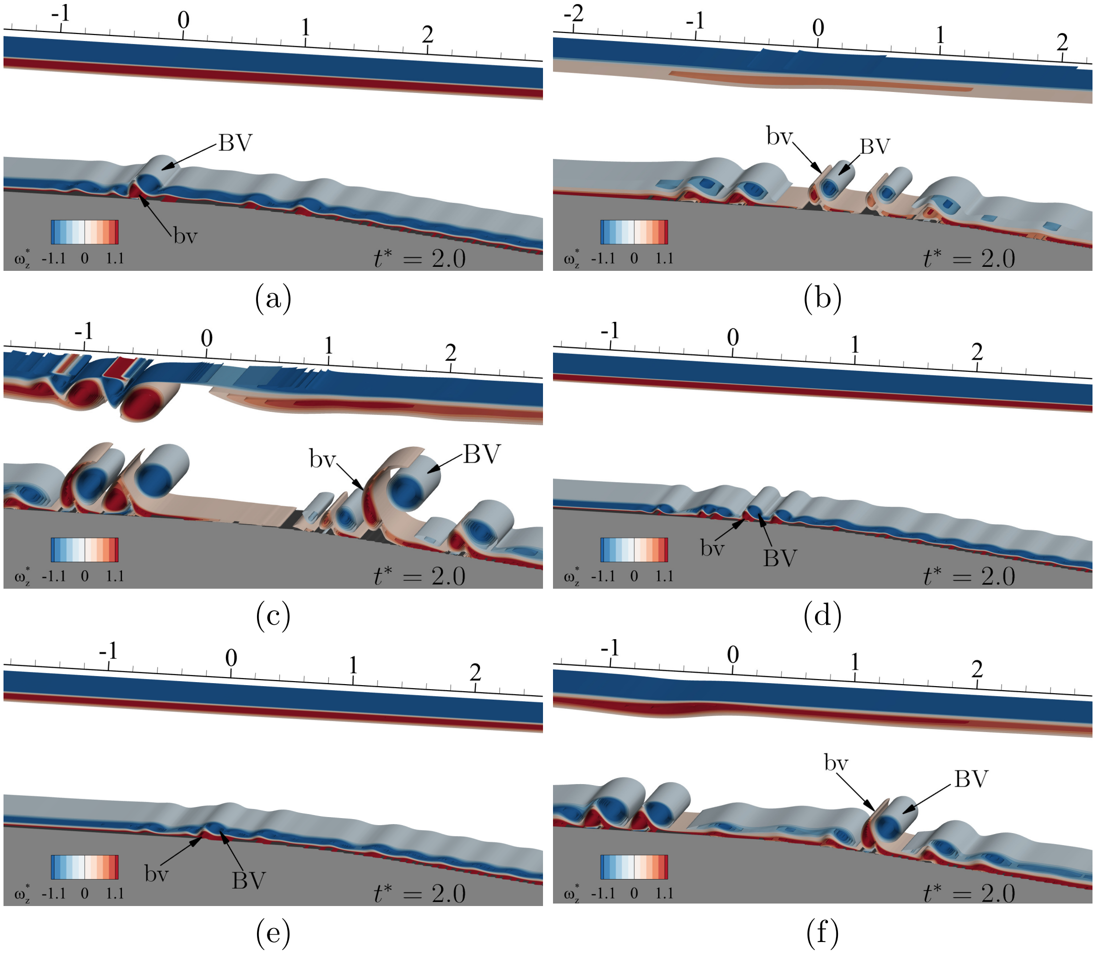

Figure 5.10: Spanwise vortex roll up in two dimensional (type I) flow evolution cases: (a) case A1, (b) case A2, (c) case A3, (d) case B1, (e) case B2, and (f) case B3.

advect upstream due to the reverse velocity in the boundary layer during the zero mean inflow phase. In high and moderate deceleration cases (cases A1 and A2), the vortex structures remain close to the bottom wall boundary (figures 5.10(a) and (b)). The induced angular velocity by the vortex pair shows to be more substantial for moderate deceleration (case A2) compared to the high deceleration case (case A1), pushing the vortex pair towards the top wall. The flow evolution in the low deceleration case (case A3) shows multiple vortex formations in the diverging and the constant channel region. The extended deceleration period leads to the development of multiple vortices, advecting upstream in later flow instances.

Flow evolution in the moderate Reynolds number cases (cases B1, B2, and B3) is qual-

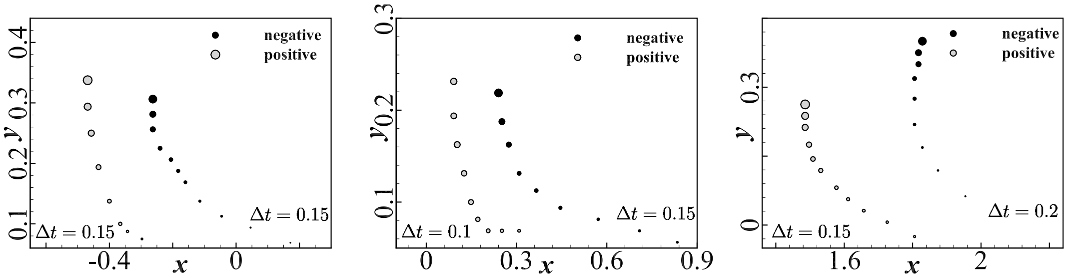

(a) (b) (c)

Figure 5.11: Temporal evolution of vortex core in advecting cases: (a) case A1 (first data point $t^* = 1.33$ and last data point $t^* = 3.833$), (b) case A2 (t^* from 1.15 to 2.4), and (c) case A3 (t^* from 1.375 to 2.8). The temporal position of the data point in the evolution window is indicated by symbol size.

itatively similar to the low Reynolds number case. Compared to low Reynolds number cases, the flow structures in moderate Reynolds number cases lie in the initial stages. Figures 5.10(d) and (e) reveal the presence of a noticeable vortex pair at $x = 0$, which is comparable to the respective deceleration cases in the low-flow Reynolds number regime. The vortex structures are well developed in the low deceleration case (case B3), similar to case A3. As shown in figure 5.10(f), vorticity rolls form in the diverging and constant channel regions. In case B3, the streamwise location of the magnified vortex structure lies in the diverging section (between $x = 1$ to 2), as in case A3. The vorticity patch in figure 5.10(f) indicates that the vortex is beginning to form over the top wall signifying a higher vortex formation on both the top and bottom walls during the dead inflow phase.

The advective nature of the vortices and their influence on the deceleration rate are quantified by tracking the vortex core trajectory. The core of the vortex is identified by minimum and maximum vorticity for primary (BV) and secondary vortices (bv), respectively. Figure 5.11 shows the temporal evolution vortex core for the primary negative vortex and the secondary positive vortex for cases A1, A2, and A3. The time-step between the data points for negative and positive vortices is distinct within each case, which is marked aside from the core positions in figure 5.11. In high deceleration events (case A1), the flow evolution happens near the end of the constant channel region (between $x = -0.4$ to 0), as shown in figure 5.11(a). Prior to being ejected into the core flow area, primary and secondary vortices developed over the bottom wall advect upstream. Increasing the deceleration period causes the vortices to develop during the deceleration phase in the downstream region. The vortex core position in figure 5.11(b) shows the advection of developed vor-

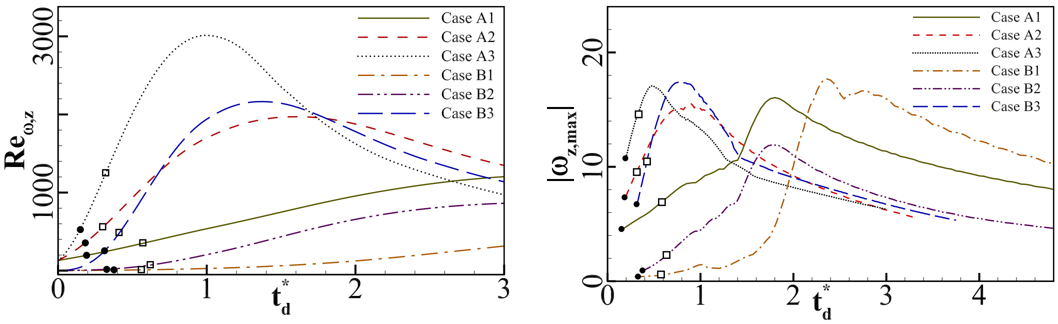

(a) (b)

Figure 5.12: Temporal evolution of (a) spanwise Reynolds number based on circulation, and (b) maximum spanwise vorticity; for advecting and decaying cases (filled circle: t_s, open square: t_v).

tices upstream during the early part of the zero mean inflow period in case A2. Vortex cores moving upward are apparent in the low deceleration case (figure 5.11(c)). Contrary to the high deceleration case, the vortex pair moves closer to the top wall and interacts with the top wall vortices in the low deceleration case.

To quantify vorticity generation, the temporal evolution of circulation-based Reynolds number is presented in figure 5.12(a). The circulation within the channel region is calculated by considering a subdomain, as shown in figure 5.1(b). This small domain can characterize both positive and negative vortex formations near the bottom wall while skipping the boundary layer vorticities and avoiding interference from the top wall structures. The stronger vortex flow features developed in the low deceleration cases (cases A3 and B3) cause an increase in circulation during the deceleration period. For high deceleration cases (cases A1 and B1), spanwise vortex roll-up is weaker compared to the low deceleration cases, resulting in a flatter circulation Reynolds number curve. As the flow stage proceeds into zero mean inflow, the primary vortex interaction over the channel surface leads to the production of positive vortices. The generation of a positive vortex roll-up and subsequent diffusion decay contribute to a decline in circulation during the zero mean inflow phase.

A quantitative analysis of the temporal evolution maximum spanwise vorticity magnitude of the primary vortex (BV) against non-dimensionalized deceleration time is provided in figure 5.12(b). Vortex formation begins towards the end of the deceleration phase in cases A1 and B1. During the zero mean inflow period, the primary vortex in cases A1 and B1 reaches its maximum vorticity within a short time, as shown in figure 5.12(b). In low and moderate deceleration cases, flow separation is achieved during the deceleration pe-

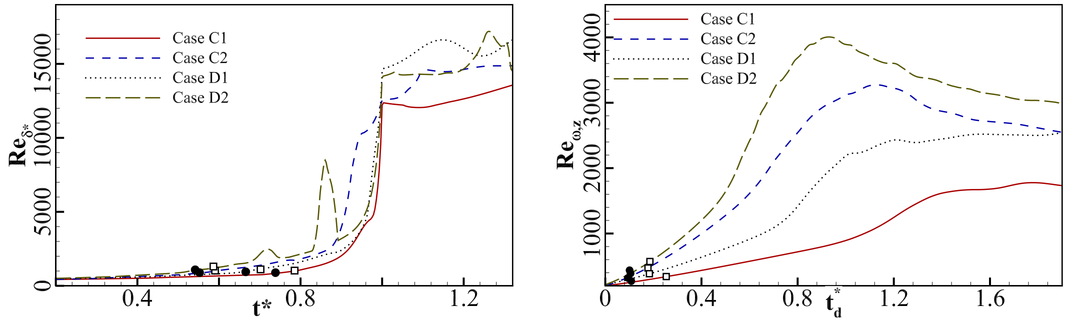

(a) (b)

Figure 5.13: Temporal evolution of (a) Reynolds number based on displacement thickness, and (b) Reynolds number based on spanwise circulation; for locally unstable cases (filled circle: t_s, open square: t_v).

riod, and the vorticity magnitude attains its maximum at the end of the deceleration phase. Unlike the high deceleration cases, low deceleration cases attain maximum vorticity magnitude during the initial deceleration phase. All cases show a steady reduction of the vorticity magnitude with an identical slope indicating the decay of vortex flow structures.

5.5 Type II: Locally evolving three-dimensional vortices

The growth of the boundary layer prior to inflectional instability is qualitatively the same in type II cases as in type I. The temporal evolution of the displacement thickness based on Reynolds number for high Reynolds number cases is depicted in figure 5.13(a). The displacement thickness increases when the boundary layer broadens due to deceleration. These cases exhibit flow separation in a Re_{δ^*} range of 840 to 1050, while vortex formation occurs in a higher range of Re_{δ^*} (970 to 1170). It is evident that displacement thickness for very high Reynolds number cases (cases D1 and D2) is much higher at the end of the deceleration phase than for high Reynolds number cases (cases C1 and C2). The generation of vortices during the zero mean inflow period leads to an erratic variation in displacement thickness. Similar to type I cases, the circulation evolution in high Reynolds number cases reaches a maximum and subsequently drops. Cases C1 and D1 with high deceleration demonstrate a sustained rise in circulation even after the deceleration phase, implying vortex development in the zero mean inflow period. Vortex generation near the end of the deceleration period results in maximum circulation in moderate deceleration cases (C2 and

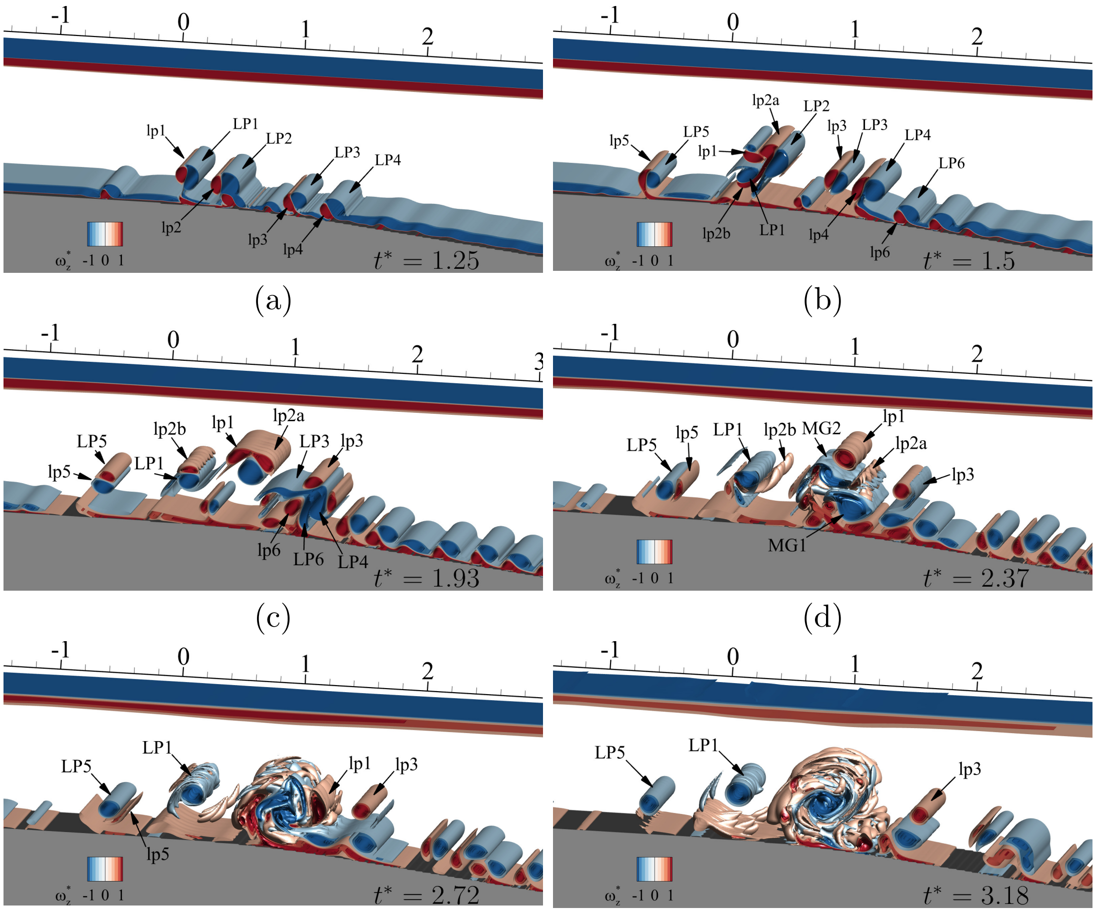

(a) (b)

(c) (d)

(e) (f)

Figure 5.14: Temporal evolution of three-dimensional flow features identified by spanwise vorticity for case C1.

D2).

5.5.1 The emergence of secondary instability and local breakdown

In high Reynolds numbers, the vortices formed by two-dimensional primary inflectional instability further undergo secondary instability, creating three-dimensional structures. Vortex flow structures developing in a high deceleration case (case C1) are revealed by the iso-surfaces of non-dimensionalized spanwise vorticity in figure 5.14. Primary inflectional instability causes the formation of negative vortices ($LP1 - LP4$), which further induces secondary positive vortices ($lp1 - lp4$) from the bottom wall boundary layer (figure 5.14(a)). This secondary vortex and the primary vortex form a pair near the wall proximity. Due to the mutual induction of the vortices, the pair detaches from the bottom wall, still pertaining to the two-dimensional nature ($t^* = 1.25$). Most flow features evolve near the initial diverging section emphasized by the non-dimensionalized streamwise scale on the top wall. The induced angular velocity of the upstream vortex pair, pair 1 ($LP1, lp1$), drives them to roll towards the vortex pair at the downstream location, pair 2 ($LP2, lp2$). Such a flow development results in stretching and splitting of the positive secondary vortex by the primary vortices ($lp2a, lp2b$ in figure 5.14(b)). The residual momentum pushes the secondary vortex ($lp1$) from the upstream pair to join the downstream couple; such a tri-vortex group further amplifies the roll-on process ($t^* = 1.93$). Inflectional profiles in the boundary layer seed multiple vortices from the boundary layer, as portrayed in figure 5.14(b) (pairs 5 and 6).

The secondary vortex structure ($lp2b$) exhibits a spanwise oscillation while orbiting around the primary vortex ($LP1$), as shown in figure 5.14(c). Similar vortex flow features are exhibited by the vortex pairs detaching from the bottom wall surfaces downstream (pairs 3 and 4). The secondary vortex ($lp4$) downstream ($x \approx 1.0$) undergoes a similar fashion of vortex splitting, creating multiple positive vortices as in the former time instances for the upstream secondary vortex ($lp2$).

The merging of the primary vortex cores ($LP4$ and $LP6$) is visible in the same instance ($t^* = 1.93$). As the flow progresses, oscillations amplify in the secondary vortex circling the primary vortex. A sandwiching effect of the merged negative vortex cores ($MG1$ and $MG2$) stretches the secondary vortices around them (figure 5.14(d)). After the stretching, spanwise oscillations disintegrate into loops around the primary spanwise vortex flow structures ($MG1$ and $MG2$). However, the initially ejected secondary vortex ($lp1$) survives the vortex interactions and shows a three-dimensional oscillation while orbiting around the primary vortex. In a later flow instance ($t^* = 2.72$) secondary vortex structure breakdown into spanwise loops around partially disintegrating primary vortices (LP1) (figure 5.14(e)). A complete transition to a turbulent structure with a negative vorticity core is observed as the flow progresses ($t^* = 3.18$). Simultaneous production of two-dimensional vortices and merging transitions are observable in the upstream and downstream positions in figure 5.14(f). Since this flow development lies in the zero mean inflow phase, advection of three-dimensional roll-ups is not evidenced for case C1, and flow features are confined to a small area near the initial diverging section (x = 0.4 to 1.5). For case C1, flow evolution over the top wall has not yet been developed at $t^* = 3.18$. Induction from the bottom wall vortices creates a positive vorticity patch over the top wall at $t^* = 3.18$, indicating vortex roll-up in later flow time.

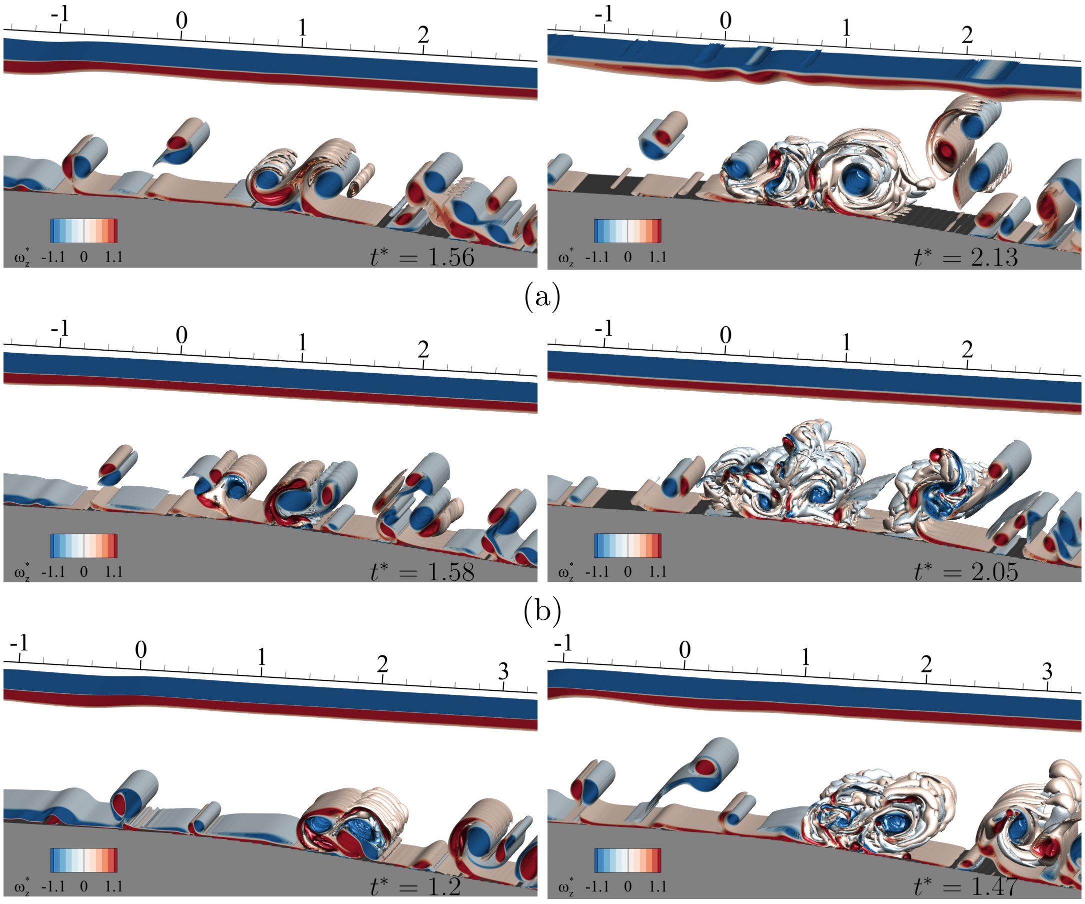

(a)

(b)

(c)

Figure 5.15: Temporal evolution of three-dimensional flow features identified by spanwise vorticity for cases belonging to type II instability: (a) case C2, (b) case D1, and (c) case D2.

The temporal evolution of flow vortices in cases similar to case C1 (Type II) is evidenced in figure 5.15. Vortex flow structures at two flow instances are shown in the figure; the first flow instance portrays the three-dimensional oscillations during the early transition phase, while the second instance illustrates the flow structures in the turbulent phase. Identical to case C1, primary instability in the deceleration phase develops into vortex pair, which moves downstream and interacts with similar vortex pairs. Figure 5.15(a) indicates the formation of spanwise oscillations over the secondary vortices in case C2. Stretching of the secondary vortex around the primary vortex is evidenced at $t^* = 2.0$. Along with three-dimensional disintegration, vortex pairs eject into the flow core at a downstream position due to the induced velocity. As flow progresses, analogous to case C1, the formation of a turbulent three-dimensional structure with negative spanwise vorticity is illustrated in figure 5.15(a). Unlike case C1, the formation of top-wall vortices is evidenced for case C2 as depicted in figure 5.15(a). During the zero mean inflow phase at $t^* = 2.13$, the ejected vortex pair interacts with the top wall boundary layer. Figures 5.15(b) and (c) show identical flow evolution for cases D1 and D2. Three-dimensional disintegration initiates with vortex pair interaction resulting in a locally turbulent region. The turbulent region develops earlier for high Reynolds number cases (D1 and D2) than in high flow Reynolds number cases (C1 and C2). A common route of transition mechanism in the vortex structures is closely related to the vortex pair interactions during the zero mean inflow region. Given its universal nature, the discussion will be further elaborated upon in the subsequent chapter.

5.6 Type III: Spatially unstable flow evolution

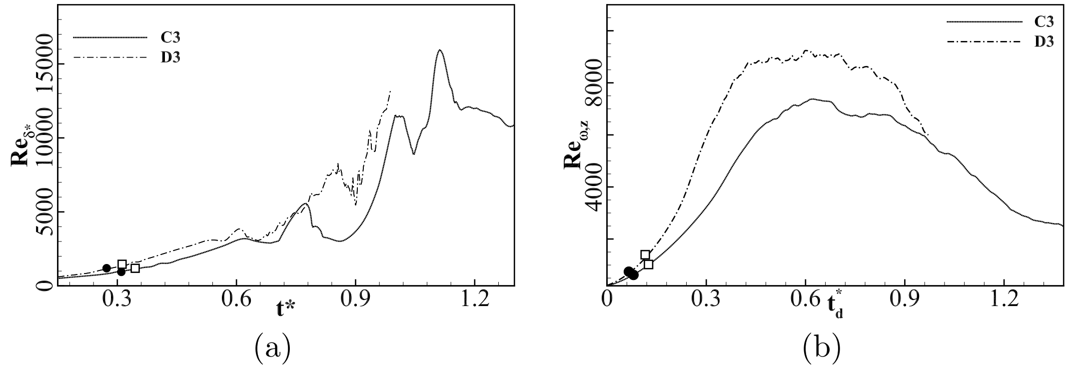

Figure 5.16: Temporal evolution of (a) Reynolds number based on displacement thickness, and (b) Reynolds number based on spanwise circulation; for spatially unstable cases (filled circle: t_s, open square: t_v).

Three-dimensional disintegration of vortex flow features results in complex boundary layer growth in spatially unstable cases (figure 5.16(a)). In both cases, Re_{δ^*} evolution initiates with a low value during the acceleration phase. The flow separation for cases C3 and D3 lies at Re_{δ^*} of 980 and 1133, respectively, which are highest compared to the former categories. Similarly, vortex formation initiates in case C3 at a Re_{δ^*} = 1092, whereas in case D3 at a Re_{δ^*} = 1300. Unlike in other cases, flow generates vortex roll-up during the initial deceleration stage, reflected by an increase in displacement thickness. As the vortex clears, the profile returns to its typical profile, lowering the displacement thickness. The peaks of the displacement thickness variation indicate further vortex development. The three-dimensional vortex breakdown in both cases produces high-frequency oscillations during the flow advancement. Three-dimensional disintegration initiates quicker for case D3 (around $t^* = 0.7$) due to the higher streamwise velocity than case C3. Alternatively, case C3 displays three-dimensional turbulent behavior towards the end of the deceleration phase (around $t^* = 0.9$).

Oscillations in the temporal variation of the Reynolds number based on spanwise circulation indicate a transition from a two-dimensional to a three-dimensional flow regime (figure 5.16(b)). Cases C3 and D3 display an increment in circulation during the acceleration and constant velocity phases, identical to A3 and B3. Compared to the previous categories, during the deceleration phase, the circulation-based Reynolds number reaches a higher magnitude for these cases (cases C3 and D3), indicating higher vortex formation. Minute spanwise loop formation due to three-dimensional disintegration induces oscillations in circulation development during the deceleration phase. The earlier onset of fluctuations characterizes the rapid disintegration of flow structures in case D3 compared to case C3. The circulation decays during the zero mean inflow phase with a higher decay rate compared to type I cases.

5.6.1 Unsteady separation and flow breakdown

Vortex flow structures identified by the non-dimensional spanwise vorticity in case C3 are portrayed in figure 5.17. Shear layer roll-ups marked by BS1 - BS5 are observed at nearly equally spaced locations over the diverging section. Vortex flow structures are highlighted according to their formation sequence during flow evolution. Due to unsteady flow separation, vortices develop over the initial diverging section (PS1) during deceleration. Vortices evolving over the diverging section advect downstream, creating additional positive vortices (bs1) from the wall surface ($t^* = 0.55$). Persistent streamwise velocity deceleration leads to a continuous shedding of vortices from the initial diverging section (PS1 and PS2). A higher advective velocity of the upstream vortex leads to the pairing of the vortex roll-ups (BS1 and BS3) ($t^* = 0.63$). Due to mutual induction, positive vortices (ps1a - ps1c) eject from the bottom wall vorticity layer and revolve around the primary vortex (PS1) while advecting downstream ($t^* = 0.69$). In such advecting vortex pairs, secondary vortices generate spanwise oscillations (ps1c) similar to locally unstable cases (type II). The formation of three-dimensional oscillations attributes to the local interaction of advecting pairs. Simultaneous merging of vortex flow features (BS2 and BS4) and the three-dimensional disintegration of secondary vortices (ps1c, ps2a, and ps2b) are evident in later deceleration

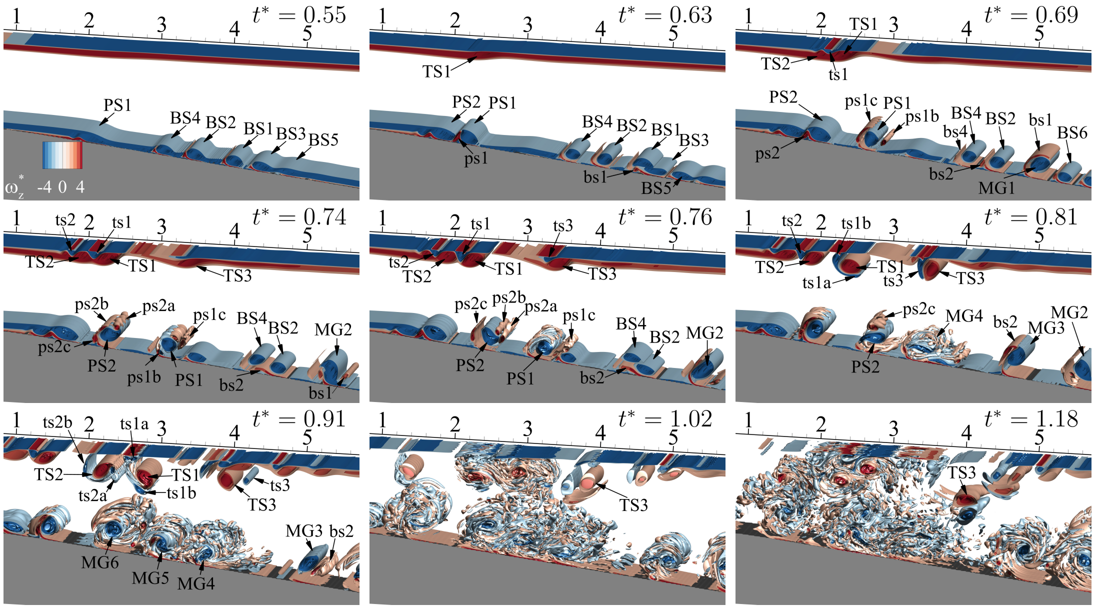

Figure 5.17: Temporal evolution of three-dimensional flow features identified by non-dimensional spanwise vorticity for case C3.

flow instances ($t^* = 0.74$ and 0.76).

A complex structure with multiple small-scale vortices is formed due to the growth of the three-dimensional oscillations into tube-like structures (MG4), which displaces downstream due to the streamwise velocity ($t^* = 0.81$). Three-dimensional oscillations develop over the unsteady separation vortices when the flow passes half of the deceleration phase. A vortex pair discharging from the initial diverging section displays three-dimensional oscillation after the ejection ($t^* = 0.91$). Advecting vortex roll-ups interact with other flow features, generating a turbulent flow structure ($t^* = 0.91$). The decay of streamwise velocity further results in flow detachment, leading to a turbulent flow evolution during the zero mean inflow phase. Analogous to the former category, the flow features move backward as the flow progresses in the zero mean inflow region. Tiny loop structures are formed through the disintegration of vortex flow structures at later flow instances ($t^* = 1.18$).

Identical to the bottom wall, the top wall boundary layer displays vortex roll-ups and three-dimensional disintegration, as presented in figure 5.17. An extended stay of the bottom wall vortex in the initial diverging section induces the flow to separate from the top wall leading to vortex roll-up. The top wall boundary layer broadens over the bottom separation region once the flow separates over the bottom wall ($t^* = 0.55$). In type III cases, flow separation occurs earlier in the deceleration phase, forcing the fluid over the top wall.

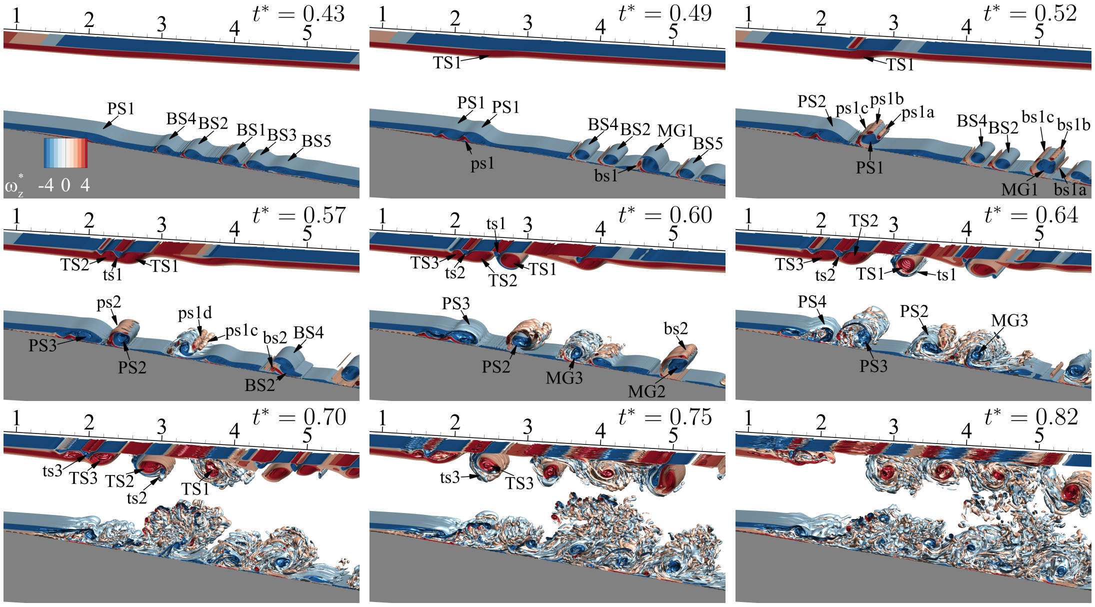

Figure 5.18: Temporal evolution of three-dimensional flow features identified by non-dimensional spanwise vorticity for case D3.

The formation of a primary positive top wall vortex (TS1) subsequently results in the production of a negative secondary vortex (ts1) ($t^* = 0.69$). The shedding of vortices due to unsteady separation promotes the development of flow structures (TS pairs 2 and 3) across the top wall ($t^* = 0.74$). The top wall vortices retain their two-dimensional traits while the bottom wall vortex pair undergoes three-dimensional disintegration at $t^* = 0.76$. Due to induced rotation, primary and secondary top wall vortices eject from the top wall boundary layer ($t^* = 0.81$). Analogous bottom wall-flow features, top wall vortices clearly show the pairing behavior at $t^* = 0.91$ (TS3). Toward the end of the deceleration phase, the top wall formations also generate three-dimensional oscillations. In the initial zero mean inflow phase, the interaction between the top and bottom wall structures is minimal ($t^* = 1.02$), while at a later flow instance ($t^* = 1.18$), the mixing of flow features over the top and bottom walls results in a turbulent flow evolution.

Similar to case C3, vortex evolution in case D3 demonstrates vortex generation and three-dimensional breakdown of flow characteristics during the deceleration phase (figure 5.18). The inflectional instability in the boundary layer develops into vortex roll-ups (BS1 - BS5) during the deceleration phase ($t^* = 0.43$ and 0.49). Compared to case C3, a higher mean inflow velocity results in a higher advective velocity for the flow features along with the vortex shedding (PS pairs) due to unsteady separation ($t^* = 0.52$). Three-dimensional oscillations induced over the secondary vortices amplify and disintegrate at subsequent flow instances as vortex pairs are ejected from the initial diverging section. In the case of D3, the vortex flow patterns disintegrate at an early pulse stage, resulting in an advecting turbulent structure that stays closer to the bottom wall ($t^* = 0.6, 0.64$). Unlike case C3, the top wall vortices (TS pairs $1, 2$) advect downstream along with the bottom wall structures due to the earlier inception of top wall structures. Flow formations over the top wall retain their two-dimensional nature at this flow instance ($t^* = 0.64$). As the flow forwards through the deceleration phase, the advecting top wall vortices (TS1, TS2) evidence three-dimensional disintegration ($t^* = 0.7$). The turbulent flow features over the top and bottom wall advect downstream as flow forwards, while the interaction of the structures results in a turbulent flow as evidenced at $t^* = 0.75$ and $t^* = 0.82$.

5.7 Summary

In this chapter, we examine the emergence of turbulence in a diverging channel under APG boundary layer conditions by imposing the analytical solution of trapezoidal mean flow condition comparable to the experiments of Das et al. [2]. The effects of flow Reynolds numbers and deceleration Reynolds numbers are systematically investigated by varying the flow velocity and deceleration rate. The flow transition initiates with the thickening of the boundary layer followed by two-dimensional primary inflectional instability, which generally occurs in the deceleration phase and subsequently leads to flow separation and shear layer roll-up in the diverging section. Top-wall boundary layers also exhibit inflectional instability, resulting in vortex roll-ups identical to the bottom wall in later flow instances. At low and medium Reynolds numbers, shear layer vortices remain two-dimensional, while secondary instabilities initiate the formation of three-dimensional structures at high Reynolds numbers. Based on the critical flow time flow associated with the initiation of secondary instability and temporally averaged streamwise vorticity, we have classified the flow evolution into three categories.

The first category (type I) occurs in low and moderate Reynolds number cases, which exhibit two-dimensional flow evolution of vortex flow structures that advect and diffuse during the zero mean inflow phase. The boundary layer growth occurs rapidly at high deceleration rates, whereas the increase is gradual at low deceleration rates. However, the time of flow separation and the vortex formation depends on the local Reynolds number based on the displacement thickness ($Re^*_\delta \approx$ 600 and 700, respectively). The emergence of the primary vortices leads to a progressive increase in circulation in the initial stage;

after reaching a maximum during deceleration, the total circulation in the diverging section declines as the wall vortices diminish and spanwise vorticity decreases. The vortex structures maintain their two-dimensional nature during the zero inflow phase, whereas the individual vorticity magnitude of primary vortices decreases by the vortex decay.

In the second category (type II), a locally turbulent flow structure is evolved during the zero mean inflow phase ($t^*_{3D} > 1$) by the amplification of the spanwise oscillation induced over the secondary vortex ejecting from the bottom wall. Similar to the former category, the boundary layer grows temporally, and higher inflow velocity in these cases leads to higher Reynolds numbers based on displacement thickness for flow separation ($Re^*_\delta \approx 940$) and vortex formation ($Re^*_\delta \approx 1070$). Spanwise vortex structures reveal that initial spanwise oscillations developed over the secondary vortices due to the straining by the primary vortex amplified with flow time, creating a locally complex structure during zero mean inflow.

The third category (type III) is characterized by low deceleration and high inflow velocity, which result in multiple shear layer roll-ups over the diverging section and vortex shedding due to unsteady separation from the initial diverging section during deceleration phase ($t^*_{3D} < 1$). Identical to elliptic instability formation in the previous category, the three-dimensional visualizations of the spanwise vorticity indicate an oscillating secondary vortex in the vortex pair ejected from the initial diverging section during the deceleration phase. Low deceleration induces a higher advective velocity for flow structures, causing the spanwise vorticity roll-ups to pair over the diverging section, similar to the pairing of co-rotating vortices as described in Rogers and Moser [95]. A separation bubble, comprising spanwise vorticity rolls with opposite sense of rotations developed due to unsteady separation, disintegrates at the end of the deceleration phase and compares well with the observations of Wissink and Rodi [38].

Chapter 6

Secondary instability aspects in a diverging channel

6.1 Introduction

Unlike highly rich vortex structures inducing multiple three-dimensional instability spots in a bluff body wake, flow in a diverging channel is highly dependent on the temporal parameters. Due to its low spatial gradient, the flow evolves around the initial diverging section, which offers the maximum pressure gradient inducing the vortex formation during the deceleration period. As discussed in the previous chapter, the secondary instability evolution of the vortex pair is altered with flow velocity and deceleration parameters and classified into three categories.

The three-dimensional transition of the vortex flow features developed in a decelerating diverging channel holds many similarities with flow evolution in vortex-dominated flow fields. Though the vortex flow structures evolve during the deceleration phase in low inflow velocities, since the flow field resists the growth of spanwise oscillation, the vortices diffuse in the zero mean inflow phase. While for high inflow velocity cases, the flow field is susceptible to spanwise oscillation and further disintegration of spanwise structures. Also, the three-dimensional flow features alter with changes in the deceleration parameters. A combination of high velocity with low deceleration causes an unsteady separation inducing periodic flow structures shedding downstream.

A comprehensive evaluation of the secondary instability nature in different flow conditions is provided in this chapter. Vortex flow features are further investigated to identify the spatial instability nature. Similar to other vortex-dominated flow evolution, the spatial characteristics of the three-dimensional transition depend on the spanwise variation of the streamwise vorticity. By employing both theoretical and numerical methods, the spatial and temporal nature of the instability mechanism is analyzed. An in-depth characterization of the instability mechanism is provided in the chapter. Also, the shedding characteristics in low deceleration cases are investigated through dynamic mode decomposition and spectra analysis of probe data.

The current chapter aims to present a detailed discussion on underlying three-dimensional coherent flow features in flow evolution and their stability characteristics through theoretical and numerical methods. In section 6.2, the growth of three-dimensional oscillation is corroborated by the spanwise velocity component evolution in both type II and type III cases. Further in section 6.3, the structure of the three-dimensional oscillation in type II cases is identified through the λ_2 method. In addition, the section also consolidates the spatial and temporal characteristics of secondary instability investigated using DMD and theoretical growth rate estimations. In section 6.4, velocity spectra and DMD analyses are presented to understand unsteady separation in type III cases. As a final summary, section 6.5 concludes the observations on the secondary instability features observed in a diverging channel under different deceleration rates.

6.2 Growth of three-dimensional oscillations

The development of the three-dimensional oscillations in the flow field is closely associated with the spanwise velocity component evolution. The contours of non-dimensional RMS spanwise velocity component ($w^*_{rms} = \frac{w_{rms}}{U_p}$) for all three-dimensional cases are provided in the figure 6.1. The RMS of the spanwise velocity component is calculated using a similar expression of u_{rms} given by equations 5.8 and 5.9. The evolution of the spanwise component shows a relatively high magnitude near the three-dimensional unstable region, identical to the non-dimensional mean streamwise vorticity (figure 5.8). The peak fluctuations in the spanwise velocity component spread around the separation bubble for type II cases, indicating a local evolution of the three-dimensional oscillation. Due to the advection of the flow structures during the deceleration period, the intensity of the spanwise fluctuations is higher in spatially unstable cases (type III). In such cases (cases C3 and D3), advection and later disintegration lead to a spread of the fluctuation intensity over the domain, as shown in figure 6.1. Identical to streamwise vorticity contour, spanwise fluctuations are also present over the top wall for type III cases.

In the present simulation, the source of perturbations is limited to the two-dimensional fluctuations associated with the analytical solution, which are imposed at the inlet of the domain and the unavoidable numerical error related to the numerical scheme. As shown

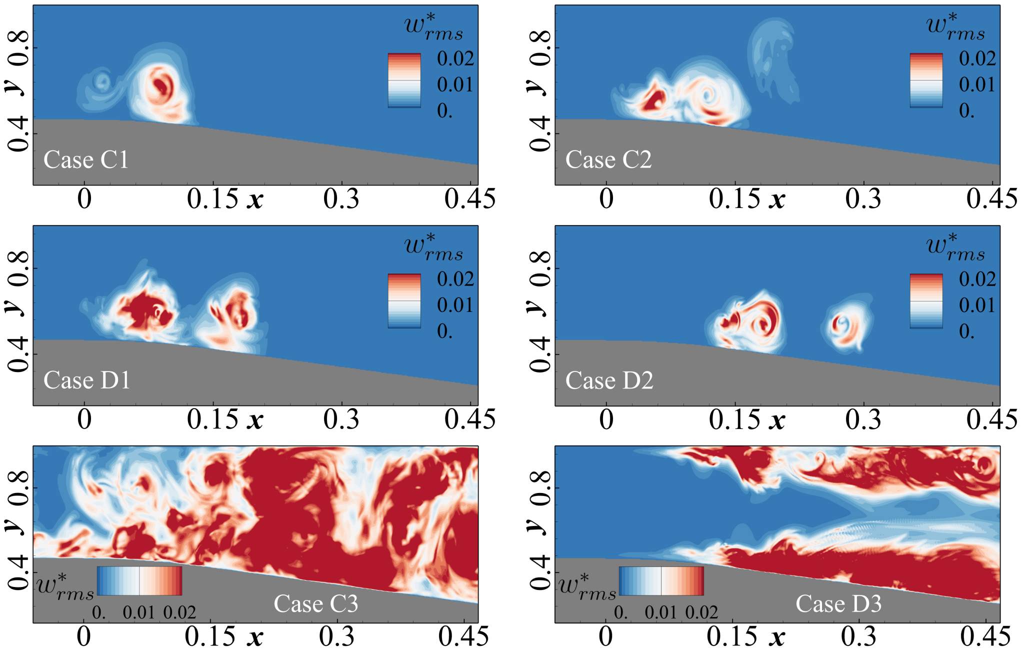

Figure 6.1: RMS of fluctuations in the spanwise velocity component in three-dimensional cases.

from the simulation, these values are of the order of 10^{-6}. In figure 6.2, the evolution of the amplitude of the spanwise fluctuations $\left((w')^2 = \frac{(w-w_{mean})^2}{U_p^2}\right)$ is plotted for locally three-dimensional cases. The probe location is selected as the maximum spanwise velocity component average position.

For all cases, the non-dimensional spanwise fluctuation amplitude increases during the dead inflow region, indicating the three-dimensional disintegration process. Oscillation amplitudes reach high magnitudes for very high Reynolds cases (cases D1 and D2) and are near 0.01, whereas they peak at around 0.005 for high Reynolds cases. Also, the spanwise velocity component growth is affected by the deceleration period. While low deceleration cases (case C1 and case D1) achieve their peak amplitudes later after the pulse ends, moderate deceleration cases (case C2 and case D2) attain their peak amplitudes earlier. The highest amplitude is observed in case D2, with a sharp increase in the oscillation amplitude.

6.3 Three-dimensional flow structures

Similar to the previous analysis, the topology of three-dimensional oscillation developed over the vortex structures in the diverging channel is identified using the λ_2 method and

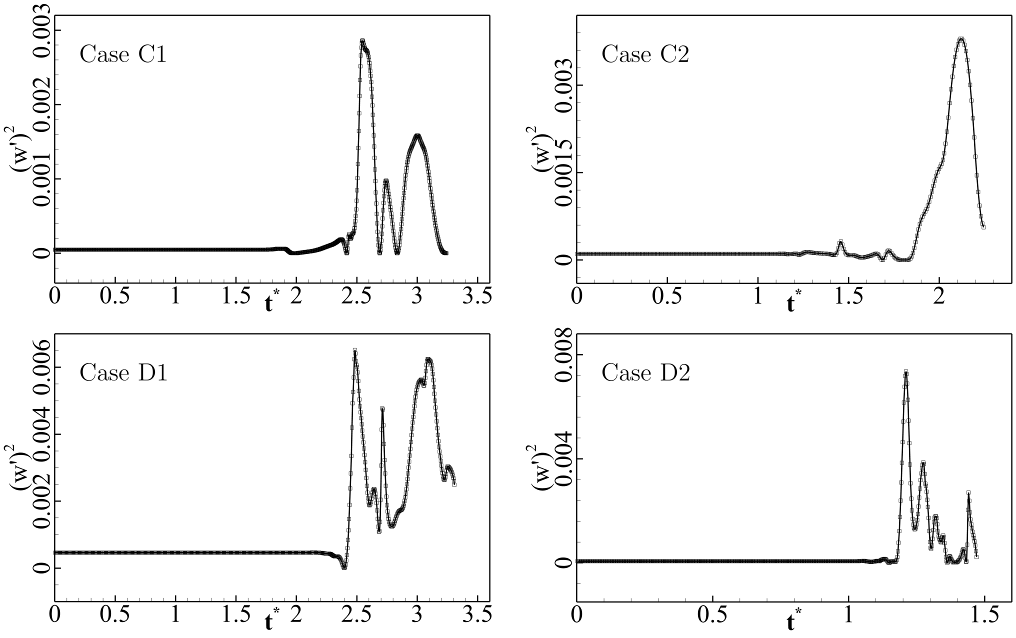

Figure 6.2: Growth of the spanwise velocity component fluctuation in type II cases. The probe location is selected as the position of maxima of the spanwise velocity component average.

contoured by non-dimensional streamwise vorticity in figure 6.3. The spanwise oscillation developed over the secondary vortex for case C1 at $t^* = 1.93$ is illustrated in figure 6.3. The alternate streamwise vorticity originated over the spanwise vortex roll-ups displays a symmetrical pattern. A cross-section (Y-Z) through the central plane of vortex pairs ($x = 0.308$) is taken to understand the nature of oscillations. Non-dimensionalized spanwise vorticity contoured snapshots (figure 6.3(b)) provide a clear visual of secondary vortex developing oscillations. The presence of alternating streamwise vorticity is further explained by superimposing the vector plot in figure 6.3(c). Circulation regions are discernible over the spanwise vortex roll-ups, as seen in the inset figure in the subfigure.

6.3.1 Spatial structure of coherent flow features

DMD algorithm is used to analyze secondary instability over the shear layer vortices resulting from primary inflectional instability. Dynamic mode decomposition identifies the underlying dynamics of the coherent flow features developed during the flow evolution. We use the snapshot-based approach introduced by Schmid [29] to identify the secondary instability features along with their temporal dynamics.

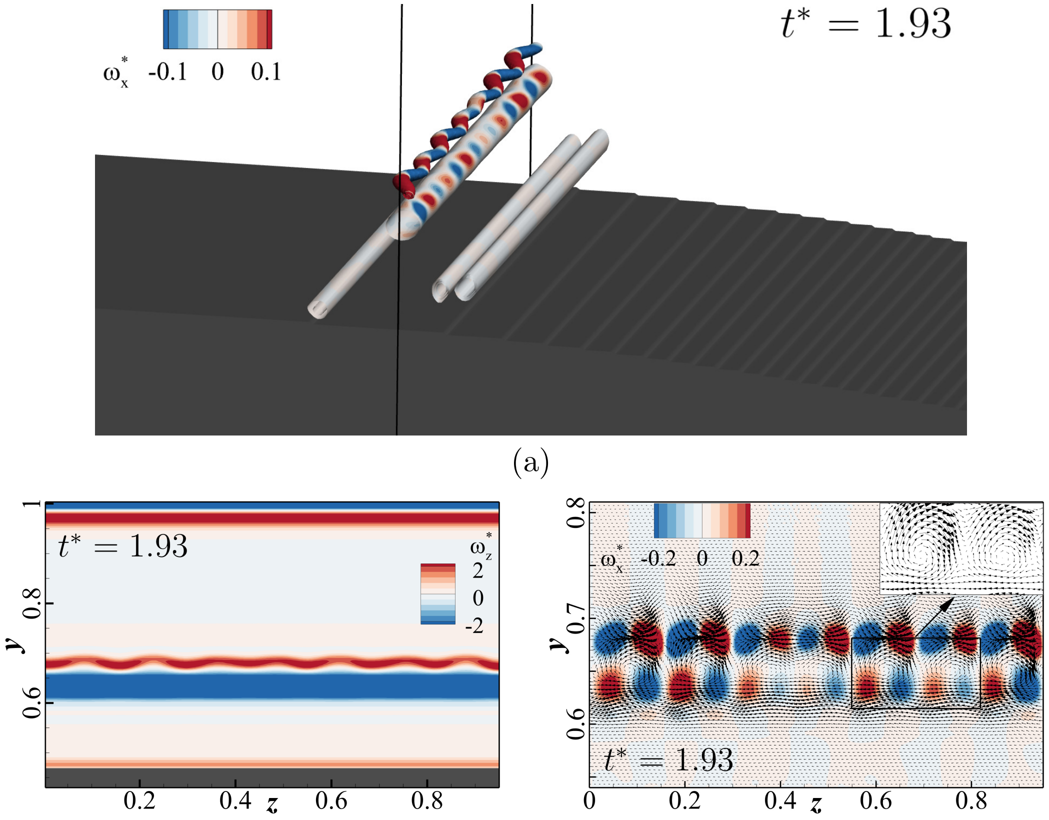

(a)

(b)

(c)

Figure 6.3: (a) Flow features identified ($LP1$ and $lp2b$) using λ_2 method contoured by streamwise vorticity ($\lambda_2 = -1$), (b) section through the spanwise oscillation contoured by spanwise vorticity ($x = 0.29$), and (c) section through the spanwise oscillation contoured by streamwise vorticity.

Through a three-dimensional dynamic mode decomposition of streamwise vorticity data, the most unstable flow features associated with secondary instabilities are identified (figure 6.4). For the DMD calculation, three-dimensional snapshots are taken with a time step of $\Delta\tau \;=\; 0.05$ s between each snapshot. The Ritz circle obtained from the dynamic mode decomposition for cases belonging to the second category is presented in figure 6.4(a). The position of the mode with respect to the unit circle outlined in the figure indicates the stability of the modes. In general, a mode lying outside a circle indicates an unstable mode, while lying within signifies a stable mode; and when it lies on a circle, it is neutrally stable. In all cases, at least one mode displays an unstable trait, illustrated by the circle in figure 6.4(a). Figure 6.4(b) shows the growth rate and frequency distribution for the DMD modes. The highest growth rate mode obtained from DMD analysis is indicated

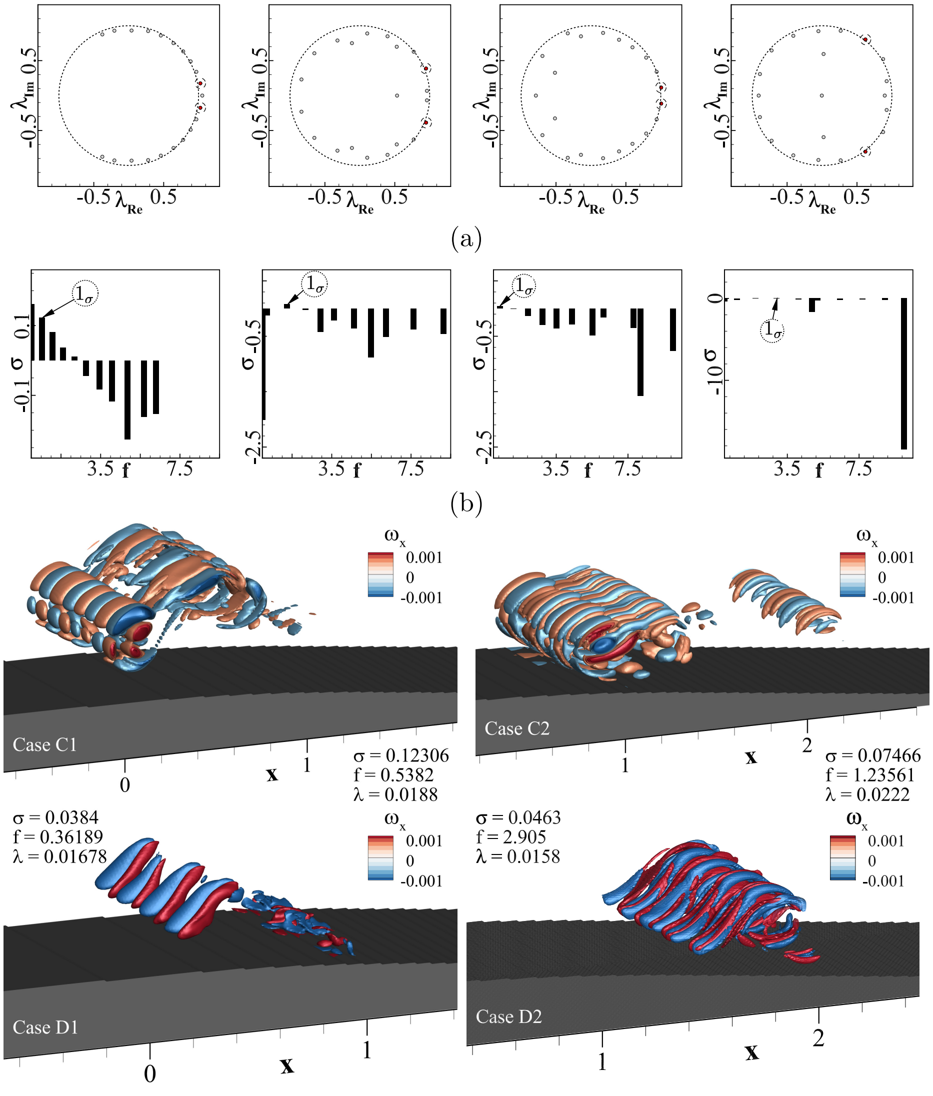

(a)

(b)

(c)

Figure 6.4: Three-dimensional DMD analysis results: (a) Ritz Circle, (b) growth rate vs. frequency, and (c) leading secondary instability modes based on growth rate criterion for type II cases.

Case	b (m)	λ_{mean}/b	λ_{DMD}/b	a_1 (m)	a_2 (m)	Γ_1 (s^{-1})	Γ_2 (s^{-1})	b_{LO} (m)
C1	0.0128	1.56	1.69	0.025	0.0040	0.00049	-0.00195	0.0111
C2	0.0125	3.34	3.26	0.0018	0.0045	0.00062	-0.0037	0.0068
D1	0.0100	2.12	1.91	0.0019	0.0040	0.00113	-0.0038	0.0088
D2	0.0095	2.25	2.11	0.0015	0.0055	0.00051	-0.0070	0.0075

Table 6.1: Spanwise wavelength comparison and parameters for Lamb-Oseen approximation.

by 1_σ.

When streamwise vortex growth is unstable, vortex roll-ups will experience three-dimensional destabilization, as manifested by the positive growth rates for all cases. The mode with the maximum growth rate for all cases, as shown in figure 6.4. The three-dimensional morphology of unstable modes is visualized using an iso-surface of streamwise vorticity. A spanwise variation of the streamwise vorticity is evidenced in all cases. The spanwise wavelength obtained for the mode with the highest growth rate is provided in table 6.1. Averaging the distance between the peaks of the streamwise vorticity plotted across the vortex core provides the mean spanwise wavelength. The average spanwise wavelength observed for all three-dimensional cases is tabulated in table 6.1. Both wavelengths are non-dimensionalized by the distance between the cores of vortex pairs (b: distance between maximum and minimum vorticity magnitudes). The spanwise wavelength for the coherent flow features identified by DMD analysis (λ_{DMD}) lies close to the mean spanwise wavelength determined from streamwise vorticity variation over the oscillation (λ_{mean}).

6.3.2 Theoretical growth rate prediction

Various theoretical models are used to measure the growth rate of vortices associated with secondary instabilities. Rankine vortices and Lamb-Oseen vortex pairs are generally used to approximate vorticity distributions for estimating the theoretical growth rates of primary vortices [96]. Furthermore, Le Dizes [97] developed a growth rate relation by neglecting the viscous effects for a multipolar vortex in a rotating flow field, with estimates comparable to the global instability analysis results for various vorticity distributions such as Kirchoff [98] and Moore and Saffman [99] vortices. A consolidated review of Kerswell [100] discusses in detail the emergence of elliptical instability in different flow scenarios.

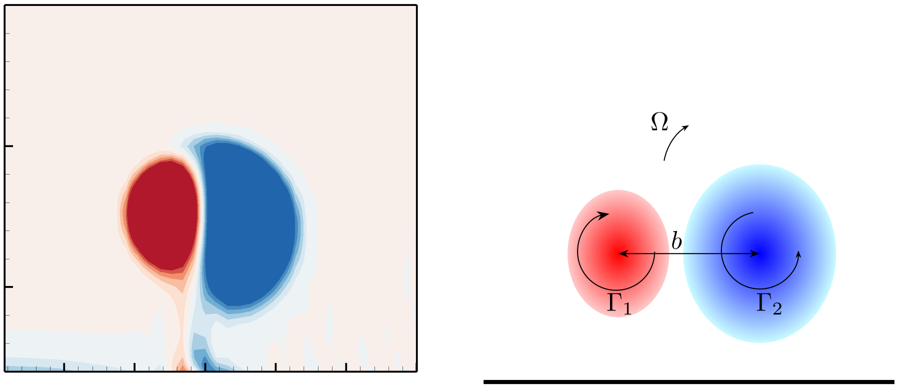

(a) (b)

Figure 6.5: Depiction of Lamb-Oseen model: (a) simulation and (b) Lamb-Oseen model.

An extended investigation by Le Dizes and Laporte [93] identifies a relation to predicting the elliptic instability growth rate in a vortex pair and establishes a critical region for the Reynolds number based on the circulation. A recent review on the instabilities arising in a vortex pair by Leweke et al. [94] proposes a revised estimation of the growth rate for elliptic instability.

The secondary instabilities formed during the zero-mean phase in the diverging channel are similar to the short-wavelength elliptic instability demonstrated by Laporte and Corjon [101]. Since multiple vortex pairs are observed near the bottom wall, unlike classical short wavelength vortex instability, theoretical stability analysis is performed for most magnified vortex pairs. Variation of the spanwise vorticity in a vortex pair ejecting from the bottom wall is shown in figure 6.5(a). An identical depiction of an approximated Lamb-Oseen pair obtained from the relation 6.1 is given in figure 6.5(b). The vorticity distribution for such a vortex pair with circulations Γ_1 and Γ_2 may be approximated using the Lamb-Oseen equation [94], which is presented below:

$$\omega_z = \frac{\Gamma_1}{\pi a_1^2} \exp\left(-\frac{r^2}{a_1^2}\right) + \frac{\Gamma_2}{\pi a_2^2} \exp\left(-\frac{r^2}{a_2^2}\right). \tag{6.1}$$

where r represents the distance from the vortex core position. The core radius (a_1 and a_2)

for a vortex centered at $\mathbf{X}^c$ is obtained from the relations 6.2 and 6.3.

$$(x_{c_1}, y_{c_1}) = \left(\frac{1}{\Gamma_1} \int_{D_1} x\,\omega_z, \quad \frac{1}{\Gamma_1} \int_{D_1} y\,\omega_z \right), \tag{6.2}$$

$$a_1^2 = \frac{1}{\Gamma} \int_{D_1} |\mathbf{X} - \mathbf{X}^c|^2 \omega_z dS. \tag{6.3}$$

Where D_1 represents the domain containing each vortex, ω_z defines the spanwise vorticity, and dS represents the infinitesimal area.

Le Dizes and Laporte [93] proposed an explicit relation using approximate linear expressions for the internal strain ratio (s_r) and inertial wave vector inclination for predicting the growth rate of an elliptic instability in a counter-rotating vortex pair. Leweke et al. [94], in their review, presented a revised linear fit to determine the frequencies (ω) and damping rates (ζ) of the first two Kelvin modes. The growth rate for the first two modes of elliptic instability in a Lamb-Oseen vortex pair is given by:

$$\sigma_1^{*,(n)} = \sqrt{\left(\frac{3}{4} - \frac{\overline{\Omega}_1}{4}\right)^4 s_r^2\left(\overline{\Omega}_1\right) \left(\frac{\Gamma_2}{\Gamma_1}\right)^2 - \left(\omega^{(n)} - \overline{\Omega}_1\right)^2 \left(\frac{b}{a_1}\right)^4} - \left(\frac{b}{a_1}\right)^2 \left(\frac{\zeta^{(n)}}{Re_{\Gamma_1}}\right). \tag{6.4}$$

The superscript n represents the mode number, and the subscript denotes the vortex number. Here the growth rate of the mode is non-dimensionalized by the time scale of translational motion $\left(\frac{2\,\pi\,b^2}{\Gamma_1}\right)$. Linear expressions for real (ω) and imaginary (ζ) parts of the complex frequency in equation 6.4 are as follows:

$$\overline{\Omega}_1 = \left(\frac{a_1}{b}\right)^2 \left(\frac{\Gamma_1 + \Gamma_2}{\Gamma_1}\right), \tag{6.5a}$$

$$s_r(\overline{\Omega}) = 1.5 + 0.1323\big(0.32 - \overline{\Omega}\big)^{-9/5}, \tag{6.5b}$$

$$\omega^{(1)} = -0.135\big(ka_1 - 2.26\big), \tag{6.5c}$$

$$\omega^{(2)} = -0.084\big(ka_1 - 3.95\big), \tag{6.5d}$$

$$\zeta^{(1)} = 74.02 + 64.15\big(ka_1 - 2.26\big), \tag{6.5e}$$

$$\zeta^{(2)} = 229.6 + 104.3\big(ka_1 - 3.95\big). \tag{6.5f}$$

The growth rate of elliptical instability for a counter-rotating vortex pair ejected from the bottom boundary of the wall in the diverging channel is determined using equation 6.4.

To ascertain the validity of the Lamb-Oseen approximation, the plot of the spanwise vorticity obtained from the equation 6.1 is compared with the simulation results (through the vorticity cores). Table 6.1 provides the essential parameters obtained from simulation

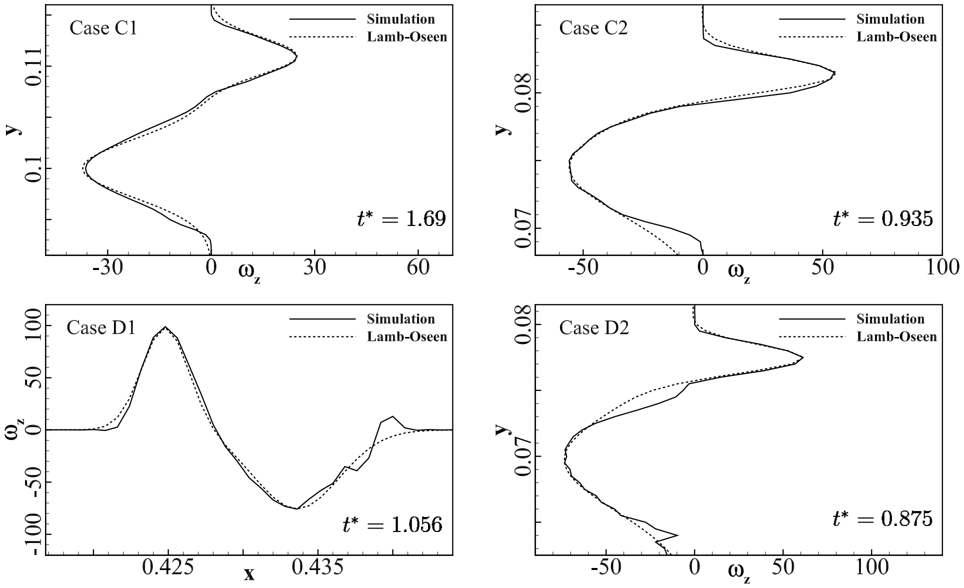

Figure 6.6: Lamb-Oseen model comparison for vortex pair in locally unstable.

used to estimate the Lamb-Oseen approximation for locally unstable cases (type II) as depicted in figure 6.6(c). Here, the b_{LO} denotes the distance between the first positive vortex core and the second negative vortex in approximated vorticity distribution. In cases, C1, C2, and D2, a vertical pair of vortices is compared with vertical Lamb-Oseen pair. While in case D1, a better approximation is obtained for a horizontal pair and is compared to a similar Lamb-Oseen approximation (figure 6.6(c)). As presented in figure 6.6, the assumption of a Lamb-Oseen vortex approximation remains true in all selected flow instances.

Using equation 6.4, the growth rate of elliptical instability for a counter-rotating vortex pair ejected from the bottom boundary of the wall was determined. The growth rate curves obtained for different spanwise wave numbers for secondary vortices are presented in figure 6.7. A similar analysis was conducted on the vortex structures in type I cases. Secondary vortices developed in advecting and diffusing two-dimensional cases indicate stable growth rate curves and are, therefore, not included. The growth rate curves are calculated for the secondary vortex, which undergoes three-dimensional disintegration (using Lamb-Oseen approximation as shown in figure 6.6(c)). The growth rate curves indicate an unstable first mode alongside a stable second mode (figure 6.7(a)). An identical growth rate curve is obtained for case D1 (figure 6.7(b)), revealing the formation of first-mode elliptic instability in high deceleration cases (cases C1 and D1). Unlike high deceleration cases, both the first and second modes show an unstable nature in moderate deceleration cases

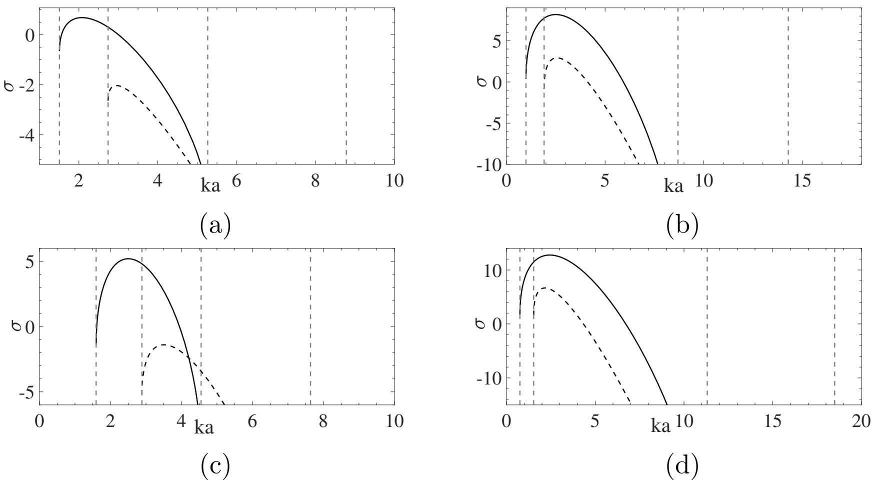

(a) (b)

(c) (d)

Figure 6.7: Growth rate curves for first and second elliptic modes for secondary vortex in locally unstable cases: (a) case C1, (b) case D1, (c) case C2, and (d) case D2. The first mode is represented by dash line, and the second mode is denoted by the solid line.

(cases C2 and D2) (figures 6.7(c) and (d)).

6.4 Shear layer shedding characteristics in diverging channel

A separation bubble forms near the initial diverging region due to unsteady separation, constituting a spanwise vortex roll and induced positive vortex in the boundary layer. A close-up image of the vortex shedding and three-dimensional disintegration of the separation bubble vortices is illustrated in figure 6.8. Similar to the shedding process observed by Wissink and Rodi [38], consecutive formation of the vortex rolls is evidenced during the deceleration phase (figure 5.18). As the flow decelerates further, the streamwise velocity weakens, amplifying the perturbations developing due to vortex interactions. As the flow decelerates ($t^* = 0.61$), the secondary vortices generate a spanwise oscillation during the shedding process and develop into spanwise loops over the primary negative vortex (PS2). Decay in streamwise velocity induces an oscillation in the separation bubble due to the amplification of perturbations (PS3). As the flow progress ($t^* = 0.63$), the vortex structure (PS3) sheds downstream, creating a short interval and a turbulent separation bubble (PS4). Further deceleration leads to the disintegration of the separation bubble and moves to a turbulent regime ($t^* = 0.65$). The formation of a turbulent separation bubble leads to

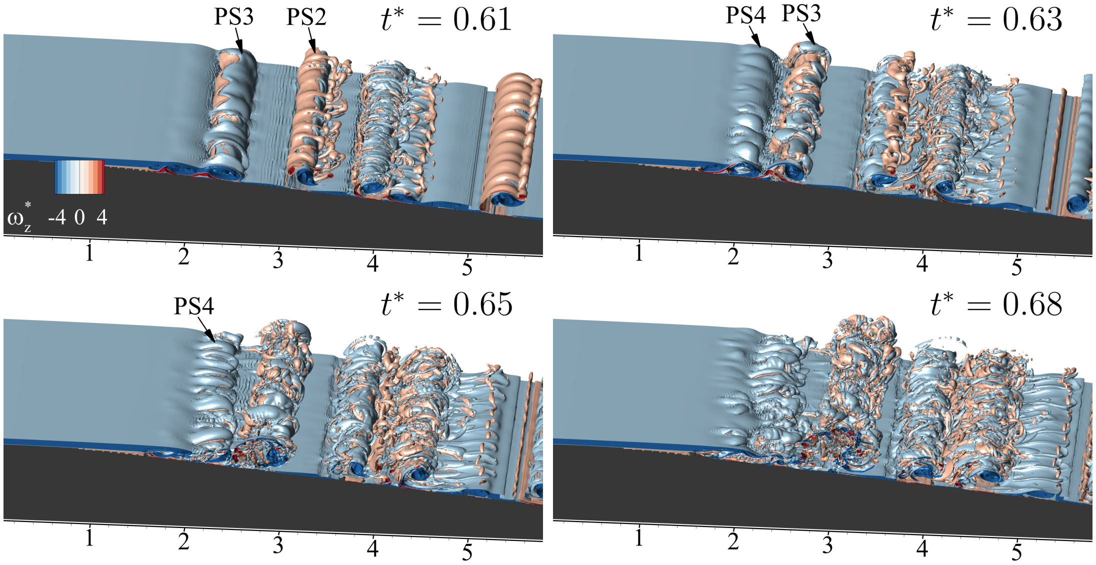

Figure 6.8: Three-dimensional disintegration of the separation bubble.

an uneven shedding of the turbulent flow features similar to the flow evolution observed by Wissink and Rodi [38] ($t^* = 0.68$). Unlike the bluff body cases, the diverging channel shows shedding characteristics only for two cases with higher Reynolds numbers accompanied by low deceleration. In figure 6.9, the spanwise vorticity at a downstream location is probed to identify the temporal characteristics of the vortex shedding due to unsteady separation for case C3 and case D3. In case C3, vortex generation initiates around $t^* = 0.3$, which is at an earlier flow instance than in case D3. Shortly after the vortex ejection, the formation of a positive vortex is evident by a sharp positive peak. Further oscillations are indicative of the subsequent formation and shedding of vortex structures. High-frequency perturbations in the zero mean inflow phase are triggered by three-dimensional fragmentation of the flow features in case C3. The vortex shedding in case D3 is more frequent and reveals a three-dimensional breakdown at an earlier stage in the flow. The underlying frequency of the vortex shedding is identified by the frequency spectra obtained from the Fourier transforms of the vorticity evolution. The highest peak in the frequency spectra obtained by the Fourier analysis indicates the shedding frequency and is marked in figure 6.9(b) for cases C3 and D3. A second dominant frequency lies close to the subsequent harmonics of the preceding dominant frequency in both cases.

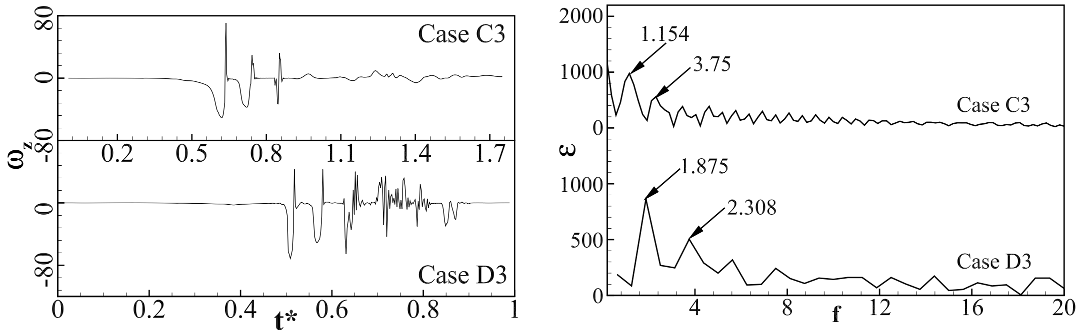

(a) (b)

Figure 6.9: Spectra analysis of vorticity probe for spatially unstable cases. (a) Temporal variation of spanwise vorticity (case C3: x = 2.633, y = 0.914; case D3: x = 2.32, y = 0.964), and (b) frequency spectra of the spanwise vorticity variation.

6.4.1 Temporal characteristics of unsteady separation

The temporal characteristics of the periodic shedding of two-dimensional flow structures in type III cases are revealed by the DMD analysis of two-dimensional snapshots of spanwise vorticity. Unlike the former category cases, rapid evolution and the streamwise advection of flow features due to the low deceleration rate hinders the three-dimensional DMD analysis of streamwise vorticity. A total of 75 snapshots lying in the initial deceleration period between t_i and t_f are used for the DMD analysis for both cases with a time step ($\Delta\tau$) of 2×10^{-2}. Frequency was invariant when the number of snapshot sizes was increased. Figure 6.10 summarizes the DMD analysis of the spanwise vorticity in spatially unstable cases. Typical, the Ritz circle plotted in figures 6.10(a) and (b) indicate the stability of DMD modes. The red symbols indicate the growing modes of cases C3 and D3 that lie outside the unit circle. To further emphasize the destabilizing nature, figures 6.10(c) and (d) present a bar diagram of frequency (f_{DMD}) plotted against the growth rate (σ) determined using DMD analysis. In each case, 1_σ denotes the most unstable mode based on the growth rate criteria. Growth rates and frequency information for each mode is provided in each figure. Figures 6.10(e) and (f) display the most prominent (highest growth rate) mode for cases C3 and D3, respectively. The peak frequencies of both modes are higher in the high Reynolds number case (case D3). Invariably, the first mode represents the growth of the vortex from the separation bubble over the diverging channel. A second dominant mode holds a frequency nearly equal to the second harmonic, indicating the second dominant peak of the vorticity frequency spectra (figures 6.10 (g) and (h)). An alternate pattern

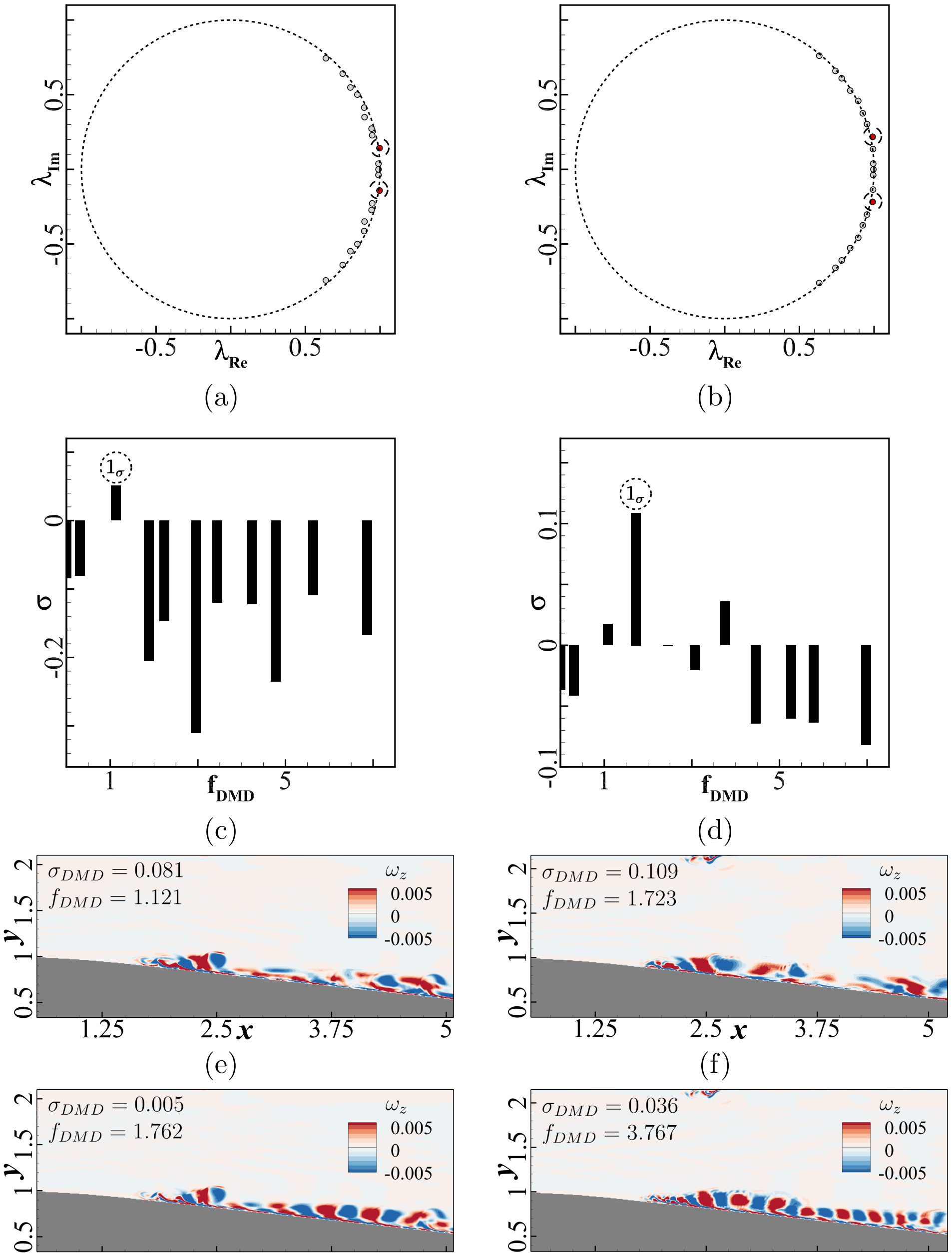

Figure 6.10: DMD analysis of spanwise vorticity evolution for cases C3 and D3. (a) Ritz circle (case C3), (b) Ritz circle (case D3); frequency vs growth rate for: (c) case C3, (d) case D3; (e) first mode (case C3), (f) first mode (case D3), (g) second mode (case C3), and (h) second mode (case D3).

Case	t_i (s)	t_f (s)	Average displacement thickness (δ^*_{avg})	Average velocity U_{avg} (m/s)	Probe analysis		DMD analysis	
					Identified frequency	Strouhal number	Identified frequency	Strouhal number
C3	4.2	5.7	0.010540	0.050637	1.154	0.24	1.121	0.23
D3	3.6	5.1	0.008361	0.092127	1.875	0.17	1.762	0.16

Table 6.2: Temporal characteristics of vortex shedding due to unsteady separation.

in the second mode indicates the spanwise vortex roll-ups over the diverging region. In the case of D3, early vortex development leads to continuous shedding mode, as shown in figure 6.10(h). DMD results also point to the vortex shedding from the separation bubble in this period. Both analyses indicate two-dimensional vortex shedding characteristics, which later disintegrate three-dimensionally during the zero mean inflow phase.

A consolidated comparison of temporal characteristics obtained from frequency spectra with the results from DMD analysis is included in table 6.2. An average displacement thickness is calculated for the velocity profiles over the separation point and is denoted as δ^*_{avg}. Similarly, an average velocity is calculated by taking the mean of the average velocity of velocity profiles over the separation point (between t_i and t_f). Strouhal number $\left(St = \frac{f\delta^*_{avg}}{U_{avg}}\right)$ is calculated for both probe analysis and DMD analysis by using the average displacement thickness along with the average velocity. In the present study, the unstable mode frequency scales with the viscosity length scales generally used in boundary layer transition studies [102, 103], and identified Strouhal frequencies lie near 0.2. In light of the fact that only two out of twelve cases show periodic vortex shedding, the results are insufficient to support the generalization of the Strouhal number relation.

6.5 Summary

Three-dimensional flow features in a low spatial gradient flow are highly associated with the temporal parameters. According to the secondary instability initiation time, the flow is categorized into three different categories. In this chapter, the spatial and temporal nature of the secondary instability is further investigated through the comprehensive analysis of streamwise vorticity and the λ_2 method. Since any spanwise oscillations are formed in the first category of cases, further investigations are carried out for only both type II and type III cases.

Analogous to the streamwise vorticity, an evolution of the spanwise velocity component also indicates the three-dimensional flow disintegration. From the contours of distribution of the average spanwise velocity component for three-dimensional cases, the clear distinction between the locally unstable structures as well as the spatially distributed structures is evident. In addition, the temporal evolution of the spanwise component also indicates a rapid growth during the zero mean inflow phase for the Type II cases. Also, the cases indicating the highest growth rate coincides with the highest theoretical growth rate cases for elliptical instability.

An initial analysis of the spatial characteristics of λ_2 structure identifies a spanwise oscillation forming over the secondary vortex ejected from the boundary layer vortex. Through a sectional analysis, an alternate distribution of the streamwise vorticity in the spanwise direction indicates a strong influence of streamwise vorticity generation in instability growth. Further DMD analysis of the streamwise vorticity component indicates an unstable mode with spatial characteristics analogous to the wavelength identified through the streamwise vorticity pattern.

The development of secondary instability is associated with the formation and ejection of a counter-rotating vortex pair induced in the deceleration phase. So a further analysis of the origin of the instability is carried out through theoretical growth rate estimates. Theoretical elliptical instability growth rate analysis of the Lamb-Oseen approximation of the vortex pair indicates an unstable nature. Also, the wavelength identified through both DMD and streamwise vorticity pattern lies within the range of elliptical instability nature.

In type III cases, the vortex dynamics indicate a complex nature due to the low deceleration unsteady separation and shedding of vortex flow features observed. Further temporal characteristics of coherent flow features are identified through DMD analysis and compared with quantified values obtained from spectra analysis provided in the previous chapter.

Chapter 7

Conclusions

Unlike the conventional studies focusing on the flow transition in a flow field under steady or oscillatory inflow conditions, the onset of turbulence in the vortical structures developed from a transitional boundary layer is a highly challenging and crucial design engineering aspect. Transitional flows of such spatiotemporal nature can significantly affect the performance of many engineering applications such as solid rocket motors, turbine blades, airfoils, etc. In this work, we employed direct numerical simulations with the open-source solver INCOMPACT3D to investigate the three-dimensional transition of vortex flow structures in a fluid flow field. The DNS of flow evolution and later disintegration of vortex flow structures from a transitional boundary layer that was developed through a combination of spatial and temporal pressure gradient components takes multiple transition routes with respect to the inflow conditions.

A complex body coupled with transient inflow poses a challenging computational problem for traditional computation methods, so the current study uses the immersed boundary method coupled with higher-order compact schemes for spatial discretization in a Cartesian framework. Highly parallelized INCOMPACT3D utilizes spectral methods to solve the modified Pressure Poisson equation used for immersed boundary approach. For the current investigation, the time integration is carried out using the third-order Adam Bashforth scheme. Identifying the origin of instability is challenging due to the complexity arising from the spatial and temporal pressure gradient components of the transitional boundary layer. The current investigation employed a wide range of methods, both theoretical and numerical, to examine the underlying coherent flow structures and their temporal characteristics. The wall-attached bluff body induces a significant spatial pressure gradient that promotes flow separation in the early flow phase (acceleration phase); the separated shear layer rolls into a primary vortex on the body's leeward side, creating a low-velocity region. Further, the flow exhibits the shear layer instabilities as the Reynolds number of the flow

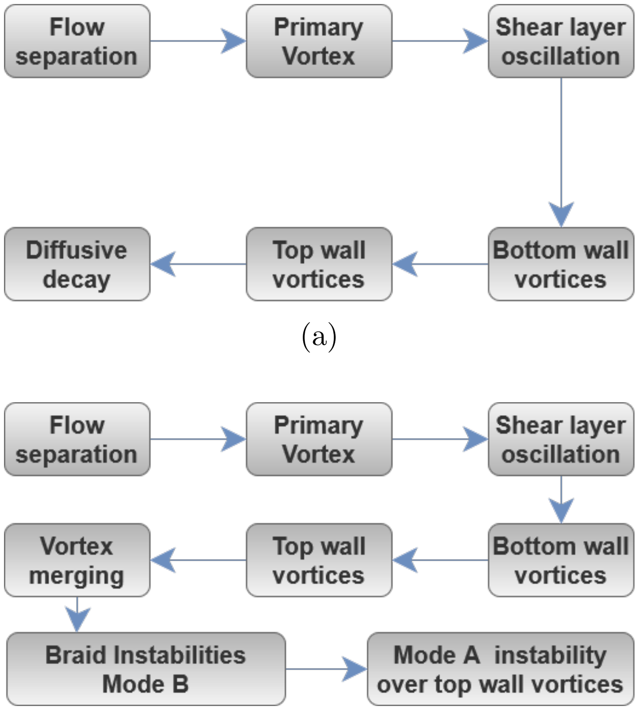

(a)

(b)

Figure 7.1: Flow transition route in Bluff body case: (a) two-dimensional cases, and (b) three-dimensional cases.

increases, while the three-dimensional breakdown is observed in cases with high Reynolds numbers. Vortex flow features diffuse during the dead inflow phase at low and moderate Reynolds numbers. A systematic representation of the flow evolution sequence in two-dimensional cases are provided in figure 7.1 (a). The shear layer instability in the bluff body case rolls into spanwise vortex rolls orbiting around the primary vortex; as a result of induction from these vortex roll-ups, the boundary layer adjacent to the body surface develops vortex rolls with an opposite sense of rotation. Furthermore, the shear layer vortex rolls integrate into the primary vortex core, while body vortices are propelled to core flow. Likewise, the top wall generates vortex pairs that descend downward into the core flow. Observations of wake vortices in a bluff body wake indicate the development of Mode A and Mode B instabilities, which are correlated with elliptic and hyperbolic instabilities developed in the core and braid regions of wake vortices. Shortwave length Mode B instabilities are demonstrated in the separation bubble vortices and body vortices, which exhibit a merging transition due to the strong rotational field generated by the primary vortex, whereas Mode A instabilities are observed in the boundary layer vortices developed over the top wall. A consolidated chain of events leading to secondary instability formation in high inflow velocities is depicted in figure 7.1 (b).

A detailed analysis of the streamwise velocity field in the wake reveals a highly inflectional velocity profile instigating the flow separation and the shear layer oscillations. Further, spectra analysis of both probe data for vertical velocity component and momentum thickness variation reveals the shear layer shedding frequencies for each case. The three-dimensional spatial structure of the secondary instabilities over the vortex flow features is exemplified using the λ_2 method. Also, underlying coherent structures inside the flow field are identified through dynamic mode decomposition of both vertical velocity and spanwise vorticity data. In addition, the frequency identified for the shear layer instability coincides with the growth rate of unstable DMD mode determined through the highest growth rate criteria. The DMD analysis of the vertical velocity component also indicates similar information. Unlike the spanwise vorticity, strengthening of the streamwise vorticity component is closely associated with three-dimensional disintegration and is further investigated using the vorticity generation equation. From the vorticity generation equation analysis, it is evidenced that the evolution of the tilting mechanism in the deceleration phase gets amplified through the stretching component in the dead inflow phase leading to spanwise oscillations and later decomposition. Vortex flow structures and flow evolution in the diverging channel are significantly altered by the temporal inflow parameters. Due to the low spatial gradient in the diverging channel, a long separation bubble became evident in the initial diverging section. Also, multiple vortex flow structures were developed over the diverging section of the channel. Based on the three-dimensional nature of the flow structures developed inside the flow field, the flow cases are classified into three categories. A chronological order of flow progression and the instances of the flow features developing inside each case is illustrated in figure 7.2. In cases with low and moderate Reynolds numbers (Type I), vortices are induced and develop during the late deceleration stage, which then diffuses during the dead inflow phase (figure 7.2 (a)). In high Reynolds number cases with moderate and high deceleration, the flow features develop near the initial diverging section during the dead inflow region due to the reverse flow profiles generated in the boundary layer (figure 7.2 (b)). Such cases classified as Type II cases move to a three-dimensional disintegration through an elliptic instability arising over the induced positive vortex ejected from the bottom boundary. For low deceleration cases Type III, the unsteady separation sheds vortex structures that break down at the downstream position at a later flow time in a similar manner in the deceleration phase (figure 7.2 (c)). Vortex merging phenomena and separation bubble breakdown is also observed in such cases.

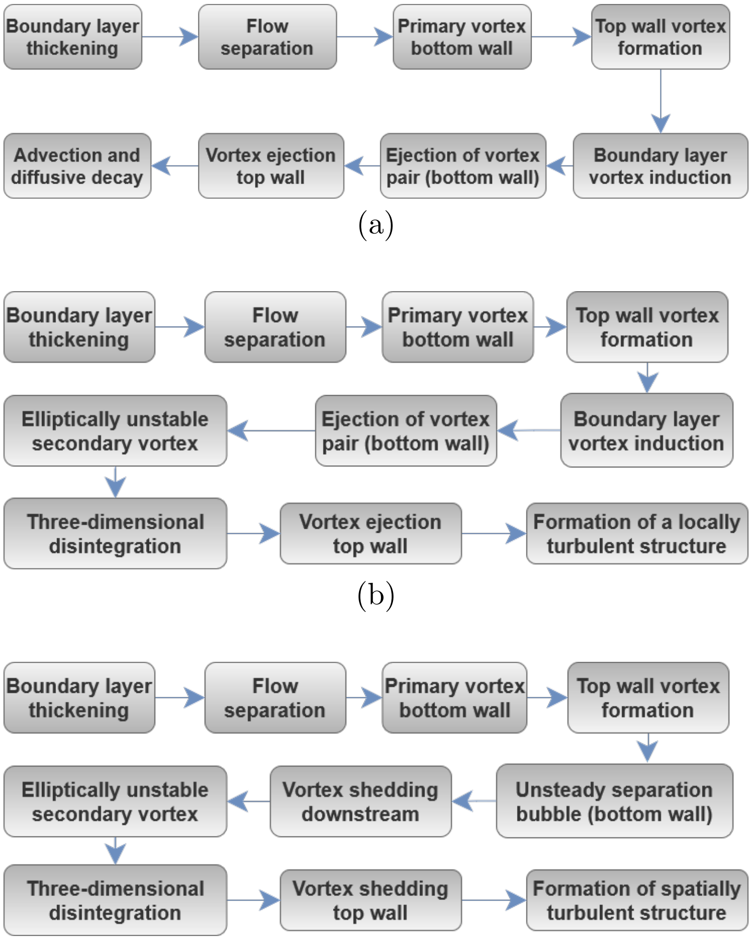

(a)

(b)

(c)

Figure 7.2: Flow transition route in diverging channel case: (a) two-dimensional (type I) cases, (b) locally unstable (type II) cases, and (c) spatially unstable (type III) cases.

Spatial and temporal characteristics identified through DMD analysis of the streamwise vorticity evolution indicate an unstable spatial streamwise vorticity structure. Alternatively, the streamwise vorticity coherent structures obtained from DMD analysis indicate an identical spanwise wavelength for the unstable mode with an average wavelength of elliptical instability. Further, the theoretical growth rate estimations for elliptical instability of the vortex structures developed in the diverging channel also show an unstable nature for vortex structures. In higher Reynolds cases with low deceleration, the DMD analysis of spanwise vorticity identifies the most unstable mode with a frequency identical to the shedding frequency.

The present investigation identifies the three-dimensional instability mechanism devel-

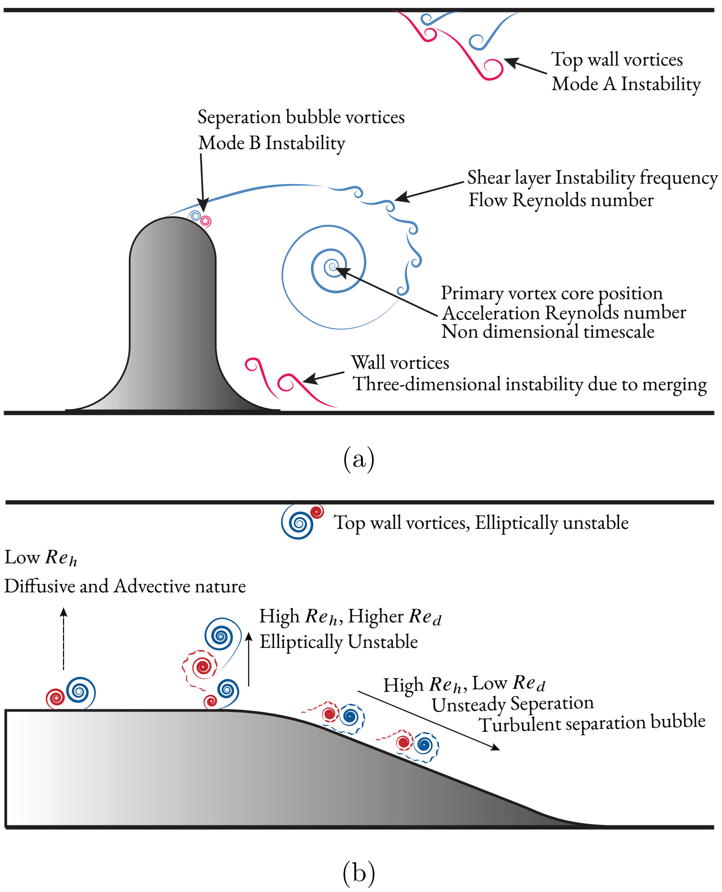

Figure 7.3: Depiction of different three-dimensional transitions in (a) bluff body wake and (b) diverging channel wake.

oping in the wake of vortices evolving from an unsteady boundary layer subjected to an adverse pressure gradient. A consolidated image of the distinct flow features evolving in the flow field for both cases is given in figure 7.3. The primary instability in both geometries is identified through Rayleigh's inflection criteria, indicating highly inflectional velocity profiles developing over the body surface during the flow evolution. A strong spatial gradient component initiates the flow separation during the early acceleration phase, while in low spatial gradient flow, the adverse pressure gradient develops during the deceleration phase. The shear layer instability frequency increases with an increase in the flow velocity; also, the frequency spectra of momentum thickness variations hold identical spectra. Flow features developed for both geometries decay through diffusion in low and moderate inflow velocities due to the suppression of spanwise oscillations. Secondary instability develops in both geometries through different transition mechanisms generated in the wake vortices. The low-velocity region behind the bluff body shows a merging mechanism inducing small wavelength braid instabilities. Similarly, the flow structures evolving over top wall surfaces indicate the formation of high wavelength mode A instabilities. While in the diverging channel, the higher temporal component induces the formation of counter-rotating pairs susceptible to elliptical instability, and in low temporal component cases, an unsteady separation bubble induces vortex shedding, which further causes merging as well as elliptically unstable vortex flow features.

Bibliography

[1] SP Das, U Srinivasan, and JH Arakeri. Unsteady separation and vortex shedding from a laminar separation bubble over a bluff body. *Journal of Fluids and Structures*, 40:233–245, 2013.

[2] SP Das, U Srinivasan, and JH Arakeri. Instabilities in unsteady boundary layers with reverse flow. *European Journal of Mechanics-B/Fluids*, 55:49–62, 2016.

[3] Debopam Das and Jaywant H Arakeri. Transition of unsteady velocity profiles with reverse flow. *Journal of Fluid Mechanics*, 374:251–283, 1998.

[4] Sylvain Laizet and Ning Li. Incompact3d: A powerful tool to tackle turbulence problems with up to o (105) computational cores. *International Journal for Numerical Methods in Fluids*, 67(11):1735–1757, 2011.

[5] Hong Q Yang, Jeff West, and Robert E Harris. Coupled fluid–structure interaction analysis of solid rocket motor with flexible inhibitors. *Journal of Spacecraft and Rockets*, 55(2):303–314, 2018.

[6] Prabal Singh Negi, Ricardo Vinuesa, Ardeshir Hanifi, Philipp Schlatter, and Dan S Henningson. Unsteady aerodynamic effects in small-amplitude pitch oscillations of an airfoil. *International Journal of Heat and Fluid Flow*, 71:378–391, 2018.

[7] DI Pullin and AE Perry. Some flow visualization experiments on the starting vortex. *Journal of Fluid Mechanics*, 97(2):239–255, 1980.

[8] D Pierce. Photographic evidence of the formation and growth of vorticity behind plates accelerated from rest in still air. *Journal of Fluid Mechanics*, 11(3):460–464, 1961.

[9] R.D. Sandberg and V. Michelassi. Fluid dynamics of axial turbomachinery: Blade- and stage-level simulations and models. *Annual Review of Fluid Mechanics*, 54: 255–285, 2022.

[10] D. Greenblatt and I.J. Wygnanski. The control of flow separation by periodic excitation. *Progress in Aerospace Sciences*, 36(7):487–545, 2000. ISSN 0376-0421. doi: https://doi.org/10.1016/S0376-0421(00)00008-7. URL `https://www.sciencedirect.com/science/article/pii/S0376042100000087`.

[11] Andrey Roshko. Perspectives on bluff body aerodynamics. *Journal of Wind Engineering and Industrial Aerodynamics*, 49(1-3):79–100, 1993.

[12] Charles HK Williamson. Vortex dynamics in the cylinder wake. *Annual review of fluid mechanics*, 28(1):477–539, 1996.

[13] Mark C. Thompson, Thomas Leweke, and Kerry Hourigan. Bluff bodies and wake-wall interactions. *Annual Review of Fluid Mechanics*, 53(1):347–376, 2021.

[14] PG Saffman and GR Baker. Vortex interactions. *Annual Review of Fluid Mechanics*, 11(1):95–121, 1979.

[15] Steven C Crow. Stability theory for a pair of trailing vortices. *AIAA journal*, 8(12): 2172–2179, 1970.

[16] Sheila E Widnall, Donald B Bliss, and Chon-Yin Tsai. The instability of short waves on a vortex ring. *Journal of Fluid Mechanics*, 66(1):35–47, 1974.

[17] Patrice Meunier and Thomas Leweke. Three-dimensional instability during vortex merging. *Physics of Fluids*, 13(10):2747–2750, 2001.

[18] GP Klaassen and WR Peltier. The role of transverse secondary instabilities in the evolution of free shear layers. *Journal of Fluid Mechanics*, 202:367–402, 1989.

[19] David C Fritts, L Wang, TS Lund, and SA Thorpe. Multi-scale dynamics of kelvin–helmholtz instabilities. part 1. secondary instabilities and the dynamics of tubes and knots. *Journal of Fluid Mechanics*, 941:A30, 2022.

[20] T. Leweke and C.H.K. Williamson. Three-dimensional instabilities in wake transition. *European Journal of Mechanics-B/Fluids*, 17(4):571–586, 1998.

[21] CHK Williamson. Three-dimensional wake transition. *Journal of Fluid Mechanics*, 328:345–407, 1996.

[22] Rajat Mittal and S Balachandar. Direct numerical simulation of flow past elliptic cylinders. *Journal of Computational Physics*, 124(2):351–367, 1996.

[23] S Dong, GE Karniadakis, A Ekmekci, and D Rockwell. A combined direct numerical simulation–particle image velocimetry study of the turbulent near wake. *Journal of Fluid Mechanics*, 569:185–207, 2006.

[24] Hongyi Jiang, Liang Cheng, Scott Draper, Hongwei An, and Feifei Tong. Three-dimensional direct numerical simulation of wake transitions of a circular cylinder. *Journal of Fluid Mechanics*, 801:353–391, 2016.

[25] Charles S Peskin. The immersed boundary method. *Acta numerica*, 11:479–517, 2002.

[26] Roberto Verzicco. Immersed boundary methods: Historical perspective and future outlook. *Annual Review of Fluid Mechanics*, 55, 2023.

[27] D Das and JH Arakeri. Unsteady laminar duct flow with a given volume flow rate variation. *Journal of applied mechanics*, 67(2):274–281, 2000.

[28] N. Ramalingam and S.P. Das. Instabilities of decaying flow in a rectangular channel. *Journal of The Institution of Engineers (India): Series C*, 101(5):821–836, 2020.

[29] P.J. Schmid. Dynamic mode decomposition of numerical and experimental data. *Journal of fluid mechanics*, 656:5–28, 2010.

[30] Clarence W. Rowley, Igor Mezić, Shervin Bagheri, Philipp Schlatter, and Dan S. Henningson. Spectral analysis of nonlinear flows. *Journal of Fluid Mechanics*, 641: 115–127, 2009. doi: 10.1017/S0022112009992059.

[31] Peter J. Schmid. Dynamic mode decomposition of numerical and experimental data. *Journal of Fluid Mechanics*, 656:5–28, 2010. doi: 10.1017/S0022112010001217.

[32] Abu Seena and Hyung Jin Sung. Dynamic mode decomposition of turbulent cavity flows for self-sustained oscillations. *International Journal of Heat and Fluid Flow*, 32(6):1098–1110, 2011.

[33] Thomas Leweke and Charles HK Williamson. Cooperative elliptic instability of a vortex pair. *Journal of fluid mechanics*, 360:85–119, 1998.

[34] Mark Christopher Thompson, Kerry Hourigan, Kris Ryan, and Gregory John Sheard. Wake transition of two-dimensional cylinders and axisymmetric bluff bodies. *Journal of Fluids and Structures*, 22(6-7):793–806, 2006.

[35] GJ Sheard, Thomas Leweke, Mark Christopher Thompson, and Kerry Hourigan. Flow around an impulsively arrested circular cylinder. *Physics of Fluids*, 19(8): 083601, 2007.

[36] OR Tutty and TJ Pedley. Oscillatory flow in a stepped channel. *Journal of Fluid Mechanics*, 247:179–204, 1993.

[37] Moshe Rosenfeld. A numerical study of pulsating flow behind a constriction. *Journal of Fluid Mechanics*, 301:203–223, 1995.

[38] J.G. Wissink and W. Rodi. Direct numerical simulations of transitional flow in turbomachinery. *Journal of Turbomachinery*, 128(4):668–678, 02 2006. ISSN 0889-504X. doi: 10.1115/1.2218517. URL `https://doi.org/10.1115/1.2218517`.

[39] J.G. Wissink, V. Michelassi, and W. Rodi. Heat transfer in a laminar separation bubble affected by oscillating external flow. *International journal of heat and fluid flow*, 25(5):729–740, 2004.

[40] P Hall and KH Parker. The stability of the decaying flow in a suddenly blocked channel. *Journal of Fluid Mechanics*, 75(2):305–314, 1976.

[41] M. S. Ghidaoui and A. A. Kolyshkin. A quasi-steady approach to the instability of time-dependent flows in pipes. *Journal of Fluid Mechanics*, 465:301–330, 2002. ISSN 00221120. doi: 10.1017/S0022112002001076.

[42] A. Nayak and D. Das. Transient growth of optimal perturbation in a decaying channel flow. *Physics of Fluids*, 29(6), 2017. ISSN 10897666. doi: 10.1063/1.4985000.

[43] A. Kannaiyan, S. Natarajan, and B.R. Vinoth. Stability of a laminar pipe flow subjected to a step-like increase in the flow rate. *Physics of Fluids*, 34(6):064102, 2022.

[44] George Gabriel Stokes. On the theory of oscillatory waves. *Trans. Camb. Phil. Soc.*, 8:411–455, 1847.

[45] M Susan Bloor. The transition to turbulence in the wake of a circular cylinder. *Journal of Fluid Mechanics*, 19(2):290–304, 1964.

[46] CH Williamson. Oblique and parallel modes of vortex shedding in the wake of a circular cylinder at low reynolds numbers. Technical report, California Inst of Tech Pasadena Graduate Aeronautical Labs, 1989.

[47] M Matsumoto. Vortex shedding of bluff bodies: a review. *Journal of Fluids and Structures*, 13(7-8):791–811, 1999.

[48] Sundara Rajagopalan and Robert Anthony Antonia. Flow around a circular cylinder—structure of the near wake shear layer. *Experiments in fluids*, 38:393–402, 2005.

[49] S Sarkar and Sudipto Sarkar. Vortex dynamics of a cylinder wake in proximity to a wall. *Journal of Fluids and Structures*, 26(1):19–40, 2010.

[50] OR Tutty and TJ Pedley. Unsteady flow in a nonuniform channel: A model for wave generation. *Physics of Fluids*, 6(1):199–208, 1994.

[51] Moshe Rosenfeld and Shmuel Einav. The Effect of Constriction Size on the Pulsatile Flow in a Channel. *Journal of Fluids Engineering*, 117(4):571–576, 12 1995. ISSN 0098-2202. doi: 10.1115/1.2817303. URL `https://doi.org/10.1115/1.2817303`.

[52] Paola Costamagna, Giovanna Vittori, and Paolo Blondeaux. Coherent structures in oscillatory boundary layers. *Journal of Fluid Mechanics*, 474:1–33, 2003.

[53] L.E. Jones, R.D. Sandberg, and N.D. Sandham. Direct numerical simulations of forced and unforced separation bubbles on an airfoil at incidence. *Journal of Fluid Mechanics*, 602:175–207, 2008.

[54] C.P. Caulfield and R.R. Kerswell. The nonlinear development of three-dimensional disturbances at hyperbolic stagnation points: a model of the braid region in mixing layers. *Physics of Fluids*, 12(5):1032–1043, 2000.

[55] A. Mashayek and W.R. Peltier. The 'zoo'of secondary instabilities precursory to stratified shear flow transition. part 1 shear aligned convection, pairing, and braid instabilities. *Journal of Fluid Mechanics*, 708:5–44, 2012.

[56] YANG Zhiyin. Secondary instability of separated shear layers. *Chinese Journal of Aeronautics*, 32(1):37–44, 2019.

[57] SF Shen. Some considerations on the laminar stability of time-dependent basic flows. *Journal of the Aerospace Sciences*, 28(5):397–404, 1961.

[58] Mingyan Zhao, Mohamed Salah Ghidaoui, and Andrei A Kolyshkin. Perturbation dynamics in unsteady pipe flows. *Journal of fluid mechanics*, 570:129–154, 2007.

[59] Duo Xu, Baofang Song, and Marc Avila. Non-modal transient growth of disturbances in pulsatile and oscillatory pipe flows. *Journal of Fluid Mechanics*, 907:R5, 2021.

[60] Tao Wei and CR Smith. Secondary vortices in the wake of circular cylinders. *Journal of Fluid Mechanics*, 169:513–533, 1986.

[61] James C Williams III. Incompressible boundary-layer separation. *Annual Review of Fluid Mechanics*, 9(1):113–144, 1977.

[62] M. Alam and N.D. Sandham. Direct numerical simulation of ‘short’laminar separation bubbles with turbulent reattachment. *Journal of Fluid Mechanics*, 410:1–28, 2000.

[63] M. Embacher and H.F. Fasel. Direct numerical simulations of laminar separation bubbles: investigation of absolute instability and active flow control of transition to turbulence. *Journal of fluid mechanics*, 747:141–185, 2014.

[64] J.R. Brinkerhoff and M.I. Yaras. Interaction of viscous and inviscid instability modes in separation–bubble transition. *Physics of Fluids*, 23(12):124102, 2011.

[65] A. Lambert and S. Yarusevych. Effect of angle of attack on vortex dynamics in laminar separation bubbles. *Physics of Fluids*, 31(6):064105, 2019.

[66] A. Sengupta and P. Tucker. Effects of forced frequency oscillations and unsteady wakes on the separation-induced transition in pressure gradient dominated flows. *Physics of Fluids*, 32(9):094113, 2020.

[67] A. Mariotti, A.N. Grozescu, G. Buresti, and M.V. Salvetti. Separation control and efficiency improvement in a 2d diffuser by means of contoured cavities. *European Journal of Mechanics-B/Fluids*, 41:138–149, 2013.

[68] M. Garcia-Villalba, N. Li, W. Rodi, and M.A. Leschziner. Large-eddy simulation of separated flow over a three-dimensional axisymmetric hill. *Journal of fluid Mechanics*, 627:55–96, 2009.

[69] M.E. Goldstein and L.S. Hultgren. Boundary-layer receptivity to long-wave free-stream disturbances. *Annual Review of Fluid Mechanics*, 21(1):137–166, 1989.

[70] S.S. Diwan and O.N. Ramesh. On the origin of the inflectional instability of a laminar separation bubble. *Journal of Fluid Mechanics*, 629:263–298, 2009.

[71] K. Jain, A.I. Ruban, and S. Braun. On receptivity of marginally separated flows. *Journal of Fluid Mechanics*, 907, 2021.

[72] N.D. Sandham. Transitional separation bubbles and unsteady aspects of aerofoil stall. *The Aeronautical Journal (1968)*, 112(1133):395–404, 2008. doi: 10.1017/S0001924000002359.

[73] I.E. Abdalla and Z. Yang. Numerical study of the instability mechanism in transitional separating–reattaching flow. *International Journal of Heat and Fluid Flow*, 25(4):593–605, 2004.

[74] O. Marxen, M. Lang, and U. Rist. Vortex formation and vortex breakup in a laminar separation bubble. *Journal of Fluid Mechanics*, 728:58–90, 2013.

[75] A.G. Kravchenko and P. Moin. On the effect of numerical errors in large eddy simulations of turbulent flows. *Journal of computational physics*, 131(2):310–322, 1997.

[76] Sanjiva K Lele. Compact finite difference schemes with spectral-like resolution. *Journal of computational physics*, 103(1):16–42, 1992.

[77] Alan George, Lan Chieh Huang, Wei-Pai Tang, and Ya Dan Wu. Numerical simulation of unsteady incompressible flow (re $\leq$ 9500) on the curvilinear half-staggered mesh. *SIAM Journal on Scientific Computing*, 21(6):2331–2351, 2000.

[78] N. Li and S. Laizet. 2decomp & fft-a highly scalable 2d decomposition library and fft interface. In *Cray user group 2010 conference*, pages 1–13, 2010.

[79] Rayleigh Rayleigh. On the stability or instability of certain fluid motions (iii.). *Proceedings of the London Mathematical Society*, 1(1):5–12, 1895.

[80] Hermann Schlichting and Joseph Kestin. *Boundary layer theory*, volume 121. Springer, 1961.

[81] Clarence W Rowley and Scott TM Dawson. Model reduction for flow analysis and control. *Annual Review of Fluid Mechanics*, 49:387–417, 2017.

[82] H K Jang, C E Ozdemir, J. H. Liang, and M. Tyagi. Oscillatory flow around a vertical wall-mounted cylinder: Dynamic mode decomposition. *Physics of Fluids*, 33(2):25113, 2021. ISSN 10897666. doi: 10.1063/5.0032644. URL `https://doi.org/10.1063/5.0032644`.

[83] Yunqing Liu, Jincheng Long, Qin Wu, Biao Huang, and Guoyu Wang. Data-driven modal decomposition of transient cavitating flow. *Physics of Fluids*, 33(11), 2021. ISSN 10897666. doi: 10.1063/5.0073266. URL `https://doi.org/10.1063/5.0073266`.

[84] Kunihiko Taira, Maziar S. Hemati, Steven L. Brunton, Yiyang Sun, Karthik Duraisamy, Shervin Bagheri, Scott T.M. Dawson, and Chi An Yeh. Modal analysis of fluid flows: Applications and outlook. *AIAA Journal*, 58(3):998–1022, 2020. ISSN 00011452. doi: 10.2514/1.J058462.

[85] M Palmer and P Freymuth. Analysis of vortex development from visualization of accelerating flow around an airfoil, starting from rest. In *17th Fluid Dynamics, Plasma Dynamics, and Lasers Conference*, page 1568, 1984.

[86] Fathi Finaish, M Palmer, and P Freymuth. A parametric analysis of vortex patterns visualized over airfoils in accelerating flow. *Experiments in fluids*, 5(4):284–288, 1987.

[87] JH Gerrard. The wakes of cylindrical bluff bodies at low reynolds number. *Phil. Trans. R. Soc. Lond. A*, 288(1354):351–382, 1978.

[88] Peter J Schmid, Dan S Henningson, and DF Jankowski. Stability and transition in shear flows. applied mathematical sciences, vol. 142. *Appl. Mech. Rev.*, 55(3): B57–B59, 2002.

[89] Jinhee Jeong and Fazle Hussain. On the identification of a vortex. *Journal of fluid mechanics*, 285:69–94, 1995.

[90] Hussein Mansy, Pan-Mei Yang, and David R. Williams. Quantitative measurements of three-dimensional structures in the wake of a circular cylinder. *Journal of Fluid Mechanics*, 270:277–296, 1994. doi: 10.1017/S0022112094004271.

[91] DM Harris and CHK Williamson. Instability of secondary vortices generated by a vortex pair in ground effect. *Journal of Fluid Mechanics*, 700:148–186, 2012.

[92] Suresh Behara and Sanjay Mittal. Flow past a circular cylinder at low reynolds number: Oblique vortex shedding. *Physics of fluids*, 22(5):054102, 2010.

[93] S. Le Dizes and F. Laporte. Theoretical predictions for the elliptical instability in a two-vortex flow. *Journal of Fluid Mechanics*, 471:169–201, 2002.

[94] T. Leweke, S. Le Dizes, and C.H.K. Williamson. Dynamics and instabilities of vortex pairs. *Annual Review of Fluid Mechanics*, 48:507–541, 2016.

[95] M.M. Rogers and R.D. Moser. The three-dimensional evolution of a plane mixing layer: the kelvin–helmholtz rollup. *Journal of Fluid Mechanics*, 243:183–226, 1992.

[96] S. Le Dizes. Non-axisymmetric vortices in two-dimensional flows. *Journal of Fluid Mechanics*, 406:175–198, 2000.

[97] S. Le Dizes. Three-dimensional instability of a multipolar vortex in a rotating flow. *Physics of Fluids*, 12(11):2762–2774, 2000.

[98] T. Miyazaki, T. Imai, and Y. Fukumoto. Three-dimensional instability of kirchhoff's elliptic vortex. *Physics of Fluids*, 7(1):195–202, 1995.

[99] D.W. Moore and P.G. Saffman. Structure of a line vortex in an imposed strain. In *Aircraft wake turbulence and its detection*, pages 339–354. Springer, 1971.

[100] R.R. Kerswell. Elliptical instability. *Annual review of fluid mechanics*, 34:83, 2002.

[101] F. Laporte and A. Corjon. Direct numerical simulations of the elliptic instability of a vortex pair. *Physics of Fluids*, 12(5):1016–1031, 2000.

[102] P.S. Klebanoff, W.G. Cleveland, and K.D. Tidstrom. On the evolution of a turbulent boundary layer induced by a three-dimensional roughness element. *Journal of Fluid Mechanics*, 237:101–187, 1992.

[103] A.A. Bakchinov, G.R. Grek, B.G.B. Klingmann, and V.V. Kozlov. Transition experiments in a boundary layer with embedded streamwise vortices. *Physics of Fluids*, 7 (4):820–832, 1995.

List of Publications

Refereed Journals

1. Sarath, K. P., & Manu, K. V. (2022). An investigation of bluff body flow structures in variable velocity flows. Physics of Fluids, 34(3), 034102. (Selected as Editor's Pick for the volume).
2. Sarath, K. P., & Manu, K. V. (2023). The onset of turbulence in decelerating diverging channel flows. Journal of Fluid Mechanics, 962, A30. (Selected as the cover picture for the volume)

Refereed Conferences

1. 7^{th} International & 45^{th} National Conference on Fluid Mechanics & Fluid Power(FMFP 2018)
2. 3^{rd} International & 25^{th} National Conference on Heat & Mass Transfer (ISHMTC-2019)
3. 4^{th} International & 26^{th} National Conference on Heat & Mass Transfer (ISHMTC-2021)

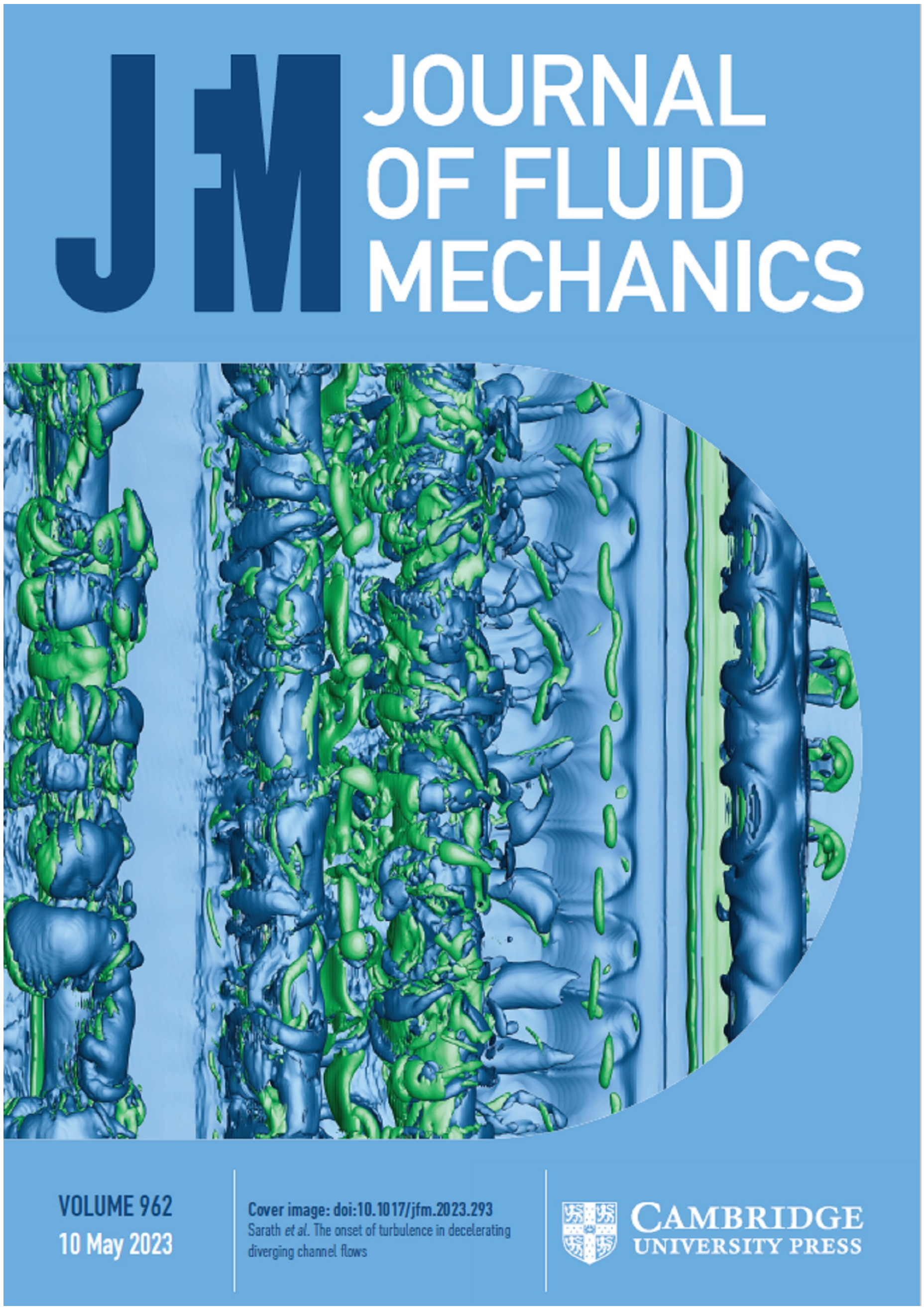

JFM JOURNAL OF FLUID MECHANICS

VOLUME 962
10 May 2023

Cover image: doi:10.1017/jfm.2023.293
Sarath *et al*. The onset of turbulence in decelerating diverging channel flows

CAMBRIDGE UNIVERSITY PRESS

Appendix A

Analytical solution for a non-zero mean inflow pulse in a two-dimensional channel.

The analytical solution of fully developed laminar pulsating flow for the variant volumetric flow rate is obtained using the Laplace transform technique combined with the Bromwich integral formula. To obtain the inflow velocity profiles for trapezoidal mean flow variation, we consider incompressible, fully-developed transient fluid flow with constant thermophysical properties in an infinitely long rectangular channel with a height of $2h$ and zero transverse velocities. Under the assumptions of uni-directionality and in the absence of body forces, the momentum equation is given by:

$$\frac{\partial u}{\partial t} = -\frac{1}{\rho}\left(\frac{\partial P}{\partial x}\right) + \nu\left(\frac{\partial^2 u}{\partial y^2}\right). \tag{A.1}$$

The boundary conditions are as follows:

$$u(h,t) = u(-h,t) = 0 \text{ (no slip)}, \tag{A.2}$$

$$u(y,0) = 0; \quad \frac{\partial\left(u(0,t)\right)}{\partial y} = 0, \tag{A.3}$$

$$\int_0^h u(y,t)\partial y = u_p(t)h. \tag{A.4}$$

Taking the Laplace transform of the momentum equation (equation A.1) and the boundary conditions (equations A.2 - A.4) yield:

$$\begin{aligned} \frac{d^2\overline{u}}{dy^2} - \frac{s}{\nu}\overline{u} &= \frac{1}{\mu}\frac{d\overline{P}}{dx} + \frac{1}{\nu}u(y,0), \\ \overline{u}(h,s) = \overline{u}(-h,s) &= 0, \\ \frac{\partial\overline{u}(0,s)}{\partial y} &= 0, \\ \int_0^h \overline{u}(y,s)\partial y &= \overline{u_p}(s)h. \end{aligned} \tag{A.5}$$

The general solution of equation (A.5) is:

$$\overline{u}(y,s) = c_1 e^{ky} + c_2 e^{-ky} + \phi_p.$$

where ϕ_p is the particular integral and applying the boundary conditions, k is attained as $k = \sqrt{\frac{s}{\nu}}$.

$$\overline{u}(y,s) = \phi_p \left[1 - \frac{(e^{ky} + e^{-ky})}{(e^{kh} + e^{-kh})} \right]. \tag{A.6}$$

To find the particular integral ϕ_p, we use the volume flow rate condition.

$$\int_0^h \phi_p \left[1 - \frac{(e^{ky} + e^{-ky})}{(e^{kh} + e^{-kh})} \right] dy = \overline{u_p}(s)h. \tag{A.7}$$

By integrating and simplifying the above equation, we get ϕ_p as:

$$\phi_p = \frac{\overline{u_p}(s)}{1 - \frac{1}{kh}\left[\frac{(e^{kh} - e^{-kh})}{(e^{kh} + e^{-kh})}\right]}, \tag{A.8}$$

and applying this in A.6 we get $\overline{u}(y,s)$ as:

$$\overline{u}(y,s) = \overline{u_p}(s)\frac{[(e^{kh} + e^{-kh}) - (e^{ky} + e^{-ky})]}{[(e^{kh} + e^{-kh}) - \frac{1}{kh}(e^{kh} - e^{-kh})]}. \tag{A.9}$$

The final solution is obtained from the inverse Laplace transform of the equations (A.10) and is found by applying Mellin's inverse formula.

$$u(y,t) = \frac{1}{2\pi i}\int_{\gamma-i\infty}^{\gamma+i\infty} \overline{u_p}(s)\frac{[(e^{kh}+e^{-kh})-(e^{ky}+e^{-ky})]}{[(e^{kh}+e^{-kh})-\frac{1}{kh}(e^{kh}-e^{-kh})]}e^{st}ds. \tag{A.10}$$

Here, the trapezoidal variation of the mean velocity with time ($u_p(t)$) is defined by equation 2.7. Analytical solution of the transient velocity profile is obtained by calculating the Laplace transform of equation 2.7 and substituting into equation A.9, succeeded by the inverse Laplace transform calculation. The Laplace transform of the mean velocity is given by

$$\begin{aligned}
\overline{u_p}(s) &= \frac{U_p}{t_0 s^2} \quad \text{for} \quad 0 \le t \le t_0, \\
&= \frac{U_p}{t_0}\left[\frac{1}{s^2}-\frac{e^{-t_0 s}}{s^2}\right] \quad \text{for} \quad t_0 \le t \le t_1, \\
&= \frac{U_p}{t_0}\left[\frac{1}{s^2}-\frac{e^{-t_0 s}}{s^2}\right] - \frac{U_p}{t_2-t_1}\left(\frac{e^{-t_1 s}}{s^2}\right) \quad \text{for} \quad t_1 \le t \le t_2, \\
&= \frac{U_p}{t_0}\left[\frac{1}{s^2}-\frac{e^{-t_0 s}}{s^2}\right] - \left(\frac{U_p}{t_2-t_1}\right)\left(\frac{e^{-t_1 s}}{s^2}\right) + \left(\frac{U_p}{t_2-t_1}\right)\left(\frac{e^{-t_2 s}}{s^2}\right) \quad \text{for} \quad t_2 \le t \le \infty.
\end{aligned}$$

For the acceleration phase, the Laplace transform of the constant acceleration phase is given by $\overline{u_p}(s) = \frac{U_p}{t_0 s^2}$. Then the solution is obtained by the inverse Laplace transform of the following equation:

$$u(y,t) = \frac{1}{2\pi i}\int_{\gamma-i\infty}^{\gamma+i\infty} \frac{U_p}{t_0 s^2}\frac{[(e^{kh}+e^{-kh})-(e^{ky}+e^{-ky})]}{[(e^{kh}+e^{-kh})-\frac{1}{kh}(e^{kh}-e^{-kh})]}e^{st}ds, \tag{A.11}$$

where $a\sqrt{s} = kh; a = \frac{y}{\sqrt{\nu}} = \frac{ch}{\sqrt{\nu}}$, $b\sqrt{s} = ky; b = \frac{h}{\sqrt{\nu}}$. Cauchy residue theorem is used to evaluate the complex integral given in equation A.11.

$$u(y,t) = \sum \text{residues of poles of} \left(\frac{U_p}{t_0 s^2}\left[\frac{(e^{b\sqrt{s}}+e^{-b\sqrt{s}})-(e^{a\sqrt{s}}+e^{-a\sqrt{s}})}{(e^{b\sqrt{s}}+e^{-b\sqrt{s}})-\frac{(e^{b\sqrt{s}}-e^{-b\sqrt{s}})}{b\sqrt{s}}}\right]e^{st}ds\right). \tag{A.12}$$

Here the poles are found to be $s = 0$, and $(e^{b\sqrt{s}}+e^{-b\sqrt{s}}) - \frac{(e^{b\sqrt{s}}-e^{-b\sqrt{s}})}{b\sqrt{s}} = 0$. $s = 0$ is a pole of second order, and the residue is given by:

$$\begin{aligned} Res|_{s=0} = \quad & \lim_{s\to 0} \quad \frac{1}{1!}\frac{d}{ds}\left(\frac{U_p}{t_0 s^2}\left[\frac{(e^{b\sqrt{s}}+e^{-b\sqrt{s}})-(e^{a\sqrt{s}}+e^{-a\sqrt{s}})}{(e^{b\sqrt{s}}+e^{-b\sqrt{s}})-\frac{(e^{b\sqrt{s}}-e^{-b\sqrt{s}})}{b\sqrt{s}}}\right]e^{st}ds\right), \\ = \quad & \lim_{s\to 0} \quad te^{st}\left[\frac{(e^{b\sqrt{s}}+e^{-b\sqrt{s}})-(e^{a\sqrt{s}}+e^{-a\sqrt{s}})}{(e^{b\sqrt{s}}+e^{-b\sqrt{s}})-\frac{(e^{b\sqrt{s}}-e^{-b\sqrt{s}})}{b\sqrt{s}}}\right]\frac{U_p}{t_0}, \\ + \quad & e^{st}\frac{U_p}{t_0}\frac{d}{ds}\left[\frac{(e^{b\sqrt{s}}+e^{-b\sqrt{s}})-(e^{a\sqrt{s}}+e^{-a\sqrt{s}})}{(e^{b\sqrt{s}}+e^{-b\sqrt{s}})-\frac{(e^{b\sqrt{s}}-e^{-b\sqrt{s}})}{b\sqrt{s}}}\right]. \end{aligned} \tag{A.13}$$

The equation A.13 is solved by splitting into two terms and the solution is given as:

$$\frac{3t}{2}[1-c^2]+\frac{h^2}{40\nu}[-5c^4-1+6c^2]. \tag{A.14}$$

Second pole given by $(e^{b\sqrt{s}}+e^{-b\sqrt{s}})-\frac{(e^{b\sqrt{s}}-e^{-b\sqrt{s}})}{b\sqrt{s}}=0$, by substituting $b\sqrt{s}=iv$ the term reduces into:

$$\begin{aligned} (e^{iv}+e^{-iv})-\frac{(e^{iv}-e^{-iv})}{iv} &= 0, \\ cos(v)-\frac{sin(v)}{v} &= 0, \\ tanv - v &= 0. \end{aligned}$$

Residues at $tanv-v=0$ are simple poles.

$$\sum_{s_n=1}^{\infty}\lim_{s\to s_n} e^{st}\frac{U_p}{t_0}\frac{\frac{1}{s}\left[(e^{b\sqrt{s}}+e^{-b\sqrt{s}})-(e^{a\sqrt{s}}+e^{-a\sqrt{s}})\right]}{\frac{d}{ds}\left[s\left[(e^{b\sqrt{s}}+e^{-b\sqrt{s}})-\frac{(e^{b\sqrt{s}}-e^{-b\sqrt{s}})}{b\sqrt{s}}\right]\right]}. \tag{A.15}$$

By substituting $b\sqrt{s}=iv_n$, $a\sqrt{s}=icv_n$ and simplifying the equation, the solution is obtained as:

$$\sum_{nh=1}^{\infty}\frac{2U_pb^2}{v_{nh}^2}\left[\frac{coscv_{nh}-cosv_{nh}}{v_{nh}sinv_{nh}}\right]e^{\frac{-v_nh^2t}{b^2}}. \tag{A.16}$$

The final solution, as in equation 2.8, is reached by summing all the residue terms.